Optical field sampling for imaging and optical testing

Gong, Hai

DOI
10.4233/uuid:33bdc816-d18f-4f33-89fe-a9cd462efd32

Publication date
2019

Document Version
Final published version

Citation (APA)
Gong, H. (2019). *Optical field sampling for imaging and optical testing*. [Dissertation (TU Delft), Delft University of Technology]. https://doi.org/10.4233/uuid:33bdc816-d18f-4f33-89fe-a9cd462efd32

Optical field sampling for imaging and optical testing

Optical field sampling for imaging and optical testing

Dissertation

for the purpose of obtaining the degree of doctor
at Delft University of Technology
by the authority of the Rector Magnificus Prof.dr.ir. T.H.J.J. van der Hagen,
chair of the Board for Doctorates,
to be defended publicly on
Monday 16 December 2019 at 12:30 o'clock

by

Hai GONG

Master of Engineering,
Xi'an Jiaotong University, Xi'an, China,
born in Hunan, China.

This dissertation has been approved by the promotors.

promotor: Prof. dr. G. Vdovin,
promotor: Prof. dr. ir. M. Verhaegen.

Composition of the doctoral committee:

Rector Magnificus,	chairperson
c Prof. dr. G. Vdovin,	Delft University of Technology, promotor
Prof. dr. M. Verhaegen,	Delft University of Technology, copromotor
Independent members:	
Prof. dr. P. Ubarch,	Delft University of Technology
Prof. dr. Z. Liu,	Xi'an Jiaotong University, China
Prof. dr. M. Neil,	Imperial College London, United Kingdom
Prof. dr. C. Keller,	Leiden University
Prof. dr. U. Wittrock,	Münster University of Applied Sciences, Germany
Prof. dr. P. French,	Delft University of Technology, reserved

Keywords: optical field, adaptive optics, imaging, optical testing, light sheet microscopy

Front & Back: Light · Shadow · Wave. A beautiful art illustration for this dissertation, designed by Miss Yachun Zhang.

ISBN 978-94-6366-237-6

学而不思则罔，
思而不学则殆。

孔子

Learning without thought is labor lost;
thought without learning is perilous.

Confucius

Contents

Acknowledgements

On my first CSI (Control for Scientific Instruments) meeting, I defined the PHD as the ’Perfect Holiday in Delft’. Finally, this holiday comes to an end. When I look back, this vacation consists of three parts to make it perfect: living in a scenic place, focusing on experiencing the joy of exploring technologies, being enlightened and supported by enthusiastic people. In particular, I owe thanks to the latter. Without them, this dissertation will not be completed and the life in Delft will not be that glorious.

First of all, I would like to thank my promoters: Prof. Gleb Vdovin and Prof. Michel Verhaegen, for allowing me to work in DCSC. They have given me significant guidance on research topics and a lot of freedom to investigate them. Gleb taught me like a master craftsman who will first give a hands on lesson for once and then let me work on the projects independently. Michel performs more as an architect who gives me the framework and then promotes the work with precise schedules. I will never forget his cheerful ’Excellent’ with a bit of Belgian accent after a long discussion.

Next, I would like to give thanks to my daily supervisor Dr Oleg Soloviev. He is a real chef of knowledge and an artist of presentation. It was always pleasant to have his coaching.

I am also grateful to my collaborators in DCSC for their generous support. Dr Paolo Pozzi is a genius at designing experiments. With his help, I can easily transfer my work from the office to the optics laboratory. Dr Dean Wilding was my office mate. He has always been the one I first ask help to. And he would patiently explain the principles to me on everything at his hand, such as a paper, a whiteboard, a computer and once even a beer mat, see Figure 1. Temitope Agbana has shown me how enthusiastic a man can be about research and serving people. We together won the Edmund Optics educational award in 2017.

Furthermore, I would like to thank the support team of DCSC and graduate school, Kitty, Erica, Kiran, Heleen, Marieke, Martha, Mascha, Will and Kees. With their kind supports, I had a very smooth from China to the Netherlands, a nice working space and responsive technical services.

I would give thanks to my DCSC colleagues, Huizhen, Chengpu, Raf, Sander, Carlas, Elisabeth, Hans, Laurens, Baptiste, Thao, Reinier, Shrinivas, Tijmen, Jelmer, Shuai, Maolong, Fan, Yiming, Jia, Anqi, Zhe, Pieter, Peter, Tian, Yichao, for making me feel home in the department.

Besides, I would like to thank all my friends and any person who helped me during this journey, which would be up to hundreds of people. I may not write down every name of them, but my gratitude to them would never be inferior.

Finally, I express my deepest gratitude to my parents, my step-mother, my sister and brother. My family give me firm support and love so that I can take adventures

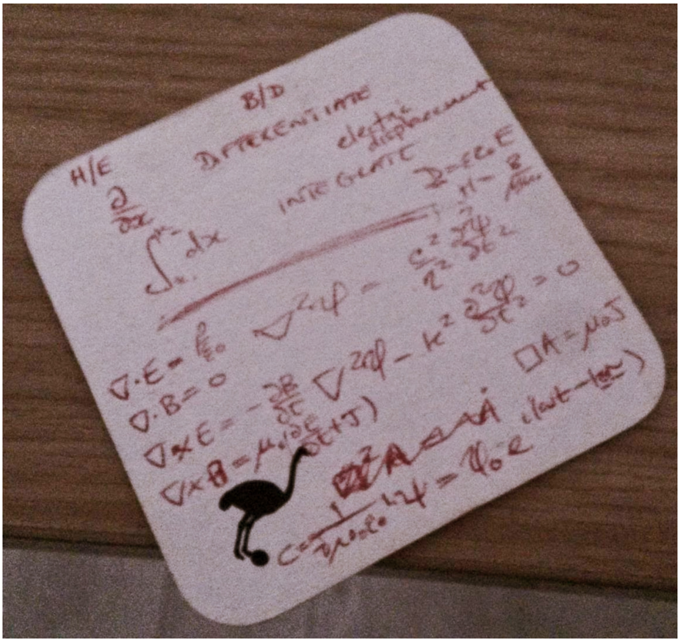

Figure 1: Maxwell's equations on a beer mat written by Dr Dean Wilding at a bar in Delft.

without hesitating. With a feeling of great sorrow, I can never share the joy with my grandmother and step-father anymore. May they hear my prayer in heaven.

Okay. It is time for another journey.

Hai Gong
Delft, September 2019

1

Introduction

1.1. Motivation

Light is a tool for human beings to explore the world. Though the space surrounds us is three-dimensional, mankind can only record the two-dimensional projection of this world for a long time, by either drawing pictures or taking photos. That is because the human eyes or cameras are merely able to sense the intensity of light radiation. To achieve a real three-dimensional imaging, the whole information of the light wave (*optical field*) including both the amplitude and the phase need to be registered. Thus, sensing the optical field is a very popular topic for scientific research along with a broad range of applications in engineering. For one example, in the content of diffraction theory [1], if the coherent optical field at one plane is recorded, the field at any other planes along the light path can be reconstructed by numerical propagation. Currently, there is no available physical sensor that can directly detect the phase due to the extremely high speed of light oscillation. Thus, we must retrieve it indirectly through specific optics and algorithms. The goal of this dissertation is to explore the techniques that allow us to capture the optical field and explore their implementations in imaging, optical testing and alignment etc. In the following chapter, there is a basic introduction of optical field, and a review of its state-of-the-art sensing techniques. Then, the chapter closes with a summary of the contributions and an outline of the dissertation.

Optical field

The wave behaviour of the light has been revealed for centuries. In 1678, the Dutch physicist Christiaan Huygens firstly proposed his wave theory of light in his work Treatise on Light [2]. It was not until 19th century, however, that people began to understand the physical nature of light, that it is an electromagnetic phenomenon. From then, the behaviour of light can be analysed in the context of electromagnetic theory based on the famous Maxwell's equations.

The optical field, referring to the electric field in optics, can be described by the solutions of Maxwell's equations, being modelled as a spatial-temporal complex field:

$$E(\mathbf{r}, t) = A(\mathbf{r}, t) \exp\left[i\left(-2\pi v t + \phi(\mathbf{r})\right)\right], \tag{1.1}$$

where E is the electrical field vector at the position $\mathbf{r} = (x, y, z)$ in space at a time t. A is the amplitude. $v = c/\lambda$ is the temporal frequency of light which is defined by the light speed c divided by the wavelength λ. The spatially relevant phase term $\phi(\mathbf{r})$ contains two parts: spatially varying phase $\mathbf{kr}$ and a constant phase ϕ_0,

$$\phi(\mathbf{r}) = -\mathbf{kr} - \phi_0, \tag{1.2}$$

where $\mathbf{k}$ is the wave vector that describes the propagation direction of the wave. The modulus of $\mathbf{k}$ is the wave number $k = 2\pi/\lambda$. Some of the most important properties of light are included in this model, such as amplitude, phase and wavelength. Basically, these are the key parameters to understand light.

For most wavelengths in the light spectrum, the temporal frequencies v have an order of 10^{14} Hz which is too high for current light sensors to detect. In many cases, only the spatial distribution of the wave is interesting for the optical calculations, such as holography. Therefore, the time component t is ignored. And the optical field can be simplified as a complex amplitude function:

$$U(\mathbf{r}) = A \exp\left[i\phi(\mathbf{r})\right]. \tag{1.3}$$

In this dissertation, the optical field we are going to investigate is modelled by 1.3. By far, the only directly measurable quantity of the light is time averaged intensity, which is generally calculated by taking the square of the modulus of the optical field:

$$I = |U(\mathbf{r})|^2 = U(\mathbf{r})\, U^*(\mathbf{r}), \tag{1.4}$$

where $\{\cdot\}^*$ denotes complex conjugation. Basically, all the methods that recover the optical field has to start from intensity measurements.

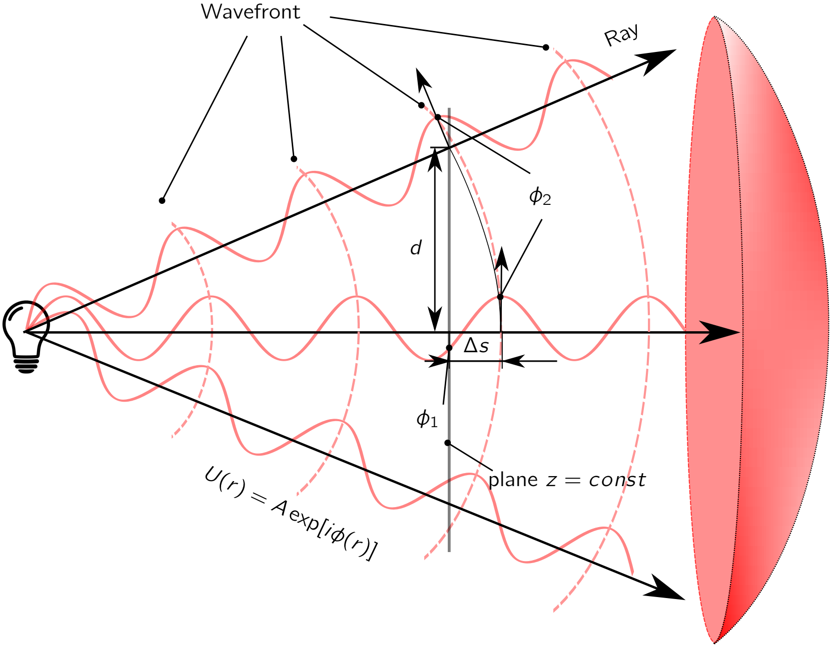

Figure 1.1: Geometrical illustration of optical wave, wavefront and ray direction.

Here we describe the wave propagation in geometry. Assuming a point source emits light rays in a homogeneous medium with a refractive index of n in Figure 1.1, the light waves propagate with the same initial phase. The surface of equal phase in the space is named *wavefront* [3]. The normal vector of wavefront represents the moving direction of rays which can be used to reconstruct the wavefront surface geometrically. The distribution of the phase in a plane $\phi(x, y)$ is linked to the wavefront function $W(x, y)$ facing to the plane. In this particular case, the wavefront is a spherical surface. Considering the marginal wave and chief wave that arrive the plane $z = const$, there is a phase difference between them: $\Delta\phi = \phi_2 - \phi_1$. This phase difference $\Delta\phi$ is given by the distance Δs between the wavefront surface and the plane z:

$$\Delta\phi = \frac{2\pi}{\lambda}\Delta s. \tag{1.5}$$

Thus, with the shape of the wavefront being obtained geometrically, we are able to convert it to the phase of the optical field. If we approximate the local wavefront between them with a planar surface, then the tilt angle of it can be determined by $\alpha = \arctan(\Delta s/d)$, where d is the distance between these two waves on the plane. With surface reconstruction algorithms, the global wavefront can be obtained from all the wavefront tiles. The distance Δs is caused by different optical paths and varied refractive indexes on the path. It carries an abundance of information, such as the geometric feature of an object, the aberrations of the optics and even the changes of pressure, temperature and humidity on the light path, which makes it appealing for researchers.

Another important property between light waves is coherence. It basically describes how well two waves are correlated with each other which is implied in the phase term of the complex amplitude. Coherent light waves can interfere with each other when they are superposed. The phase difference between them will lead to the wave being strengthened or weaken. This phenomenon is described in the Section 1.2 in detail, and it is an important principle to reveal the optical field. The coherence of a light is usually discussed in aspects of temporal coherence and spatial coherence. Temporal coherence describes how well the frequency synchronization is between the waves emitted from the same source. It is usually determined by the finite spectral width of the source. Light with a longer coherence length corresponds to a narrower linewidth. Spatial coherence is the cross correlation of two separated points of the same wave field. It describes whether the wave has a fixed and well-defined relative phase or wavefront in the space. The spatial coherence length is usually related to the size of the extended light source and the propagation distance. Since most of the experiments are done with monochromatic sources, temporal coherence properties have minor effect, we mainly consider the spatial coherence properties in the scope of this dissertation.

1.2. State-of-the-art

There are a great number of techniques that have emerged to challenge the problem of recovering the complex optical field. Every method tends to have its own specific optical apparatus, electronics, data sets and software. Technically, they are distinct to each other. In principle, some of them share the same root. Here we categorize them into three main groups: interferometric methods, wavefront sampling methods and computational methods.

Interferometric methods

Interferometric methods utilize the interference phenomenon of two superposed coherent waves to decode the optical field as mentioned previously. Given two monochromatic waves $U_1 = A_1 \exp(i\phi_1)$ and $U_2 = A_2 \exp(i\phi_2)$, the intensity of their superposition can be written as:

$$\begin{aligned} I &= (U_1 + U_2)(U_1 + U_2)^* \\ &= A_1^2 + A_2^2 + A_1 A_2 \left[\exp(i\phi_1 - i\phi_2) + \exp(i\phi_2 - i\phi_1)\right] \\ &= I_1 + I_2 + 2\sqrt{I_1 I_2}\cos(\phi_1 - \phi_2), \end{aligned} \tag{1.6}$$

where I_1 and I_2 are the intensity of these two waves respectively.

The phase difference $\Delta\phi = \phi_1 - \phi_2$ is encoded in the intensity variation. Considering one planar wave is the reference, the other wave is from the object, the interference is performed over a number of points on a recording film, then the object field can be reconstructed in the space by illuminating the interferogram (also called hologram) with a beam identical to the reference. This technique named "holography" is firstly invented by Denis Gabor in 1948 [4]. Later, with the help of computer and digital recording devices, the complex optical field can be quantitatively measured and numerically reconstructed [5].

According to the arrangement of the angle between the reference beam and sample beam, the holography methods can be sorted into on-axis (in-line) configuration and off-axis configuration. In on-axis holography, the optical axis of a reference beam is identical to the sample beam which can simplify the optical instrumentation. However, the optical field information is spatially overlapped with unwanted phase conjugated information, it usually requires iterative algorithms to remove the disturbing zero-order and twin-image. Off-axis holography employs a tilted reference beam to interfere with the object beam, which gives a well-defined carrier spatial frequency to separate the desired image term from the zero-order and twin-image. The disadvantage is it can not make full use of the bandwidth of the camera, thus captures less fine spatial details of the sample compared with the on-axis configuration [6–8]. There is another group of interferometric methods called shearing interferometry that uses a shifted copy of the object wave as the reference wave. Thus, it usually decodes the gradients of the phase instead of the phase directly [9, 10].

These interferometric methods are able to measure the phase in an extremely high precision and resolution. Correspondingly, they demand a high temporal and spatial coherence of the light and are very sensitive to the perturbations from the environment such as mechanical vibrations and thermal changes. Also, the need of a reference increases the complexity of an interferometric system which obstacle the applications in many portable and space limited situations.

Wavefront sampling methods

There are a number of sensors have been developed to reconstruct the wavefront of a beam. These wavefront sensors (WFS) usually first measure the feature of the wavefront (e.g. gradients, curvatures) regionally or globally with specified sampling elements, and then reconstruct the complete wavefront [11].

One of the most popular wavefront is Hartmann/Shack-Hartmann wavefront sensor. The Hartmann wavefront sensor (HWFS) is consisted of an array of apertures mounted a distance from a pixelated sensor. The incident light propagates to the sensor and forms spots like pattern on it. The displacement of each diffracted spot is proportional to the average wavefront tilt over the local aperture. Thus, it can measure the relative gradient change of a wavefront compared to a reference. Then the gradients are numerically integrated to reconstruct the incident wavefront. That is to say, each aperture samples the phase information of an optical field in a discrete manner. The Shack-Hartmann wavefront sensor (SHWFS) is a variation of HWFS, which is specifically described later in Section 2.3. The aperture array is replaced by a lenslet array which much increases the photon efficiency [12].

Another variant of HWFS is the multiple-wave lateral shearing interferometry, which combines the interferometry and the discretizing idea of a wavefront sensor [10]. The conventional shearing interferometry can only measure the phase gradients in one direction. The multiple-wave interferometry extends the measurability to more than one gradient direction by making use of a modified Hartmann mask. In the case of quadri-wave lateral shearing interferometry [13], the mask is made by a superposition of a binary amplitude grating (period p) and a π shift phase grating (period $2p$). Four tilted replicas of the local wavefront are created to interfere with each other. The two-dimensional wavefront gradient can be extracted from the interferogram with a Fourier deconvolution algorithm, which is similar to the one in Section 2.4.2 of Chapter 2 [14]. This method technically can achieve higher spatial resolution and dynamic range than SHWFS. However, the requirement for the light coherence is higher due to its interferometric nature.

In the previous methods, the wavefront is segmented on its surface. However, there is a group of sensors that their sampling subdivision operation is performed at the focal plane (Fourier plane). A typical one is pyramid wavefront sensor [15]. It utilizes a pyramidal-shape prism to split the light on the focal plane, and generate four sub-images with a relay lens. By processing this four images, it can achieve a performance the same as a SHWFS with a four pixels per spot centroiding mode. In other variants, a quatrefoil lens [16] and a liquid crystal display [17] are used as the Fourier plane splitter. They usually do not need expensive components and can achieve high spatial resolution. However, the dynamic range of the wavefront slope detection is limited. Special techniques such as oscillating the pyramid and the input field are proposed to conquer the problem [15, 18, 19].

Compared to the interferometric methods, wavefront sensors generally do not require strict coherence of the light and an extra reference beam. Thus, the system can be very compact and easy to align. Conventionally, the number and diameter of the aperture/ lenslets, along with the focal length, limit the performance of wavefront sensor in terms of spatial resolution, dynamic range and the sensitivity [20]. Though they have gained a great popularity in the applications of optics testing, laser beam characterization and adaptive optics, not many people consider it as a holographic imaging device yet. However, with the developing of the manufacturing technology, there are higher spatial resolution wavefront sensors available. Thus, in this dissertation, we investigate the principle and requirement of such wavefront sensors for the imaging and optical testing applications.

Computational methods

A group of methods that relies heavily upon mathematical algorithms to recover the optical field has arisen. Accordingly, they are with minimum optics involved. In the system theory, a general imaging system can be mathematically simplified as a linear space-invariant system [1]:

$$\mathbf{y} = \mathbf{h} * \mathbf{x}. \tag{1.7}$$

Here **y** is the output. It is the convolution '*' of an input **x** with the transfer function **h** of the optical system.

The input and output can be real-valued functions (intensity) or complex-valued functions (optical field). In general, if the illumination of an optical system is spatial coherent, the light can be described as a spatial distribution of complex-valued field amplitude. If the illumination is spatial incoherent, then the light can be described as a spatial distribution of real-valued intensity.

Many optical process such as free-space propagation, lens transform, pupil filtering, and spatial light modulation can be precisely modelled in transfer functions. We can slightly change parameters in the optical setup, such as propagation distance, aberration and aperture shape, to form a series of transfer functions. With the corresponding multiple outputs being measured, it is possible to compose linear equations to solve the input field. Or, on the contrary, we can change the parameters of the input field, such as illumination angle, optical phase, intensity distribution, to identify the optical systems. Therefore, many computational techniques have been developed to recover the optical field from this point of view.

Phase retrieval is a class of such techniques that derives from many practical fields such as astronomical imaging, X-ray crystallography, electron microscopy and radar. It usually recovers the phase information from the intensity measurements with some prior information given by assumptions about the object beam and special constraints. For an instance of these assumptions, the sampled object is often considered to be finite, of positive intensity and the background is empty in literature [21–24]. There is a more detailed review of its algorithms in the Section 2.6. Here we take a glimpse of this approach.

A general scheme of the majority phase retrieval methods is as follows: first applying an initial guess of the phase function, with the system transfer function being modelled, then an estimated intensity distribution being produced, and comparing it to the measured data. The initial guess is adjusted iteratively or with other optimization algorithms to minimize the error between the estimation and measurement.

One popular iterative phase updating scheme is the Gerchberg-Saxton algorithm, in which the estimation of the optical field is transformed back and forth between the object plane and Fourier plane. At each plane, a projecting operation based on the intensity constraint is performed. The detailed algorithm is described in the Section 2.6.3. Non-iterative scheme has also been developed. A well-received one is based on the transport-of-intensity equation which is shown in the Section 2.6.1.

However, there are some problematic issues that provide an obstacle to the success of phase retrieval. Besides the problem of finding a local minimum that lies in most optimization schemes, the phase retrieval problem is also an ill-posed inverse problem due to the fact that different phase solutions may lead to the same output image. The ambiguities of a phase estimation $\hat{\phi}(x,y)$ come from three sources: the background constant phase $\hat{\phi}(x,y)+c$, the wrapped phase $\hat{\phi}(x,y)+2\pi N(x,y)$, and the symmetric term $\hat{\phi}(-x,-y)$. To resolve the ambiguity problem in phase retrieval, additional information is usually required [25]. This extra information is usually measured with slightly applying some diversities to the system, such as modulating an optical element and the illumination source [26].

Phase diversity is a popular implementation of this phase retrieval technique, in which known phase aberrations are added to the light path for extra measurements [27]. These phase aberrations can be introduced by utilizing phase mask, spatial light modulator or simply measuring at different planes with a defocus aberration [28]. Techniques that utilizes amplitude diversity has also been developed. For example, the structured illumination has been used to enhance the resolution of complex field imaging [29]. In the work of Ref [30], combining a random amplitude mask with a phase diversity scheme leads to a unique, accurate and fast-convergent reconstruction.

A technique known as pytchography is also considered as an amplitude diversity approach which is firstly devised in the field of electronic imaging [31]. A spatial constraint is applied to the illumination so that the sample is scanned with some overlap area in each step and multiple diffraction patterns are obtained for phase retrieval. The result from each pattern is fed to the reconstruction of adjacent areas as a better initial guess. Thus, instead of the point like object, the full-field of an extended object can be imaged by scanning through the whole sample. The overlapping procedure can also be done in the Fourier domain which is named Fourier pytchography [32]. This technique enables the microscope to image beyond the cut-off frequency of the employed objective lens.

Compared to holographic methods and wavefront sensors, computational methods need no reference beam and tailored optical components. They are able to extend the capability of imaging systems with robust and relatively inexpensive apparatus. However, the necessary pre-processing and calibration of the setup are usually very crucial for the accurate and reliable reconstruction. Furthermore, the post-processing algorithms for the optical field restoration are computationally intensive in general. To eliminate the ambiguities, multiple acquisitions are preferred to restore one image. These time-consuming processes hinder the real-time application of this group of methods.

1.3. The scope and outline of the dissertation

The scope of this dissertation mainly covers the following research contents: (1) exploring new optical field sensing techniques with the help of newly emerging optical components; (2) defining the conditions for holographic imaging with conventional wavefront sensors; (3) extending the imaging and optical testing applications of optical field sensing in practical scenarios. Following the same order used to introduce these works, the dissertation has been structured as follows.

Chapter 1
In this chapter, we introduce the motivation and scope for optical field sensing and have a brief review of the existing techniques. An outline of the work is included.

Chapter 2
This chapter provides the fundamental theories and frequently referred tools throughout the dissertation. The sampling criteria for optical field sensing, physical phenomenon of interferometry, and the mathematical modeling of optical elements are explained in the framework of Fourier optics. The algorithmic techniques for correctly converting the intensity recordings to optical field measurements, which includes wavefront gradient extraction, wavefront reconstruction, phase retrieval and phase unwrapping algorithms, are reviewed in details.

Chapter 3
This chapter explores a novel approach to register the complex optical field with a programmable spatial amplitude modulator. This multiplex based approach contains two schemes: (1) demodulating the phases from multiple interferograms generated by sequentially scanning of two-points interferometers, (2) phase retrieval from multiple speckle patterns generated by binary masks. No external reference beam is required for this approach. The experimental validation for coherent lensless imaging is carried out by utilizing a digital micromirror device as the essential amplitude modulator.

This chapter is based on the work in the following publications:
G. Vdovin, *H. Gong*, O. Soloviev, P. Pozzi, and M. Verhaegen. Lensless coherent imaging by sampling of the optical field with digital micromirror device. Journal of Optics, 17(12), 122001 (2015).
H. Gong, P. Pozzi, O. Soloviev, M. Verhaegen, and G. Vdovin. Phase retrieval from multiple binary masks generated speckle patterns. Proc. SPIE Optical Sensing and Detection IV (9899), 98992N (2016).

Chapter 4
This chapter investigates the feasibility of a conventional wavefront sensor, specifically the Shack-Hartman wavefront sensor, for holographic coherent imaging. We clarified the relationships in respect to the imaging resolution and wavefront detection resolution in the coherent lensless imaging setting. This concept is experimentally examined by combining the numerical propagation with the complex amplitude in the far field directly registered by a high density Shack-Hartmann wavefront sensor.

This chapter is based on the work in the following publications:
H. Gong, O. Soloviev, D. Wilding, P. Pozzi, M. Verhaegen, and G. Vdovin. Holographic imaging with a Shack-Hartmann wavefront sensor. Optics Express, 24(13), 13729 (2016).
T. E. Agbana, *H. Gong*, A. S. Amoah, V. Bezzubik, M. Verhaegen, and G. Vdovin.

Aliasing, coherence, and resolution in a lensless holographic microscope. Optics Letters, 42(12), 2271 (2017).

Chapter 5
In this chapter, we present a quantitative phase imaging technique by measuring the optical path difference with a Shack-Hartmann wavefront sensor at the image plane. The illumination condition for the correct quantitative phase imaging is defined for the microscopic case. Both the transmissive and reflective configurations have been implemented to validate the predicted performance for optical testing and biological sample observation.

This chapter is based on the work in the following publications:
H. Gong, T. E. Agbana, P. Pozzi, O. Soloviev, M. Verhaegen, and G. Vdovin. Optical path difference microscopy with a Shack–Hartmann wavefront sensor. Optics Letters., 42(11), 2122, (2017).
H. Gong, O. Soloviev, G. Vdovin, and M. Verhaegen. Shack-Hartmann reflective micro profilometer. 2017 International Conference on Optical Instruments and Technology: Optical Systems and Modern Optoelectronic Instruments, 68 (2018).

Chapter 6
In this chapter, we develop approaches to miniaturize the illumination path of a light sheet microscope which allows adaptive control. Two approaches based on slab and GRIN lens waveguides have been designed and demonstrated respectively. These two configuration allows the transmission of multiple modes which enable the wavefront engineering after the waveguides.

This chapter is based on:
The report of the project "Adaptive Imaging Microscopy (AIM)" to Horizon 2020, ERC-PoC-2016, 737564, (2018).
Patent application: *H. Gong*, M. Verhaegen, G. Vdovin, P. Pozzi, O. Soloviev, D. Wilding, Light sheet microscopy with a waveguide (voorlopig aanvraagnummer: N2021567).

Chapter 7
This chapter summarizes the results of the dissertation and makes suggestion for the future research.

References

[1] J. W. Goodman, *Introduction to Fourier Optics*, 2nd ed. (Roberts and Company Publishers, 2005) p. 491.

[2] C. Huygens, *Treatise on light* (tredition, 2012).

[3] M. Bass, C. DeCusatis, J. Enoch, V. Lakshminarayanan, G. Li, C. Macdonald, V. Mahajan, and E. Van Stryland, *Handbook of Optics, Third Edition Volume I: Geometrical and Physical Optics, Polarized Light, Components and Instruments(Set)*, 3rd ed. (McGraw-Hill, Inc., New York, NY, USA, 2010).

[4] D. Gabor, *A New Microscopic Principle,* Nature **161**, 777 (1948).

[5] U. Schnars, C. Falldorf, J. Watson, and W. Jüptner, *Digital Holography and Wavefront Sensing: Principles, Techniques and Applications* (Springer, 2015) pp. 1–226.

[6] K. Lee, K. Kim, J. Jung, J. Heo, S. Cho, S. Lee, G. Chang, Y. Jo, H. Park, and Y. Park, *Quantitative Phase Imaging Techniques for the Study of Cell Pathophysiology: From Principles to Applications,* Sensors **13**, 4170 (2013).

[7] L. Xu, X. Peng, J. Miao, and a. K. Asundi, *Studies of digital microscopic holography with applications to microstructure testing.* Applied optics **40**, 5046 (2001).

[8] M. Mir, B. Bhaduri, R. Wang, R. Zhu, and G. Popescu, *Progress in Optics*, Vol. 57 (Elsevier Inc., 2012) pp. 133–217.

[9] D. Malacara, M. Servín, and Z. Malacara, *Interferogram Analysis For Optical Testing, Second Edition* (2005) p. 440.

[10] J.-C. Chanteloup, *Multiple-wave lateral shearing interferometry for wave-front sensing.* Applied optics **44**, 1559 (2005).

[11] J. M.Geary, *Introduction to Wavefront Sensors* (SPIE Optical Engineering Press, 1995).

[12] B. C. Platt and R. Shack, *History and Principles of Shack-Hartmann Wavefront Sensing,* Journal of Refractive Surgery **17**, 573 (2001).

[13] P. Bon, G. Maucort, B. Wattellier, and S. Monneret, *Quadriwave lateral shearing interferometry for quantitative phase microscopy of living cells.* Optics express **17**, 13080 (2009).

[14] S. Velghe, J. Primot, N. Guérineau, R. Haïdar, S. Demoustier, M. Cohen, and B. Wattellier, *Advanced wave-front sensing by quadri-wave lateral shearing interferometry,* , 62920E (2006).

[15] R. Ragazzoni, *Pupil plane wavefront sensing with an oscillating prism,* Journal of Modern Optics **43**, 289 (1996).

[16] A. B. Parthasarathy, K. K. Chu, T. N. Ford, and J. Mertz, *Quantitative phase imaging using a partitioned detection aperture,* Optics Letters **37**, 4062 (2012).

[17] I. Iglesias and F. Vargas-Martin, *Quantitative phase microscopy of transparent samples using a liquid crystal display,* Journal of Biomedical Optics **18**, 026015 (2013).

[18] I. Iglesias, R. Ragazzoni, Y. Julien, and P. Artal, *Extended source pyramid wavefront sensor for the human eye,* Optics Express **10**, 419 (2002).

[19] T. Y. Chew, R. M. Clare, and R. G. Lane, *A comparison of the Shack-Hartmann and pyramid wavefront sensors,* Optics Communications **267**, 189 (2006).

[20] D. R. Neal, J. Copland, and D. A. Neal, *Shack-Hartmann wavefront sensor precision and accuracy,* Advanced Characterization Techniques for Optical, Semiconductor, and Data Storage Components **4779**, 148 (2002).

[21] J. R. Fienup, *Reconstruction of an object from the modulus of its Fourier transform,* Optics Letters **3**, 27 (1978), arXiv:78 [0146-9592] .

[22] J. R. Fienup, *Phase retrieval algorithms: a comparison,* Applied Optics **21**, 2758 (1982).

[23] R. P. Millane, *Phase retrieval in crystallography and optics,* Journal of the Optical Society of America A **7**, 394 (1990).

[24] B. Guo, F. Gao, H. Zhao, L. Zhang, J. Li, and Z. Zhou, *Phase retrieval for non-ideal in-line phase contrast x-ray imaging,* **10074**, 1 (2017).

[25] T. Bendory, R. Beinert, and Y. C. Eldar, *Fourier phase retrieval: Uniqueness and algorithms,* in *Compressed Sensing and its Applications* (Springer, 2017) pp. 55–91.

[26] A. Fannjiang and W. Liao, *Phase retrieval with random phase illumination,* Journal of the Optical Society of America A **29**, 1847 (2012), arXiv:1206.1001 .

[27] R. A. Gonsalves, *Phase retrieval and diversity in adaptive optics,* Optical Engineering **21**, 829 (1982).

[28] G. Pedrini, A. Faridian, P. Gao, D. Naik, A. Singh, W. Osten, and M. Takeda, *Phase retrieval methods for optical imaging and metrology,* in *2014 13th Workshop on Information Optics (WIO)* (IEEE, 2014) pp. 1–3.

[29] S. Chowdhury and J. Izatt, *Structured illumination quantitative phase microscopy for enhanced resolution amplitude and phase imaging,* Biomedical Optics Express **4**, 1795 (2013).

[30] A. Anand, G. Pedrini, W. Osten, and P. Almoro, *Wavefront sensing with random amplitude mask and phase retrieval.* Optics letters **32**, 1584 (2007).

[31] W. Hoppe, *Trace structure analysis, ptychography, phase tomography,* Ultramicroscopy **10**, 187 (1982).

[32] G. Zheng, *Fourier ptychographic imaging: a MATLAB tutorial* (Morgan & Claypool Publishers, 2016).

2

Fundamentals of optical field sensing

In this chapter, we introduce the fundamental principles and algorithms that form the basis of this dissertation. The sampling theorem of the optical field, the theory of interferometry and the detail principle of a Shack-Hartmann wavefront sensor are described. We also reviewed the algorithms for gradient demodulation, wavefront reconstruction, phase retrieval and phase unwrapping which are frequently referred to in the following chapters.

The techniques of sensing the optical field are complex combinations of optics and algorithms. To have a good understanding of the existing and proposed approaches, the readers not only need to know how optics work so that we can model the optics system and obtain the raw measurements correctly, but also to master the numerical techniques such as wave propagation, signal processing, optimization etc. for retrieving the useful information. In the following chapters, our proposed methods are built on the interferometric principle, phase retrieval (Chapter 3), and the Shack-Hartmann wavefront sensor (Chapter 4, 5 and 6). Therefore, we have a preliminary introduction of all the fundamentals in this chapter.

2.1. Sampling of the coherent optical field

Basically, most of the signals in the real world , also named analogue signals, are continuous. When they are processed by any digital sensors, they will be discretely recorded. This process, no matter in space, time or any other dimension, is called sampling. A proper sampling process should allow the analogue signal be reconstructed exactly without any key information being lost. Thus, the digitization usually follows some sampling criteria in practice.

In the digital signal processing applications, the most well-known sampling theorem is the Shannon-Whittaker sampling theorem. It states that a band limited signal with a maximum spectral component f_{max} can be reconstructed without aliasing by a sampling rate $f_s \geqslant 2f_{max}$. This condition is also called Nyquist sampling criterion.

However, for many optical systems, such as holography applications, the information need to be measured are usually not at the plane that being detected. Thus, the Nyquist sampling criterion can not directly apply to these situations as shown by many researchers [1, 2]. Here some generalized principles for optical field sampling is introduced to guide the system implementation.

Figure 2.1 illustrates the general scheme of the sampling and reconstruction in an optical system. Given an initial optical field $U_0(x, y)$, it will be transformed by the optical system composed of various optics. The optical operations of the field, such as propagation, diffraction and filtering can be summarized by a transfer function $h(x, y)$, giving the field after the optical system $U_z(x, y) = U_0(x, y) * h(x, y)$.

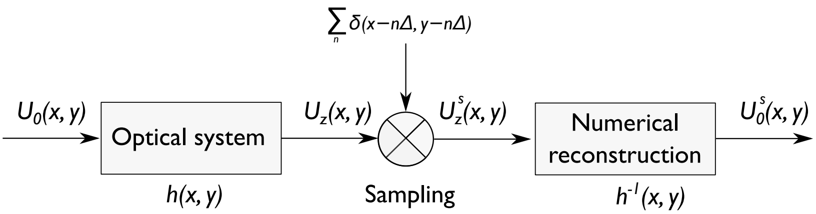

Figure 2.1: A general scheme of the sampling and reconstruction in an optical system.

Generally, we can only detect the intensity instead of the complex amplitude of the optical field due to the temporal resolution limitation of the opto-electronic sensors.

However, the complex information can be encoded in the intensity pattern through many methods, such as holography and various wavefront sensors. Here we assume the complex amplitude has been decoded and sampled in a discrete form $U_z^s(x,y)$. Then the original optical field can be reconstructed numerically by inverse transforming the sampled field: $U_0^s(x,y) = U_z^s(x,y) * h^{-1}(x,y)$. In the following, we analysis the problem in one-dimensional for the simplicity of notation. The conclusion for the two-dimensional situation is straightforward.

Considering a coherent case the in free space, the original optical field $U(x,0)$ (the second argument denotes the distance to the original point, here is $z=0$) propagates to a distance z. The final optical field can be approximated by the Fresnel diffraction according to the scalar wave diffraction theory: $U(x,z) = U(x,0) * h(x,z)$. Here $h(x,z)$ is the convolution kernel of the Fresnel diffraction: $e^{i\frac{k}{2z}x^2}$.

Thus, we have the optical field at the sensor plane:

$$U(x,z) = \frac{\exp(ikz)}{i\lambda z} \int_{-\infty}^{\infty} U(f_x,0) \exp\left[\frac{ik}{2z}(x-f_x)^2\right] df_x. \tag{2.1}$$

Assuming the optical field is recorded by a sensor with a pixel size of Δ, the sampled version of the diffraction filed can be expressed as:

$$U^s(x,z) = U(x,z) \sum_{n=-\infty}^{\infty} \delta\left(x - n\Delta\right). \tag{2.2}$$

Reconstructing the original field can be done by numerically convolving the diffraction field with an inverse Fresnel kernel $h^{-1}(x,z)$, which is equivalent to reversing the propagation direction by using $h(x,-z)$. Back propagating the sampled diffraction field in the Fourier domain, we have:

$$\begin{aligned}
\tilde{U}^s\left(f_x,0\right) &= \mathcal{F}\{U^s(x,z)\}\tilde{h}\left(f_x,-z\right) \\
&= \mathcal{F}\left\{U(x,z)\sum_n \delta(x-n\Delta)\right\}\tilde{h}\left(f_x,-z\right) \\
&= \mathcal{F}\left\{\mathcal{F}^{-1}\left\{\mathcal{F}\{U(x,0)\}\tilde{h}\left(f_x,z\right)\right\}\sum_n \delta(x-n\Delta)\right\}\tilde{h}\left(f_x,-z\right) \\
&= \mathcal{F}\left\{U(x,0) * h(x,z)\sum_n \delta(x-n\Delta)\right\}\tilde{h}\left(f_x,-z\right) \\
&= \sum_m \tilde{U}(f_x - \frac{m}{\Delta},0)\tilde{h}\left(f_x - \frac{m}{\Delta},z\right)\tilde{h}\left(f_x,-z\right).
\end{aligned} \tag{2.3}$$

A tilde sign '˜' is used to notate the Fourier transform of a function in here. The Fourier transform of the transfer function $h(x,z)$ is:

$$\tilde{h}\left(f_x,z\right) = \exp(ikz)\exp\left(-i\pi\lambda z {f_x}^2\right). \tag{2.4}$$

Thus, the multiplication of the two transfer functions in equation 2.3 can be expressed as:

$$\begin{aligned}\tilde{h}\left(f_x-\frac{m}{\Delta},z\right)\tilde{h}\left(f_x,-z\right)&=\exp(ikz)\exp\left[-i\pi\lambda z\left(f_x-\frac{m}{\Delta}\right)^2\right]\exp(-ikz)\exp\left(i\pi\lambda z{f_x}^2\right)\\&=\exp\left[i\pi\lambda z\left(2\frac{m}{\Delta}f_x-\frac{m^2}{\Delta^2}\right)\right]\\&=\exp\left(-i\pi\lambda z\frac{m^2}{\Delta^2}\right)\exp\left(i2\pi\lambda z\frac{m}{\Delta}f_x\right).\end{aligned} \tag{2.5}$$

The sampled original optical field is reconstructed by substituting equation 2.5 into equation 2.3 and then taking an inverse Fourier transform:

$$\begin{aligned}U^s(x,0)&=\mathcal{F}^{-1}\left\{\sum_m\tilde{U}\left(f_x-\frac{m}{\Delta},0\right)\tilde{h}\left(f_x-\frac{m}{\Delta},z\right)\tilde{h}\left(f_x,-z\right)\right\}\\&=\mathcal{F}^{-1}\left\{\sum_m\tilde{U}\left(f_x-\frac{m}{\Delta},0\right)\exp\left(-i\pi\lambda z\frac{m^2}{\Delta^2}\right)\exp\left(i2\pi\lambda z\frac{m}{\Delta}f_x\right)\right\}\\&=\exp\left(-i\pi\lambda z\frac{m^2}{\Delta^2}\right)\mathcal{F}^{-1}\left\{\sum_m\tilde{U}\left(f_x-\frac{m}{\Delta},0\right)\exp\left(i2\pi\lambda z\frac{m}{\Delta}f_x\right)\right\}.\end{aligned} \tag{2.6}$$

Here we refer to the shift property of the Fourier transform:

$$\mathcal{F}\{u(x)\exp(i2\pi ax)\}=\tilde{u}(f_x-a). \tag{2.7}$$

We finally have the back propagation result:

$$U^s(x,0)=\exp\left(-i\pi\lambda z\frac{m^2}{\Delta^2}\right)\sum_m U\left(x-m\frac{\lambda z}{\Delta},0\right)\exp\left(i2\pi\frac{m}{\Delta}x\right). \tag{2.8}$$

In the result above, the constant phase term $\exp\left(i2\pi\frac{m}{\Delta}x\right)$ indicates the signal is sampled at a rate $f_s=1/\Delta$. It means, in the Fourier domain, the spectrum is a sequence of the replica of the signal Fourier transform with a period of f_s. In accordance with the Shannon sampling theorem, the adjacent replica should not overlap to avoid aliasing. However, the difference is that the numerical reconstruction also leads to an infinite replica of $U(x,0)$ in the space domain. The replica is separated by an interval of $\lambda z/\Delta$. Thus, we need to avoid the overlap in the space domain as well.

To recover the original field $U(x,0)$ from its diffraction field samples without loss and aliasing, we need to consider the cases in both the Fourier domain and space domain.

2.1.1. Band limited case

If the original field $U_0(x)$ has a limited bandwidth B, which means

$$\tilde{U}(f_x, 0) = 0, \quad \text{if} \quad f_x \notin B. \tag{2.9}$$

The maximum frequency of the signal is $f_m = B/2$.

Since the Fresnel transfer function is not band limited, the diffraction field shares the same Fourier spectrum bandwidth with the original field. Similar to the Shannon sampling theorem, the field can be fully recovered if the sampling frequency is higher than twice the signal maximum frequency: $f_s > 2f_m$.

The reconstruction can be carried out by applying a low-pass filter $\tilde{g}(f_x)$ with a cut-off frequency $f_c : f_m < f_c < f_s - f_m$ to filter out the replica in the Fourier spectrum of sampled back propagation:

$$U^s(x, 0) = \mathcal{F}^{-1}\left\{\mathcal{F}\{U^s(x, z)\}\tilde{g}(f_x)\tilde{h}(f_x, -z)\right\}, \tag{2.10}$$

where

$$\tilde{g}(f_x) = \begin{cases} 1 & \text{if } |f_x| \leqslant f_c, \\ 0 & \text{else.} \end{cases} \tag{2.11}$$

Here we shall explain it with a simulated example as follows. Giving a band limited signal $U(x, 0) = \sin(2\pi f_a x - \pi/2) + 1$, where the $f_a = 1000\ m^{-1}$, which is shown in Figure 2.2 (a). $U(x, 0)$ is propagated in free space to a distance $z = 8\ m$ by the Fresnel approximation in equation 2.1. The diffraction field is presented in Figure 2.2 (b). The red circles indicate the sampling point of the signal. The space is defined by an array of $N = 2048$, each pixel has a size of $\delta x = 20\ \mu m$. Thus, the size of the area is $A = N\delta x$, and $x \in [-A/2, A/2]$. The wavelength is $500\ nm$.

The following figures show the reconstructions from the discrete diffraction field with different sampling rates. Figure 2.2 (c) is sampled by a frequency $f_s = 1.5 f_a$, which does not meet the Nyquist criterion. Aliasing appears from the reconstruction. The signal is fully recovered by using a sampling rate $f_s = 2.5 f_a$ in Figure 2.2 (d).

2.1.2. Space limited case

If $U_0(x)$ is space limited, which is expressed as

$$U(x, 0) = 0 \quad \text{if} \quad f_x \notin R. \tag{2.12}$$

From equation 2.8 we know if the size of original field satisfy $L \leq \lambda z/\Delta$, then the original field can be reconstructed without overlap. We just have to filter the result of the back propagation with the bound of space to get the original field. Thus, the reconstruction procedure can be carried out by applying a filter $G(x)$ in the space domain:

$$U^s(x, 0) = G(x) \exp\left(-i\pi\lambda z \frac{m^2}{\Delta^2}\right) \sum_m U\left(x - m\frac{\Delta}{\lambda z}, 0\right) \exp\left(i2\pi \frac{m}{\Delta} x\right), \tag{2.13}$$

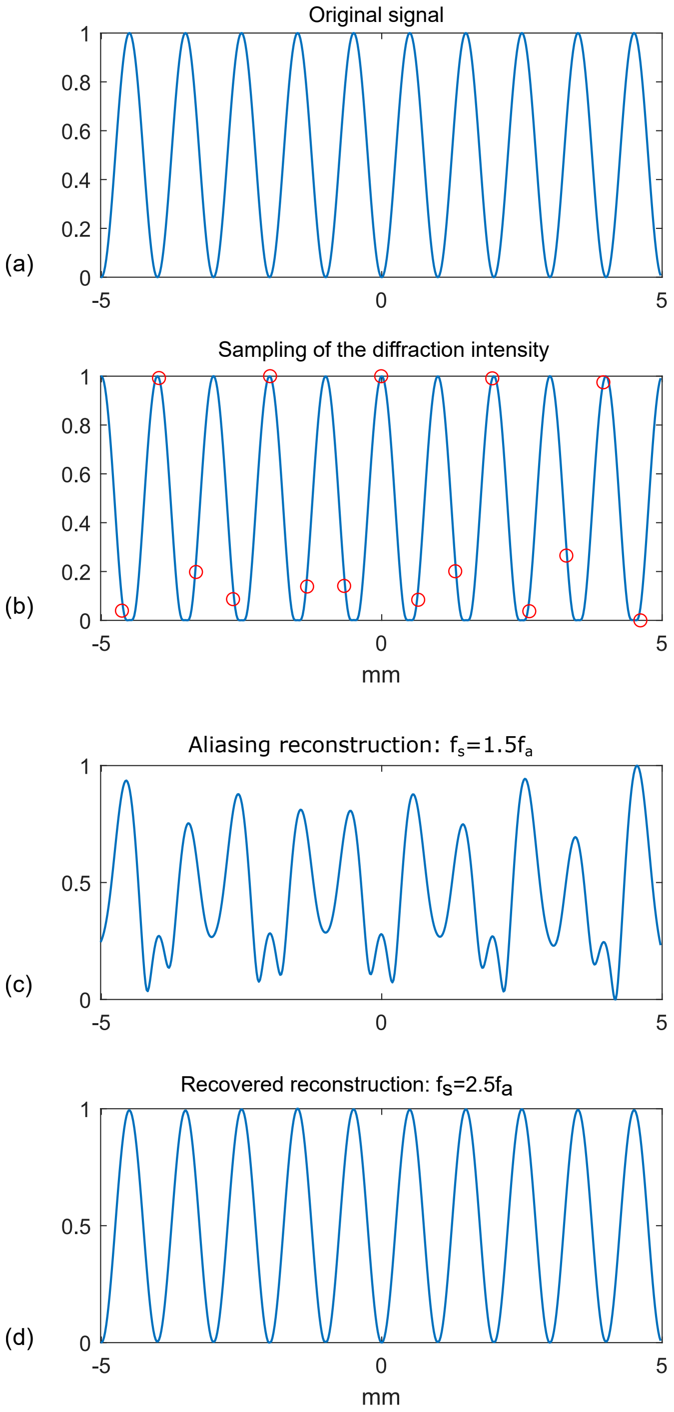

Figure 2.2: (a) shows a signal with a spatial frequency of f_a. It is propagated to a distance $z = 8\ m$ and sampled by different sampling rates as shown in (b). (c) and (d) show the reconstruction from the samples in the rates $1.5f_a$ and $2f_a$ respectively.

where

$$G(x) = \begin{cases} 1 & \text{if } x \in R, \\ 0 & \text{else}. \end{cases} \tag{2.14}$$

It is very interesting that this condition will sometimes break the Nyquist criterion which allows to sample the diffraction intensity with a lower frequency. They are two independent conditions.

To demonstrate it, here we use the same setting in the previous Section2.1.2. The signal is defined to have a limited size $L = 2\ mm$, as shown in Figure 2.3 (a). The $L < \lambda z f_s = 5\ mm$. In Figure 2.3 (b), the diffraction intensity is sampled at a frequency $f_s = 1.5 f_a$ with which the original signal can not be properly reconstructed in the previous case. However, the U_0 is fully recovered as shown in Figure 2.3 (c). We just have to filter out the original signal with the boundary $x \in [-L/2, L/2]$.

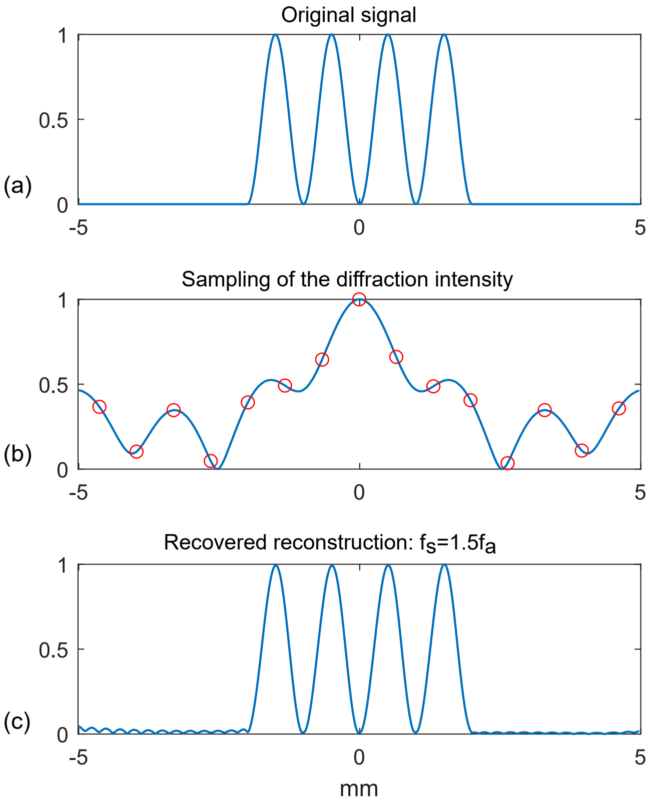

Figure 2.3: (a) shows a space limited signal with a spatial frequency f_a. (b) shows the diffraction intensity of the signal and its sampling points in the rate $1.5 f_a$. (c) shows the signal reconstructed from the samples.

When the optical signals are processed digitally, the choice of the sampling density needs to be investigated according to the geometry of the optical system. The two cases above show the aspects of consideration in the sampling constraints of the coherent optical field. In the first case, continuous band-limited signals can be recovered from the samples if they meet the Nyquist criterion. In the second case, the convolution kernel of the optical system, specifically the Fresnel transform for free space propagation, allows the fully reconstruction of a space-limited object from its diffraction intensity even when the field is severely under-sampled according to the Nyquist criteria. In practice, the space limited case corresponds to the source or object with limited size which are typical applications of optical field reconstruction such as the content of diffraction imaging and in-line holography. By knowing the minimum requirement of sampling rate without introducing any aliasing or other related artefact, we can greatly improve the efficiency of signal acquisition and reduce the burden of computation for signal processing or simulation. In the book of [3], Jason D. Schmidt provides details of a general guideline for choosing parameters for optics simulation in response to the sampling requirements.

2.2. Young's interferometry

In 1801, Thomas Young's famous double-slit interference experiment demonstrated the wave characteristic of light. As one of the most fundamental configurations of interferometry, it is widely used in spatial coherence test, wavelength measurement and many other applications. Usually, the interference phenomenon is described by geometrical optics. It can also be formulated by the theory of diffraction.

For simplicity, we first consider the propagation in (x, z) plane as depicted in Figure 2.4. A monochromatic and spatial coherent light beam illuminates an opaque screen with two pinholes x_1 and x_2. The separation between them is $d = x_1 - x_2$. The diffracted light propagates a distance L to an observation screen. The complex field in between can be modelled as the overlap of two sphere waves emitted from these two point sources. We assume that these point sources have the same amplitude but with different phases: $U(x_1, 0) = ae^{i\phi_1}$ and $U(x_2, 0) = ae^{i\phi_2}$. Since L is much larger than x', we can use the paraxial approximation. The complex field at a distance z expressed as $U(x, z)$ is the convolution of the initial field $U(x, 0)$ and the Fresnel diffraction spatial impulse response $h(x, z)$ which is:

$$h(x, z) = \frac{1}{i\lambda z} \exp(ikz) \exp\left(\frac{ik}{2z} x^2\right), \tag{2.15}$$

where λ is the wavelength of the monochromatic light, k is the wave number.

The field at a position (x', z) is then calculated by the superposition of these two

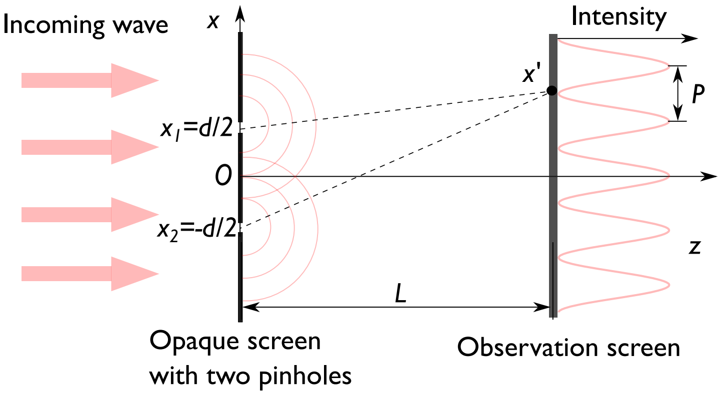

Figure 2.4: Young's double-slit interference experiment.

waves:

$$
\begin{aligned}
U\left(x',z\right) &= \left[U\left(x_1,0\right)+U\left(x_2,0\right)\right] * h\left(x',z\right)\\
&= \frac{a}{i\lambda z}\exp\left(ikz\right)\left\{\exp\left(i\phi_1\right)\exp\left[\frac{ik}{2z}\left(x'-x_1\right)^2\right]+\exp\left(i\phi_2\right)\exp\left[\frac{ik}{2z}\left(x'-x_2\right)^2\right]\right\}\\
&= \frac{a}{i\lambda z}\exp\left(ikz\right)\exp\left(i\phi_1\right)\left\{\exp\left[\frac{ik}{2z}\left(x'+\frac{d}{2}\right)^2\right]+\exp\left(i\Delta\phi\right)\exp\left[\frac{ik}{2z}\left(x'-\frac{d}{2}\right)^2\right]\right\}\\
&= \frac{a}{i\lambda z}\exp\left[i\left(kz+\phi_1\right)\right]\exp\left[\frac{ik}{2z}\left(x'^2+\frac{d^2}{4}\right)+\frac{i\Delta\phi}{2}\right]\\
&\qquad\times\left\{\exp\left[i\left(\frac{k}{2z}dx'-\frac{\Delta\phi}{2}\right)\right]+\exp\left[-i\left(\frac{k}{2z}dx'-\frac{\Delta\phi}{2}\right)\right]\right\}\\
&= \frac{2a}{i\lambda z}\exp\left[i\left(kz+\phi_1\right)\right]\exp\left[\frac{ik}{2z}\left(x'^2+\frac{d^2}{4}\right)+\frac{i\Delta\phi}{2}\right]\cos\left(\frac{kd}{2z}x'-\frac{\Delta\phi}{2}\right),
\end{aligned}
\tag{2.16}
$$

where $\Delta\phi = \phi_1 - \phi_2$ is the phase difference between these two point sources.

The intensity distribution on the observation screen is the square of modulus of the complex field:

$$
\begin{aligned}
I\left(x',L\right) = \left|U\left(x',L\right)\right|^2 &= \left(\frac{2a}{\lambda L}\right)^2\cos^2\left(\frac{kd}{2z}x'-\frac{\Delta\phi}{2}\right)\\
&= 2\left(\frac{a}{\lambda L}\right)^2\left[1+\cos\left(\frac{kd}{L}x'-\Delta\phi\right)\right].
\end{aligned}
\tag{2.17}
$$

Thus, the observed pattern is a sinusoidal fringe with a period of $P = \lambda L/d$. The phase difference is also encoded by shifting the fringe pattern. We can demodulate the interferogram to retrieve $\Delta\phi$. We Fourier transform $I(x,L)$:

$$\begin{aligned}\mathcal{F}\left[I(x,L)\right] &= 2\left(\frac{a}{\lambda L}\right)^2 \mathcal{F}\left\{1+\cos\left(\frac{kd}{L}x' - \Delta\phi\right)\right\} \\ &= \left(\frac{a}{\lambda L}\right)^2 \times \\ &\left\{2\delta\left(f_x\right) + \mathcal{F}\left[\exp\left(i\pi\frac{2d}{\lambda L}x\right)\exp\left(-i\Delta\phi\right) + \exp\left(-i\pi\frac{2d}{\lambda L}x\right)\exp\left(i\Delta\phi\right)\right]\right\} \\ &= \left(\frac{a}{\lambda L}\right)^2\left[2\delta\left(f_x\right) + \delta\left(f_x - \frac{d}{\lambda L}\right)\exp\left(-i\Delta\phi\right) + \delta\left(f_x + \frac{d}{\lambda L}\right)\exp\left(i\Delta\phi\right)\right].\end{aligned} \tag{2.18}$$

From equation 2.18, we can see that the phase difference is encodes in the phase of the side-lobes.

An example of two dimensional double-slit interference with phase differences between two sources is simulated in MATLAB by numerically propagation. Figure 2.5 is the pattern of the double slit. The bright spots represent these two pinholes. They are two horizontally arranged 5 μm square pixels and the distance in between is 50 μm.

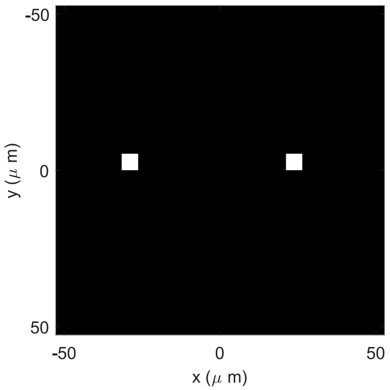

Figure 2.5: A sketch of two pinholes. The pinholes are simulated by two 5 μm by 5 μm square pixels. The distance between them is 50um. These two pixels share the same constant amplitude. The rest pixels are set to zeros.

The observation plane is 30 mm away from the pinholes. The wavelength we used in the simulation is 500 nm. Figure 2.6 shows two resulted interferograms in an area of 1.9 $mm \times 1.9\ mm$ on this plane. Figure 2.6 (a) is the interference of two point sources that have no phase difference. We can see that the sinusoidal intensity distribution is coincident with the analytical results in equation 2.17.

To investigate the effect of the phase difference between two point sources on the interference pattern. We assigned the initial phases 0 and $\pi/3$ to this two pixels respectively. Figure 2.6 (b) is resulting interferogram. Comparing the cross section of these two interferograms in Figure 2.7, we can observe a shift of the fringes. Fourier transform the interferogram, we obtained the Fourier spectrum and its phase map in Figure 2.8. The phases of the two side lobes are $\pm 0.98\ rad$, which is close to $\pi/3$ with discretization error in numerical calculations.

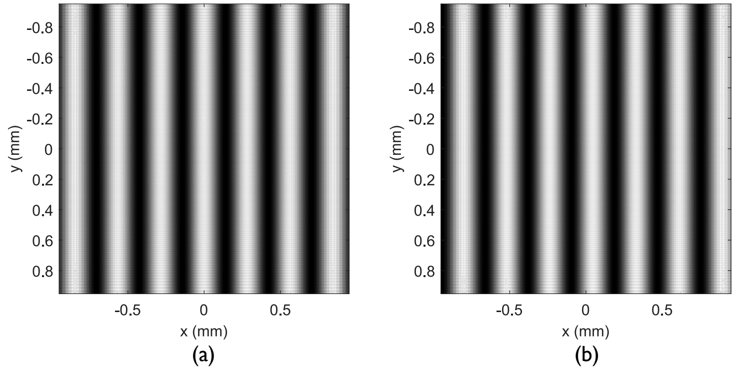

Figure 2.6: Interference patterns of the two pinholes. The physical size is 1.9 $mm \times 1.9\ mm$. (a) Two point sources with no phase difference. (b) Two point sources with a phase difference of $\pi/3$.

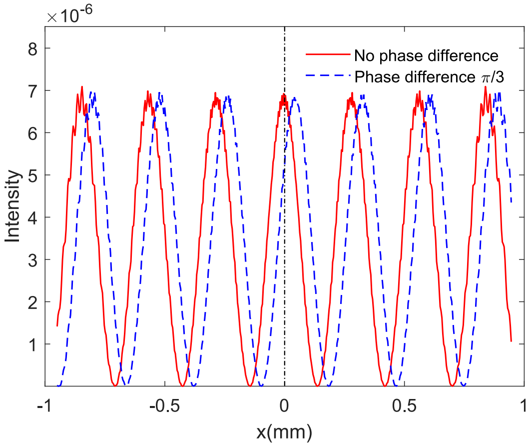

Figure 2.7: The intensity distributions in the centre of the two interferograms.

This simple demonstration shows a solution, both in optical geometry and signal processing, to measure the phase difference between two coherent points in space. The works in Chapter 3 are mainly based on this principle.

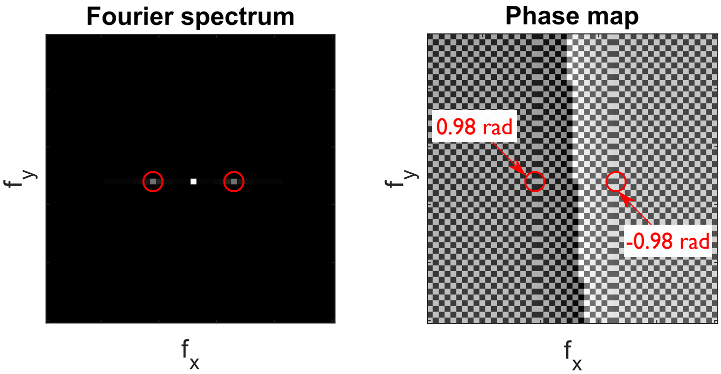

Figure 2.8: Fourier analysis of the interferograms. Left is the Fourier spectrum of the interferogram in Figure 2.6. Right is the phase map of the Fourier transform.

2.3. Shack-Hartmann wavefront sensor

The Shack-Hartmann wavefront sensor (SHWFS) is widely used in the field of adaptive optics and optical testing. It is composed of a lenslet array and an image sensor (CCD/ CMOS, PSD array etc.). Generally, all the lenslets are manufactured to have the same focal length. The image sensor is arranged in the focal plane of the lenslet array. This sensor originates from the work of Roland Shack in the beginning of the 20th century, and Ben Platt in 1971 [4].

An early form of this kind of sensors, named the Hartmann sensor, uses an array of pinhole before the image sensor. Modified from this Hartmann testing mask by adding lenslets, the SHWFS is more photon efficient, which makes it more suitable for low-light applications. Although, in the early stage, this wavefront sensor suffered from the limited lenslet numbers, the resolution has increased significantly with the development of microlens array fabrication technology.

In Figure 2.9, a basic form of SHWFS is shown. It contains a lenslet array, and a camera sensor is placed at its focal plane. Here we provide the numerical model of a SHWFS which is helpful for the later discussions of how to process the data from the sensor.

The lenslet array can be described as a phase grating $t(x, y)$:

$$t(x, y) = \left\{ \exp\left[-\frac{ik}{2F} \left(x^2 + y^2 \right) \right] P(x, y) \right\} * comb_{p,p}(x, y), \tag{2.19}$$

where F is the focal length of each lenslet. p is the pitch of the lenslet. $comb_{p,p}(x, y)$ is a two dimensional comb function with p as its period. The thickness of the lenslet array is ignored due to the uniform refractive index of the substrate layer and the relatively thin sagitta layer. $P(x, y)$ is the pupil function of a single lenslet.

To simplify the analysis, we assume there is no cross talk between neighbour lenslets

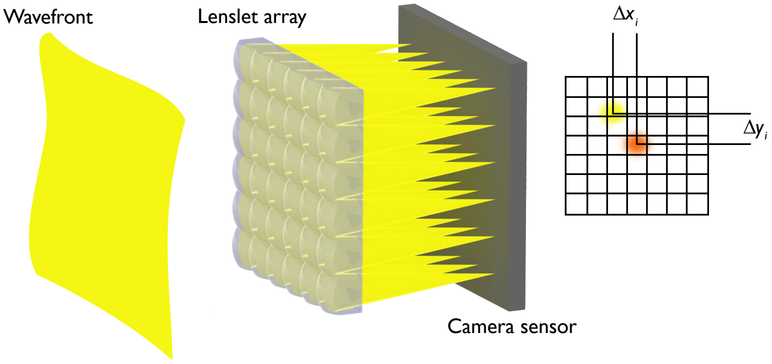

Figure 2.9: Schematic of a general Shack-Hartmann wavefront sensor.

as strictly defined in Ref. [5]. The local optical field before the lenslet has a linear wavefront and a uniform intensity:

$$U_0^{m,n}(x,y) = A\exp\left[ik\left(s_x^{m,n}x + s_y^{m,n}y\right)\right], \tag{2.20}$$

where A is the constant amplitude. Integers m and n indicate the point location of the lenslet. $s_x^{m,n}$, $s_y^{m,n}$ are the local gradients of the wavefront before the lenslet in two orthogonal directions:

$$s_x^{m,n} = \frac{\partial W^{m,n}(x,y)}{\partial x}, \tag{2.21}$$

$$s_y^{m,n} = \frac{\partial W^{m,n}(x,y)}{\partial y}. \tag{2.22}$$

The local optical field at the focal plane of the lenslet is approximated after a Fresnel propagation:

$$\begin{aligned} U_F^{m,n}(x',y') = \frac{1}{i\lambda F}\exp\left[\frac{ik}{2F}\left(x'^2+y'^2\right)\right] \iint A\exp\left[ik\left(s_x^{m,n}x + s_y^{m,n}y\right)\right] \times \\ \exp\left[-\frac{ik}{2F}\left(x^2+y^2\right)\right] P(x,y)\exp\left[\frac{ik}{2F}\left(x^2+y^2\right)\right] \times \\ \exp\left[-i\frac{2\pi}{\lambda F}\left(x'x+y'y\right)\right] dxdy \\ = \frac{A}{i\lambda F}\exp\left[\frac{ik}{2F}\left(x'^2+y'^2\right)\right] \tilde{P}\left(\frac{x'-s_x^{m,n}F}{\lambda F}, \frac{y'-s_y^{m,n}F}{\lambda F}\right), \end{aligned} \tag{2.23}$$

where x' and y' represent the coordinates in the focal plane.

From the result of equation 2.23, we can tell that the local gradients of the wavefront will shift the focal spot by $s_x^{m,n}F$ and $s_y^{m,n}F$ on the image sensor. Thus, the relationship between the local gradient of the (m,n) lenslet and its measured spot position shift $(\Delta x^{m,n}, \Delta y^{m,n})$ can be simply described as:

$$\frac{\partial W^{m,n}}{\partial x} = \frac{\Delta x^{m,n}}{F}, \; \frac{\partial W^{m,n}}{\partial y} = \frac{\Delta y^{m,n}}{F}. \tag{2.24}$$

With an incident plane wave, the light within the aperture of a lenslet is focused in the centre of the sub-region (as the red spot shown in the Figure 2.9). Then a spots array pattern (SH pattern) will be recorded by the camera. When the wavefront of incident light is distorted, these focal spots will be shifted from their centres.

If there is no cross talk, the SH pattern can be expressed as:

$$U_F(x', y') = \sum_m \sum_n U_F^{m,n}(x' - np, y' - mp). \tag{2.25}$$

Usually, the gradients of the wavefront are retrieved by comparing the SH pattern with a previously calibrated reference.

2.4. Wavefront slopes

Wavefront slope or the gradient of wavefront is essential for wavefront sensing. Many kinds of wavefront sensors, like the Hartmann sensor, Shack-Hartmann sensor, shearing interferometry sensors [6, 7], measure the wavefront slope information. Then the wavefront is reconstructed from the measurements indirectly.

Classically, the gradients are extracted from Shack-Hartmann (SH) pattern by using centroid method [8]. When the number of lenslets is small, direct calculation of the centroids within each sub-aperture is efficient enough. However, in the high resolution case, this process is cumbersome. Since the SH pattern is periodic, we can retrieve the spot shifts by Fourier processing which is more efficient. This method is introduced and extensively studied by E.N. Ribak [9, 10]. As frequently referenced tools, the centroid method and Fourier demodulation method are briefly introduced as follows.

2.4.1. Centroid method

The amount of shift can be indicate by the first moment of the region intensity, well known as centroid [11]:

$$x_c^{m,n} = \frac{\iint x' I_F^{m,n}(x', y') dx' dy'}{\iint I_F^{m,n}(x', y') dx' dy'}. \tag{2.26}$$

According to equation 2.20, the local optical field can be expressed as:

$$U_F^{m,n}(x', y') = \frac{1}{i\lambda F} \exp\left[\frac{ik}{2F}\left(x'^2 + y'^2\right)\right] \mathcal{F}\left\{U_0^{m,n}(x, y)P(x, y)\right\}\left(\frac{x'}{\lambda F}, \frac{y'}{\lambda F}\right). \tag{2.27}$$

Thus, the centroid position can also be expressed as:

$$\begin{aligned} x_c^{m,n} &= \frac{\iint x' \left|U_F^{m,n}(x',y')\right|^2 dx'dy'}{\iint \left|U_F^{m,n}(x',y')\right|^2 dx'dy'} \\ &= \lambda F \frac{\iint u \left|\mathcal{F}\left\{U_0^{m,n}(x,y)\right\}(u,v)\right|^2 dudv}{\iint \left|\mathcal{F}\left\{U_0^{m,n}(x,y)\right\}(u,v)\right|^2 dudv}, \end{aligned} \tag{2.28}$$

where $u = \frac{x'}{\lambda F}$, $v = \frac{y'}{\lambda F}$.

Using the derivative theorem of Fourier transform:

$$\mathcal{F}\left\{U_0^{m,n}(x,y)\right\}(u,v) = \frac{1}{i2\pi u}\mathcal{F}\left\{\frac{\partial U_0^{m,n}(x,y)}{\partial x}\right\}(u,v). \tag{2.29}$$

And applying this theorem to the equation 2.28:

$$\begin{aligned} x_c^{m,n} &= \frac{\lambda F}{i2\pi} \frac{\iint \mathcal{F}\left\{\frac{\partial U_0^{m,n}(x,y)}{\partial x}\right\}(u,v)\,\mathcal{F}\left\{U_0^{m,n*}(x,y)\right\}(u,v)\,dudv}{\iint \left|\mathcal{F}\left\{U_0^{m,n}(x,y)\right\}(u,v)\right|^2 dudv} \\ &= \frac{\lambda F}{i2\pi} \frac{\iint \frac{\partial U_0^{m,n}(x,y)}{\partial x} U_0^{m,n*}(x,y)dxdy}{\iint \left|U_0^{m,n}(x,y)\right|^2 dxdy}. \end{aligned} \tag{2.30}$$

The gradient of the optical field can be expressed as:

$$\frac{\partial U_0^{m,n}(x,y)}{\partial x} = iA\exp\left[i\phi^{m,n}(x,y)\right]\frac{\partial \phi^{m,n}(x,y)}{\partial x}. \tag{2.31}$$

By using Parseval theorem, we can rewrite $x_c^{m,n}$ as:

$$\begin{aligned} x_c^{m,n} &= \frac{\lambda F}{i2\pi} \frac{\iint_{sa} iA\exp\left[i\phi^{m,n}(x,y)\right]\frac{\partial\phi^{m,n}(x,y)}{\partial x}A\exp\left[-i\phi^{m,n}(x,y)\right]dxdy}{\iint_{sa}\left|A\exp\left[i\phi^{m,n}(x,y)\right]\right|^2 dxdy} \\ &= \frac{\lambda F}{2\pi S_{sa}} \iint_{sa} \frac{\partial\phi^{m,n}(x,y)}{\partial x}dxdy, \end{aligned} \tag{2.32}$$

where S_{sa} is the area of a lenslet sub-aperture. It can be seen that the position of the centroid at the focal plane and the phase of local wavefront are related.

Let $s_x^{m,n} = \iint_{sa}\partial\phi^{m,n}(x,y)/\partial x dxdy/(kS_{sa})$, we have

$$x_c^{m,n} = s_x^{m,n}F. \tag{2.33}$$

Comparing with expression 2.24, we can relate the centroid position with the wavefront slope. With this knowledge, here we introduce the method of obtaining the wavefront slope by a standard centroid approach:

1. **Pre-process of the SH image to reduce the effect of noise.** It includes:

removing the background brought by the environment photon and camera read-out noise; applying an adjustable threshold (usually be relative to the maximum intensity) to isolate the spots from the speckles [12, 13].

2. **Define and label the sub-aperture of each spot.** The image is divided into grids with fixed size according to the structure of the lenslet array or the distribution of the reference spots pattern. Their size could be larger than the physical size of a lenslet region to extend the dynamic range. This dynamic range can also be extended with adaptive algorithms [14, 15] .

3. **Centroid calculation.** The image of each sub-aperture is treated independently. Several known centroiding methods can be applied to estimate the spot position, such as center of mass, cross-correlation [16, 17] and matched filter [18] methods. The most used approach is calculating the center of mass. Then the discrete estimation of the spot position within the mth sub-aperture (x_c^m, y_c^m) can be calculated as:

$$x_c^m = \frac{\sum_{M,N} x_{M,N} I_{M,N}}{\sum_{M,N} I_{M,N}}, y_c^m = \frac{\sum_{M,N} y_{M,N} I_{M,N}}{\sum_{M,N} I_{M,N}}. \tag{2.34}$$

   Here M, N denote the numbers of pixels of each sub-aperture in two dimensions.

4. **Slope calculation.** When both the position of the current spot (x_c^m, y_c^m) and the position of its corresponding reference spot (x_r^m, y_r^m) are registered, the slopes of the sub-aperture can be obtained by knowing the relative spot displacement and the focal length of the lenslet:

$$s_x^m = \frac{x_c^m - x_r^m}{F}, \; s_y^m = \frac{y_c^m - y_r^m}{F}. \tag{2.35}$$

   Finally, the slopes can be registered with all sub-aptertures are processed with this centroid approach.

2.4.2. Fourier demodulation

The slopes can also be obtained globally by spatial demodulation of the whole image [9, 19, 20]. According to equation 2.25, the SH pattern of the incident light is a two-dimensional periodic function modulated by certain phase shift caused by the wavefront distortion. Assuming the pattern is an even function, it can be expressed by a sum of a series of cosine functions:

$$I_{sh}(x,y) = a_0 + \sum_{m,n} a_{m,n}\left[\cos\left(\frac{2\pi mx}{p} + \varphi_{m,n}(x)\right) + \cos\left(\frac{2\pi ny}{p} + \theta_{m,n}(y)\right)\right]. \tag{2.36}$$

where a_0 is a constant term, $a_{m,n}$ are the magnitude of sinusoidal harmonics. $\varphi_{m,n}(x)$ and $\theta_{m,n}(y)$ are phase shift.

All the spots are assumed circularly symmetric and equal. The fundamental frequency harmonics ($m = n = 1$) weights most in the geometric arrangement of focal spots. The high order harmonics defines the internal structure of the spots. Thus, we neglect the high frequencies and omit the constant term in the gradient demodulation process. The SH pattern is simplified to:

$$I_{sh}(x,y) \approx \cos\left(\frac{2\pi x}{p} + F\frac{\partial W(x,y)}{\partial x}\right) + \cos\left(\frac{2\pi y}{p} + F\frac{\partial W(x,y)}{\partial y}\right). \tag{2.37}$$

Here the gradients are assumed to be continuous between the measured spots which, by comparison, is sampled discretely in centroid method.

Fourier transform the SH pattern, we obtain:

$$\begin{aligned}
\mathcal{F}\left\{I_{sh}(x,y)\right\} \approx \frac{1}{2}\mathcal{F}\Bigg\{&\exp\left(\frac{i2\pi x}{p} + is_x F\right) + \exp\left(-\frac{i2\pi x}{p} - is_x F\right) + \\
&\exp\left(\frac{i2\pi y}{p} + is_y F\right) + \exp\left(-\frac{i2\pi y}{p} - is_y F\right)\Bigg\} \\
= \frac{1}{2}\Bigg[&\mathcal{F}\left\{\exp\left(is_x F\right)\right\}\delta\left(f_x - \frac{1}{p}, f_y\right) + \mathcal{F}\left\{\exp\left(-is_x F\right)\right\}\delta\left(f_x + \frac{1}{p}, f_y\right) + \\
&\mathcal{F}\left\{\exp\left(is_y F\right)\right\}\delta\left(f_x, f_y - \frac{1}{p}\right) + \mathcal{F}\left\{\exp\left(-is_y F\right)\right\}\delta\left(f_x, f_y + \frac{1}{p}\right)\Bigg].
\end{aligned} \tag{2.38}$$

In the Fourier domain, the harmonics are separated to the side lobes in the positions $(m/p, n/p)$ where $(m, n = 0, \pm 1, \pm 2, ...)$. If the lenslet pitch is small (or the number of lenslet is large in the same sensing area), then these components are well separated. Generally, the phase modulation frequency should be much smaller than the carrier wave frequency. Thus, the wavefront gradient is assumed to be much slower than the lenslet spatial frequency so that the typical frequency of the wavefront gradient stay within the sub-region of the side lobes. This is named adiabatic condition by Ribak in Ref. [9]:

$$\nabla^2 W(\mathbf{X}) \ll \nabla\left(\frac{2\pi\mathbf{X}}{p}\right)\Big/F. \tag{2.39}$$

It denotes that the detectable curvature of wavefront is limited by the pitch and focal length of a lenslet array. In general, this condition is more relaxed than the well-defined centroid method where no focal spot goes across to the other sub-aperture.

From equation 2.38, we find that the wavefront slope information is encoded in the first harmonics. Therefore, the slope information can be obtained by the following steps. Firstly, translate one of the side lobes (for example $\mathcal{F}\left\{\exp\left(ic_x F\right)\right\}\delta\left(f_x - 1/p, f_y\right)$) to the centre of Fourier domain along the x axis. It removes the lenslet frequency term in the δ function. Secondly, a low pass filter with a cut-off frequency f_c is applied to the Fourier domain to extract the term $\mathcal{F}\left\{\exp\left(is_x F\right)\right\}\delta\left(f_x, f_y\right)$. f_c defines the maximum frequency of the wavefront gradient. It should be smaller than the bandwidth of lenslet frequency. Finally, the phase of the inverse Fourier transform of the rest term is $s_x F$.

The straight forward steps of this Fourier demodulation method is:

1. Fourier transform the SH pattern.
2. Translate the first side lobe on the x axis to the centre.
3. Apply a low pass filter to the Fourier domain. The cut-off frequency satisfies the condition :$f_c \leqslant 1/2p$.
4. Inverse Fourier transform the filtered domain.
5. Extract the phase of the result, and unwrap it if phase discontinuity appears.
6. Divide the lenslet focal length to reveal the wavefront slope on axis x: $\partial W(x,y)/\partial x$.
7. Repeat the steps (2-6) for the first side lobe on the y axis to obtain the wavefront slopes on axis y: $\partial W(x,y)/\partial y$.

In this method, there is no rigid sub-aperture division process as did in the centroid method. The slopes are automatically interpolated. Three Fourier transforms are needed to obtain both x, y slopes. To speed up the method, Ribak further developed a direct demodulation technique to reduce Fourier transforms which is suited for large arrays. In experimental work it is used quite often as a fast method (Some condition should be satisfied: see [19]). The method is named the smoothing method with the following steps:

1. The SH pattern is multiplied with a phase term which relates to the size of the lenslet pitch:
$$E(x,y) = I_{sh}(x,y)\exp\left(-i2\pi x/N_{px}\right).$$
2. First smoothing by applying a sliding average in x and y axis:
$$E^{1x}(x,y) = \sum_{n=0}^{N_{px}-1} E\left(x+n-N_{px}/2, y\right)/N_{px},$$
$$E^{1y}(x,y) = \sum_{n=0}^{N_{py}-1} E^{1x}\left(x, y+n-N_{py}/2\right)/N_{py}.$$
3. Further smoothing with a second pass:
$$E^{2x}(x,y) = \sum_{n=0}^{N_{px}-1} E^{1y}\left(x+n-N_{px}/2, y\right)/N_{px},$$
$$E^{2y}(x,y) = \sum_{n=0}^{N_{py}-1} E^{2x}\left(x, y+n-N_{py}/2\right)/N_{py}.$$

4. The wavefront slope is calculated:

$$\partial W(x,y)/\partial x = \arg\left\{E^{2y}(x,y)\right\} N_p/2\pi F.$$

5. Same process with respect to the other axis to obtain the y slope.

In the expressions, N_{px} and N_{py} are the size of the rectangular region to be smoothed. They are usually chosen to be the grid of the SH pattern spots.

Choosing the demodulation algorithm depends on the applications. In high speed situations, the smoothing method is more suitable. But its accuracy is not as high as the full Fourier demodulation method which is more suitable for high precision case [10].

2.5. Wavefront reconstruction methods

Once the local wavefront gradients are registered, the wavefront can be reconstructed with various approaches. These approaches differ by processing the wavefront locally or globally, the reconstruction algorithms have been conventionally categorized into zonal methods and modal methods [21–23]. An introduction of these two wavefront reconstruction methods is as follows.

2.5.1. Zonal reconstruction

Zonal reconstruction is a kind of numerical integration. It was quite popular in the early days of adaptive optics due to its simplicity. The relationship between the wavefront and slopes can be formulated differently depends on the sampling geometry of slope measurements. In the Fried geometry [24], each lenslet of a SHWFS measures both the x and y slopes at the same point. The finite difference model can be expressed as:

$$\begin{aligned} s_x^{m,n} &= \frac{[W(m+1,n)+W(m+1,n+1)]-[W(m,n)+W(m,n+1)]}{2p}, \\ s_y^{m,n} &= \frac{[W(m,n+1)+W(m+1,n+1)]-[W(m,n)+W(m+1,n)]}{2p}, \end{aligned} \tag{2.40}$$

where $W(m,n)$ means the wavefront of subaperture (m,n), and p is the size of the uniformly arranged subaperture. By stacking the slopes of two dimensions into one vector $\mathbf{s}$, the measuring model in equation 2.40 can be vectorized as:

$$\mathbf{s} = \mathbf{G}\mathbf{W}, \tag{2.41}$$

where $\mathbf{W}$ are the stacked wavefront, $\mathbf{G}$ defines the finite difference structure, which is not limited to Fried geometry. Other alternatives such as Hudgin geometry and Southwell geometry, are chosen depending on the sampling principle in different applications [25]. If $\mathbf{G}$ has full rank, the solution of equation 2.41 is a pesudo-inverse:

$$\hat{\mathbf{W}} = \left(\mathbf{G}^T\mathbf{G}\right)^{-1}\mathbf{G}^T\mathbf{s}. \tag{2.42}$$

However, in general there are more unknowns than equations in equation set 2.41 which lead to a rank deficiency of $\mathbf{G}$. Thus, the $\mathbf{G}^T\mathbf{G}$ is not invertible, a singular value decomposition routine is used in practice:

$$\mathbf{G} = \mathbf{UDV}^T, \tag{2.43}$$

where $\mathbf{U}$ and $\mathbf{V}$ are orthogonal matrices, the singular values of $\mathbf{G}$ are stored on the diagonal of matrix $\mathbf{D}$. Then the solution of equation 2.41 is:

$$\hat{\mathbf{W}} = \mathbf{G}^+\mathbf{s}, \tag{2.44}$$

where $\mathbf{G}^+$ is the generalized pseudo-inverse calculated as:

$$\mathbf{G}^+ = \mathbf{VD}^{-1}\mathbf{U}^T. \tag{2.45}$$

A least squares solution with the effect of noise is also provided in Ref. [26].

2.5.2. Modal reconstruction

In the modal reconstruction method, the wavefront is expressed by a linear combination of a set of basis functions $P_n(x, y)$. These functions need to be continuous and the property of first analytic derivatives are required to be able to fit the slope measurement. Usually, these basis functions are orthogonal (Orthogonality) within the aperture which means the presence (or absence) of one order of $P(x, y)$ does effect the others. But, non-orthogonal basis functions are also used such as Taylor monomials [27]. The wavefront can be generally expressed as a compact notation:

$$W(x, y) = \sum_n a_n P_n(x, y), \tag{2.46}$$

where a_n are the coefficients of each basic function. The gradients can be written as:

$$\begin{aligned} \frac{\partial W(x, y)}{\partial x} &= \sum_n a_n \frac{\partial P_n(x, y)}{\partial x}, \\ \frac{\partial W(x, y)}{\partial y} &= \sum_n a_n \frac{\partial P_n(x, y)}{\partial y}. \end{aligned} \tag{2.47}$$

The functions of gradients provide a model of the slope measurements. Then, the comparison between them can be used to define an objective function, such as an error function:

$$\varepsilon^2 = \sum\left(s_x - \sum_n a_n \frac{\partial P_n(x, y)}{\partial x}\right)^2 + \sum\left(s_y - \sum_n a_n \frac{\partial P_n(x, y)}{\partial y}\right)^2. \tag{2.48}$$

Then the coefficients a_n can be solved by least squares fitting or other optimization methods. Choosing the type of basis functions largely depends on the applications. In many cases, it is related to the shape of aperture and computational complexity.

The wavefront surface of a rectangular aperture can be described by the product of two Legendre polynomials [21, 28, 29]:

$$W(x,y)=\sum_{n=0}^{N}\sum_{m=0}^{M}a_{n,m}P_n(x)\,P_m(y), \tag{2.49}$$

where

$$\begin{aligned} P_n(x)&=\sum_{k=0}^{K}(-1)^k\frac{(2n-2k)!}{2^n k!\,(n-k)!\,(n-2)!}z^{n-2k},\\ P_m(y)&=\sum_{k=0}^{K}(-1)^k\frac{(2m-2k)!}{2^m k!\,(m-k)!\,(m-2)!}z^{m-2k}. \end{aligned} \tag{2.50}$$

The Legendre polynomials are orthogonal over the square area defined by : $|x|<1,\ |y|<1$.

The most frequently used basis functions are Zernike polynomials [22, 30]. They are orthogonal over a unit circle. The reason of their popularity is that they are closely related to the aberrations arise in the optical systems. For instance, their low order terms directly describe the parameters such as tip/tilt, defocus, astigmatism, coma and spherical aberrations. A normalized wavefront described in the polar coordinate system (r,θ) by the Zernike polynomials is provided in equation 2.51:

$$W(r,\theta)=\bar{W}+\sum_{n=2}^{\infty}A_{n0}R_n^0(r)+\sum_{n=1}^{\infty}\sum_{m=1}^{n}R_n^m\left[A_{nm}\cos(m\theta)+B_{nm}\sin(m\theta)\right], \tag{2.51}$$

where $\bar{W}$ are the mean wavefront. A_{nm} and B_{nm} are the Zernike coefficients. The radial polynomial R_n^m can be written as

$$R_n^m(r)=\sum_{j=0}^{(n-m)/2}(-1)^j\frac{(n-j)!}{j!\left(\frac{n+m}{2}-j\right)!\left(\frac{n-m}{2}-j\right)!}r^{n-2j}. \tag{2.52}$$

The integers n and m in equations 2.51 and 2.52 are respectively known as the radial and azimuthal wave number. $n\geqslant m$ and $n-m$ must be an even number.

There are many Zernike polynomial variations such as annular Zerinke polynomials for optical systems with central obscurations [31] and complex-valued Zernike polynomials in forming the phase retrieval problmes as introduced in [32, 33].

The wavefront can also be decomposed by complex exponential functions since they are orthogonal over rectangular apertures [34]. With this representations, the problem can be handled with the highly efficient Fast Fourier transform (FFT) algorithm. According to Ref. [35], the computational complexity of Fourier reconstruction is $O(n\log n)$ while the Zernike reconstruction is $O\left(n^2\right)$. The performance comparison between the Fourier reconstruction and Zernike reconstruction has been done in the works [36, 37]. Generally, the Fourier reconstruction can achieve a better performance in terms of speed and reconstruction error.

In this dissertation, the retrieved Shack-Hartmann data are mainly in a rectangular shape and real-time processing is preferred. Thus, we process them mostly with Fourier reconstruction. The details of this method is introduced as follows.

Fourier reconstruction

Considering the wavefront is a combination of a series of orthogonal sinusoidal function basis:

$$W(x,y) = \sum_{m=0}^{N}\sum_{n=0}^{M} a_{m,n}(x,y)\exp\left[i2\pi\left(xn/M + ym/N\right)\right]. \tag{2.53}$$

Express it in the form of Fourier transform in a continuous manner:

$$W(x,y) = \iint \tilde{W}(f_x,f_y)\exp\left[i2\pi\left(xf_x + yf_y\right)\right] df_x df_y \tag{2.54}$$

Taking partial derivatives of the wavefront with respect to x and y, we obtain:

$$\begin{aligned} \frac{\partial W(x,y)}{\partial x} &= i2\pi \iint f_x\tilde{W}(f_x,f_y)\exp\left[i2\pi\left(xf_x + yf_y\right)\right] df_x df_y, \\ \frac{\partial W(x,y)}{\partial y} &= i2\pi \iint f_y\tilde{W}(f_x,f_y)\exp\left[i2\pi\left(xf_x + yf_y\right)\right] df_x df_y. \end{aligned} \tag{2.55}$$

Again we express the wavefront gradients in the form of a Fourier transform, we have

$$\begin{aligned} \frac{\partial W(x,y)}{\partial x} &= \iint \tilde{s}_x(f_x,f_y)\exp\left[i2\pi\left(xf_x + yf_y\right)\right] df_x df_y, \\ \frac{\partial W(x,y)}{\partial y} &= \iint \tilde{s}_y(f_x,f_y)\exp\left[i2\pi\left(xf_x + yf_y\right)\right] df_x df_y. \end{aligned} \tag{2.56}$$

Comparing the two groups of equations 2.55 and 2.56, we can find the relations that:

$$\begin{aligned} \tilde{s}_x(f_x,f_y) &= i2\pi f_x\tilde{W}(f_x,f_y), \\ \tilde{s}_y(f_x,f_y) &= i2\pi f_y\tilde{W}(f_x,f_y). \end{aligned} \tag{2.57}$$

To solve this equation, multiply f_x , f_y to both sides respectively and add them together yielding:

$$f_x\tilde{s}_x(f_x,f_y) + f_y\tilde{s}_y(f_x,f_y) = i2\pi\left(f_x^2 + f_y^2\right)\tilde{W}(f_x,f_y). \tag{2.58}$$

Therefore, the Fourier transform of the wavefront can be written as:

$$\tilde{W}(f_x,f_y) = \frac{f_x\tilde{s}_x(f_x,f_y) + f_y\tilde{s}_y(f_x,f_y)}{i2\pi\left(f_x^2 + f_y^2\right)}. \tag{2.59}$$

So once the slopes are obtained, we can calculate the wavefront with the equation

2.59. This method is especially suitable for a rectangular pupil. For the circular pupil, the boundary needs to be defined and the help of iterative processing [35, 38].

Modal methods are generally superior to zonal methods in suppression of the error propagation, especially when the data set is noisy. Also, modal methods, for instance, the Zernike methods, are able to present the dominant aberrations which are convenient for optical system assessment.

2.6. Phase retrieval

Besides the interferometric and wavefront sensing techniques, phase retrieval is also an important group of techniques used to recover the phase of an object from intensity only measurements [39]. These intensities can be obtained in various of ways such as being captured at different planes on the optical path or registered with introduced additive phases in the concept of phase diversity. It generally requires no sophisticated setups as in holography and relies more on numerical computations. These methods can be mainly categorized into the transport-of-intensity equation (TIE) methods, optimization based methods, and alternating projection methods. A brief review of these methods are described as follows. Then we will emphasize on the details in Gerchberg-Saxton algorithm which has been implemented with the digital micro-mirror device in Chapter 3.

2.6.1. Transport-of-intensity equation (TIE)

This category of methods retrieves the phase of a plane from several closely spaced intensity measurements of the adjacent planes by deterministically solving the transport-of-intensity equation:

$$k\frac{\partial I(\mathbf{r},z)}{\partial z} = -\nabla_{\perp}\cdot\left[I(\mathbf{r},z)\nabla_{\perp}\phi(\mathbf{r})\right], \tag{2.60}$$

where k is the wavenumber, $\mathbf{r}=(x,y)$ is a two-dimensional vector in the transverse direction. $I(\mathbf{r},z)$ is the intensity distribution in the space. $\nabla_{\perp}$ denotes the lateral gradient operator which is normal to z, the beam propagation direction. The TIE can be derived from many methods, such as a small propagation distance approximation of the Fresnel propagation or directly from the Helmholtz equation under paraxial approximation [40, 41].

The TIE denotes the relationship between the spatial phase $\phi(\mathbf{r})$ and the axial derivative of the intensity $\partial I(\mathbf{r},z)/\partial z$. With a minimum of two intensity measurements $I(z)$ and $I(z+dz)$ of two planes with an interval distance dz, $\partial I(\mathbf{r},z)/\partial z$ can be approximated as:

$$\frac{\partial I(\mathbf{r},z)}{\partial z} = \frac{I(z+dz)-I(z)}{dz}. \tag{2.61}$$

Then a variety of methods can be applied to solve $\phi(\mathbf{r})$ from this partial differential equation with appropriate boundary conditions and assumptions [40, 42, 43]. One frequently mentioned method from Teague's work is assuming the transverse flux

$I(\mathbf{r}, z)\nabla_\perp \phi(\mathbf{r})$ is conservative. An auxiliary function ψ is introduced that satisfies:

$$\nabla\psi(\mathbf{r}) = I(\mathbf{r}, z)\nabla\phi(\mathbf{r}). \tag{2.62}$$

Then the TIE is transformed into a Poisson equation:

$$k\frac{\partial I(\mathbf{r}, z)}{\partial z} = -\nabla_\perp^2 \psi(\mathbf{r}). \tag{2.63}$$

The phase $\phi(\mathbf{r})$ can be determined by solving the equation 2.63 and then integrating ψ. The solution is given by the following expression

$$\phi(\mathbf{r}) = -k\nabla_\perp^{-2}\nabla_\perp \cdot \left[I^{-1}(\mathbf{r}, z)\nabla_\perp \nabla_\perp^{-2} \frac{\partial I(\mathbf{r}, z)}{\partial z} \right], \tag{2.64}$$

where $\nabla_\perp^2$ is the inverse Laplacian operator.

The basic TIE method only requires several intensity measurements at different planes along the propagation direction and their interval distances. The optical setup is straightforward and easy to implement. Also, this method is able to measure the phase with lowly coherent light, which makes it a good alternative method when the interferometric methods are not applicable. Consequently, it is able to avoid the speckle noise brought by the highly coherent light and suitable for applications that prefer partially coherent light such as conventional microscopes.

However, the corresponding boundary condition are usually based on *a priori* knowledge which are difficult to obtain in practice. Severe artefacts will appear when the actual experimental conditions violate the working assumptions. The boundary error is considered one of the major obstacle for the TIE in the high precision phase measurement applications. Other parameters of TIE methods, such as the interval distances, the signal-to-noise ratio, also affect the recovery accuracy as discussed in the work [44].

2.6.2. Optimization based methods

Phase retrieval problems are increasingly considered from the view of optimization, especially in the field of phase diversity. Considering a complex object $O = A\exp(i\phi)$ is imaged by an optical system with a diverse group of point spread functions (PSFs) $h^1, h^2, ..., h^j$. The corresponding images are $I^1, I^2, ..., I^j$. For the jth measurement with detection noise n, we have

$$I^j = \left| h^j * O \right|^2 + n. \tag{2.65}$$

The goal is to estimate O from all the measurements with given PSFs. Then the phase retrieval problem can be formulated as an minimization problem:

$$\min_O \sum_{j=1}^{M} \left\| I^j - \left| h^j * O \right|^2 \right\|_2^2. \tag{2.66}$$

Many non-linear optimization techniques based different searching strategies, such as gradient methods, trust-region methods [39, 45], are explored to find an acceptable solution. This intensity-based cost function is non-convex. In general, it doesn't guarantee the convergence to the target. Thus, increasing the number of measurements M with diverse PSFs can reduce the solutions that satisfy the equation.

Recently, processing this problem with convex programs based on semidefinite programming (SDP) relaxations is gaining popularity. Different relaxation techniques, such as PhaseLift [46], and PhaseCut [47], have been developed. In many cases, the SDPs provide good theoretical guarantees of the convergence. Also, the numerical calculation can benefit from many standard convex optimization solvers, e.g. CVX. However, this method generally requires matrix lifting, which means replacing the target vector with a higher-dimension matrix. This treatment will highly increase the cost of computation [48].

In many real-time applications, such as adaptive optics, the computing time is expected to be reduced. Thus, the phase is usually modeled by a linear combination of Zernike polynomials:

$$\phi(x, y) = \sum_{n=1}^{N} \alpha_n Z_n(x, y), \tag{2.67}$$

where $Z_n(x, y)$ is the nth polynomial in the Zernike basis expansion. Then the problem is converted to minimize equation 2.66 with respect to the Zernike coefficients α_n which could much reduce the scale of the calculations.

2.6.3. Iterative methods

Iterative methods are also called alternating projection methods in the view of mathematician. If we have known intensity measurements of at least a pair planes or one measurement and a support region, along with the transfer functions in between of the planes, we can reconstruct the complex amplitude of the object by the back-and-forth numerical propagation of the optical fields.

The pioneering work was done by Gerchberg and Saxton [49], and is known as the Gerchberg-Saxton algorithm(GS). Later there were many modified versions to improve this algorithm in terms of convergence efficiency, accuracy or complexity, such as steepest-descent method, gradient search method, and Hybrid Input-Output (HIO) algorithm which is introduced by Fienup in his one of the most frequently cited papers in optics [50].

Gerchberg-Saxton algorithm

The Gerchberg-Saxton algorithm is one of the first practical iterative approaches to solve the phase retrieval problem with the Fourier field involved. The classical GS algorithm recovers the complex amplitude field from the intensity measurements of the front focal (object) plane and back focal (Fourier) plane of a lens as depicted in the Figure 2.10. The measured intensities are I_1 and I_2 respectively. In this case, the propagation from the object to the focal plane is a Fourier transform. The optical field is projected between these two planes alternatively until the computed optical field satisfies the object constrains or the Fourier constraints. This iterative procedure is described in algorithm 1:

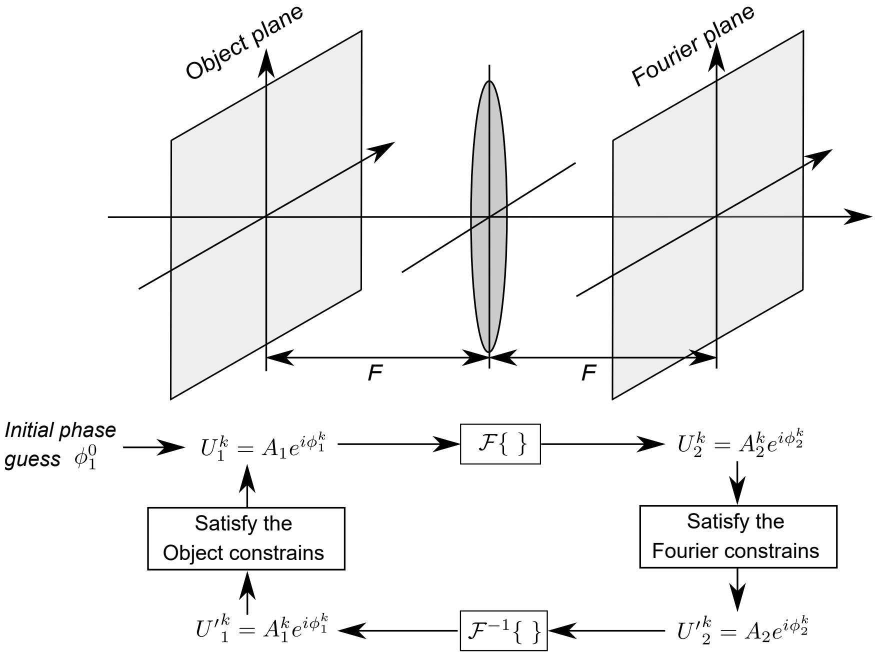

Figure 2.10: Scheme of the Gerchberg-Saxton algorithm.

In the algorithm, e_2^k represents the squared error in the Fourier domain of the the kth iteration. Correspondingly, the squared error in object domain is defined as

$$e_1^k = \sum \left| U_1^{k+1} - U'^k_1 \right|^2 . \tag{2.69}$$

By using Parseval's theorem, we know that

$$\begin{aligned} e_2^k &= N^{-2} \sum \left| U'^k_2 - U_2^k \right|^2 \\ &= \sum \left| \mathcal{F}\left\{ U'^k_2 \right\} - \mathcal{F}\left\{ U_2^k \right\} \right|^2 \\ &= \sum \left| U_1^k - U'^k_1 \right|^2 . \end{aligned} \tag{2.70}$$

Both U_1^k and U_1^{k+1} satisfy the object constraints. In the definition, the U_1^{k+1} is the nearest value to U'^{k+1}_1. Therefore, from equation 2.69 and equation 2.70, we have

$$e_2^k \geqslant e_1^k . \tag{2.71}$$

Algorithm 1 The GS algorithm

Input:

$A_1 = \sqrt{I_1}$: Magnitude of the object plane.
$A_2 = \sqrt{I_2}$: Magnitude of the Fourier plane.
ε : An error threshold.

Output:

ϕ_1^{end} - The recovered phase of the object optical field after the iterations.

Initialization:

Give an initial phase value ϕ_1^0 to form the object optical field $U_1 = A_1 e^{i\phi_1^0}$. Generally, the phase is chosen randomly. Also, the initialization is not limit to start from the object plane. The iteration loop starts from the estimated field U_2 is equivalent.

Iterative steps:

For the kth cycle :

1. Fourier transform the current estimated $U_1^k = A_1 e^{i\phi_1^k}$ to obtain $U_2^k = A_2^k e^{i\phi_2^k}$.
2. Keep the phase ϕ_2^k and replace the magnitude with the measured data A_2 to form the new estimated field at the Fourier plane $U'^{k}_{2} = A_2 e^{i\phi_2^k}$ (satisfying the Fourier constraints).
3. Inverse Fourier transform the recombined U'^{k}_{2} to obtain the estimated $U'^{k}_{1} = A_1^k e^{i\phi_1^{k+1}}$.
4. Keep the phase ϕ_1^{k+1} and replace the magnitude with the measured value A_1 to form the new estimated field at the object plane $U_1^{k+1} = A_1 e^{i\phi_1^{k+1}}$.

The loop will not stop until a phase ϕ_1^{end} is achieved that satisfies the condition:

$$e_2^k = N^{-2} \sum \left| U_2^k - U'^{k}_{2} \right|^2 \leqslant \varepsilon, \tag{2.68}$$

where N is the number of sampling points.

Similarly, applying Parseval's theorem to equation 2.69

$$\begin{aligned} e_1^k &= \sum \left| U_1^{k+1} - U'^{k}_{1} \right|^2 \\ &= N^{-2} \sum \left| \mathcal{F}\left\{U_1^{k+1}\right\} - \mathcal{F}\left\{U'^{k}_{1}\right\} \right|^2 \\ &= N^{-2} \sum \left| U_2^{k+1} - U'^{k}_{2} \right|^2 . \end{aligned} \tag{2.72}$$

Since U'^{k+1}_{2} is the nearest value to U_2^{k+1}, it can be found that

$$e_1^k \geqslant N^{-2} \sum \left| U_2^{k+1} - U'^{k+1}_{2} \right|^2 = e_2^{k+1}. \tag{2.73}$$

Combining equation 2.71 with equation 2.73 yields the relation that

$$e_2^{k+1} \leqslant e_1^k \leqslant e_2^k. \tag{2.74}$$

From the above analysis, we know the GS algorithm is an error-reduction algorithm. The error with the constrainsts is monotonically decreasing. It suggests that the algorithm may converge to a solution if the constraints are convex. However, in practice the constraints in either object domain or Fourier domain are usually non-convex. Thus, the algorithm probably stagnates in a stationary point which leads to a local minimum.

Many experiments show the GS algorithm usually reduces the error fast for the first iterations. However, the convergence speed becomes much slower for the later iterations [51–53]. Also, the GS algorithm is not suitable for the problem with a single intensity measurement and support information as many researches suggest. Thus, later there are many modifications of the GS algorithm to overcome the trapping and stagnation problem. One of the most popular approach is proposed by J. R. Fienup [54] with the help of prior information, such as the constraints of the input and output.

Among all these iterative methods, the alternating projection algorithm, as a more generalized category of GS algorithms, is still popular in applications, though its theoretical understanding is still under investigation. In many optical applications, the measurement process performs as a low-pass filter. A practical algorithm needs to restore the missing phases of the optical field and resolve the fine details of the data. Many of the current approaches are based on inefficient SDP schemes or lack comprehensive theoretical analysis [55, 56]. Recently, the algorithms base on sparsity is gaining popularity as well [57]. Here we skip the introduction of them since they are not the main works relate to the work of this dissertation.

2.7. Phase unwrapping

In many signal processing situations, such as synthetic aperture radar, interferometry, holography and wavefront sensing techniques, we need to extract the phase of a complex signal. The calculation is usually returned by the arctangent function which gives the value in the range $(-\pi, \pi]$. However, the actual value typically exceeds this range, thus the phase is wrapped. One or multiple 2π discontinuities may appear between adjacent pixels even though the physical signal phase is continuous and smooth. This discontinuity is sometimes an obstacle for recovering the actual information. Thus, when such a discontinuity is detected, a phase unwrapping process $\mathcal{U}\{\ \}$ need to be carried out:

$$\hat{\phi}(x, y) = \mathcal{U}\{\phi(x, y)\} = \phi(x, y) + 2\pi N, \tag{2.75}$$

where $\hat{\phi}(x, y)$ is the unwrapped phase, $N = 0, \pm 1, \pm 2, \ldots.$

Figure 2.11 shows an example of phase unwrapping for a one dimensional spherical phase:

$$\phi(n) = 20\left(\frac{n}{256} - 1\right)^2 , \tag{2.76}$$

where n is the sampling index up to 512. The radian of the phase is defined to be larger than 2π. Thus, the phase is wrapped as shown in Figure 2.11 (b). Applying a simple rule to unwrap the phase: if the difference between a sample and its succeeding sample is larger than π, then a value of 2π is added to all the following samples. If this difference is smaller than -2π, then the added value is -2π. Figure 2.11 (c) gives the unwrapped phase with this explicit rule. The spherical curve is recovered perfectly by removing all the abrupt jumps due to the phase wrapping.

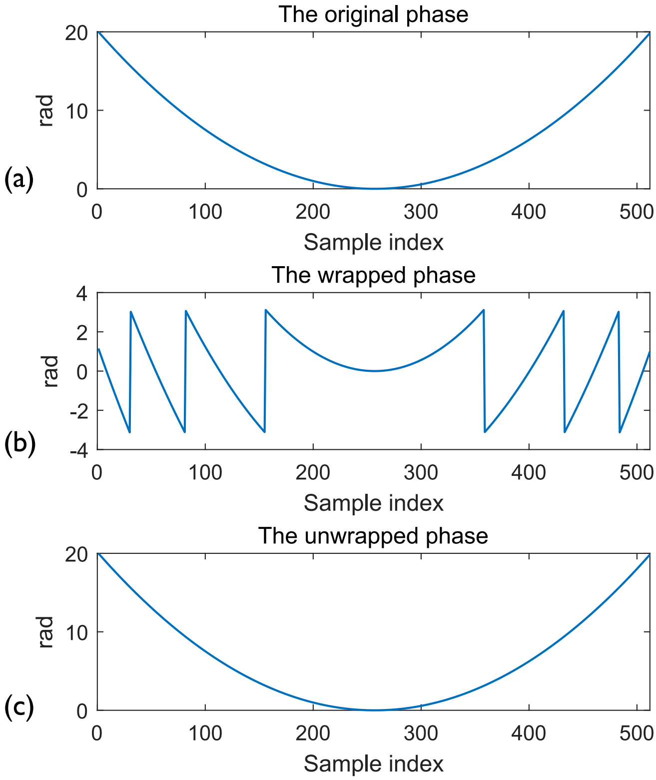

Figure 2.11: (a) shows a continuous phase having a range exceeds 2π. (b) shows the wrapped phase of (a). (c) shows the phase unwrap results with the compensating algorithm by simply detecting the phase jumping value.

However, this process can be very challenging in practice. It is because the unwrapping process can be ambiguous due to the noise ratio, sampling rate, and the physical discontinuities contained in the signal. All of these factors lead to the difficulty in distinguishing between genuine phase wraps and fake phase wraps. As a demonstration, amount of white noise with an amplitude of 0.75 *rad* is added to the previous signal as shown in Figure 2.12 (a). The same unwrapping algorithm fails at a certain position which is labelled out in figure Figure 2.12 (c). And this error propagates to the following phase data. The phase unwrapping problem becomes more complicated when it comes to two-dimensional cases where the residues (the integration result depends on the path around residues) may present. It is a vital problem for many wavefront sensing and imaging applications. Thus, many sophisticated algorithms have been proposed during decades of study.

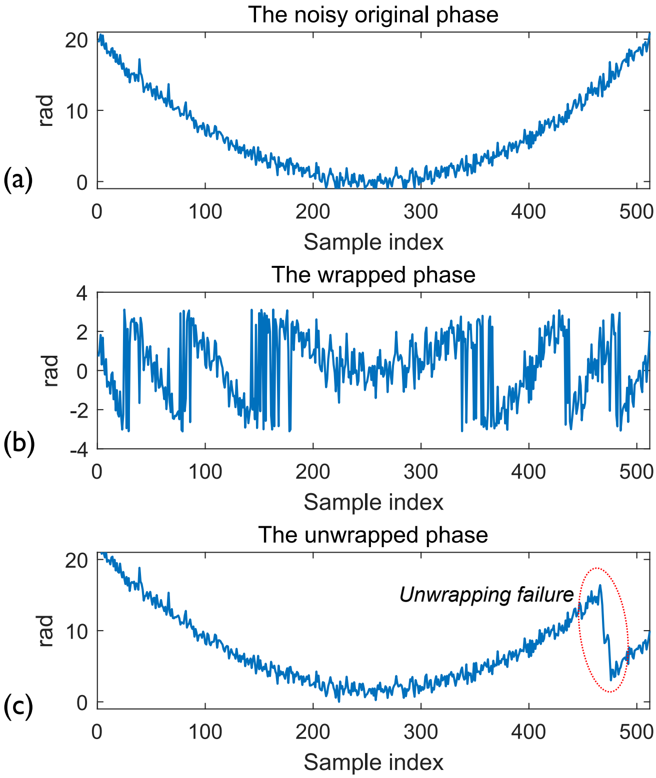

Figure 2.12: (a) shows the same phase as Figure 2.11 (a) with noise added. (b) shows the wrapped phase of (a). (c) shows the phase unwrap results with the same algorithm as in Figure 2.11.

These different types of algorithms can be roughly classified into the following categories: global algorithms, regional algorithms and path-following algorithms.

2.7.1. Global algorithms

The basic idea behind the global algorithms is formulating the phase unwrapping problem into a generalized minimum L_p-norm problem. The phase field is sought to minimize the global error function as shown below:

$$\varepsilon^p = \|solution - problem\|^p. \tag{2.77}$$

One of the most frequently mentioned method is unweighted least-squares method. Its cost function is defined as follows:

$$\varepsilon^2 = \int \left[\Delta\hat{\phi}_x - \mathcal{W}\left(\Delta\phi_x\right)\right]^2 dx + \int \left[\Delta\hat{\phi}_y - \mathcal{W}\left(\Delta\phi_y\right)\right]^2 dy, \tag{2.78}$$

where $\Delta\hat{\phi}_x$ and $\Delta\hat{\phi}_y$ are the gradients of estimated unwrapped phase. $\Delta\phi_x$ and $\Delta\phi_y$ are the gradients of the measured phase. $\mathcal{W}[\ ]$ is the wrapping operator that wraps the phase into the range $(-\pi, \pi]$. It can be efficiently solved by using fast Fourier transform (FFT) methods [58], discrete cosine transform (DCT) methods [59] and multigrid algorithms [59]. The techniques with FFTs or DCTs can offer a direct solution by solving the Poisson's equation as defined as:

$$\begin{aligned} P\left(m,n\right) &= \left(\Delta^x_{m,n} - \Delta^x_{m-1,n}\right) + \left(\Delta^y_{m,n} - \Delta^y_{m,n-1}\right) \\ &= \left[\phi\left(m+1,n\right) - 2\phi\left(m,n\right) + \phi\left(m-1,n\right)\right] + \\ &\qquad \left[\phi\left(m,n+1\right) - 2\phi\left(m,n\right) + \phi\left(m,n-1\right)\right]. \end{aligned} \tag{2.79}$$

For example, in one of the FFT based methods, a $M \times N$ grid wrapped phase $\phi(m,n)$, here $m \in [0, M]$, $n \in [0, N]$, is extended to a periodic function $\Phi(m', n')$ by applying a mirror reflection with respect to both the x and y axes. As a result the grid is extended to $m' \in [0, 2M]$, $n' \in [0, 2N]$. Then the extended unwrapped phase field $\hat{\Phi}(m', n')$ can be efficiently calculated by:

$$\hat{\Phi}(m', n') = \mathcal{F}^{-1}\left\{\frac{\tilde{P}_{m',n'}}{2\cos\left(\pi m'/M\right) + 2\cos\left(\pi n'/N\right) - 4}\right\}, \tag{2.80}$$

where $\tilde{P}_{m',n'}$ is the Fourier transform of the Poisson function $P_{m',n'}$ in equation 2.79. The unwrapped phase $\phi_{m,n}$ is then obtained by restricting the result to the grid of original phase map.

The unweighted least-squares algorithms can provide a smooth solution in a high speed. This feature makes it suitable for some applications like testing the mirror deformation in adaptive optics. However, this algorithm exploits all the information in the data with no difference. As a result, the solution can be strongly effected by the presence of residues. Therefore, it is inappropriate for those applications which require exact results or contain sharp features.

To reduce the effect of residues or other unreliable pixels, an reliable quality map V is preferred to weight the error function. For instance, in a two-dimensional least-squares problem, the weighted version can be expressed as:

$$\varepsilon^2 = \int V_x \left[\Delta\hat{\phi}_x - \mathcal{W}\left(\Delta\phi_x\right)\right]^2 dx + \int V_y \left[\Delta\hat{\phi}_y - \mathcal{W}\left(\Delta\phi_y\right)\right]^2 dy, \tag{2.81}$$

where V_x and V_y are predetermined reliable quality maps. The weighted least-squares problem is usually solved by implementing the unweighted method iteratively. Although this process increases the robustness, a longer execution time is the price to pay as a result.

2.7.2. Regional algorithms

To tackle concerns about the error propagation issue in the global algorithms, the regional algorithms such as region-based [60, 61] and tile-based [62] phase unwrappers were developed. The difference between these two is how the sub-regions are identified.

The region algorithms first separate the pixels into different regions, where within each region the phase is continuous. It is generally done by comparing the phase between the adjacent pixels. If the phase difference is below an adjustable threshold, then these pixels are assigned to the same region. After this sorting process, different regions are phase unwrapped by applying phase shift with respect to the neighbour region to remove the discontinuities.

In the tile-based algorithms, the phase map is divided into number of tiles and each tile is categorized into different classes by checking whether phase wrapping problem presents within it. After the preliminary test, each tile is unwrapped individually, and later they are recombined into the complete unwrapped phase by means such as minimizing an error function at the interfaces only [63].

In these regional algorithms, the phase is unwrapped within the local region independently, thus the error propagation is limited to a small area. Generally, they provide a good compromise between robustness and computational cost.

2.7.3. Path-following algorithms

Path-following algorithms generally integrate the phase in a sequence of steps by following a chosen path. The phase unwrapping process from one point to another is path-independent if the integral along any closed path C is zero:

$$\oint_C \boldsymbol{\phi}\left(\boldsymbol{r}\right) d\boldsymbol{r} = 0. \tag{2.82}$$

If the condition 2.82 is satisfied, the problem of two-dimensional phase unwrapping can be reduced to the problem of path invariance of the unwrapping. However, due to the noise or the presence of edges, such a path integral can yield a non-zero value, which is called residue, as mentioned previously. This phase inconsistency can be detected if the residue charge q is non-zero, which can be calculated as the sum of the phase difference around it:

$$
\begin{aligned}
q &= \sum_{m=1}^{4} \Delta_m \\
&= [\phi(m, n+1) - \phi(m, n)] + [\phi(m+1, n+1) - \phi(m, n+1)] - \\
&\qquad [\phi(m+1, n+1) - \phi(m+1, n)] - [\phi(m+1, n) - \phi(m, n)] \,.
\end{aligned}
\tag{2.83}
$$

According to different strategies in choosing the integral path and handling the residues, these algorithms can be subdivided into three groups [63]: (1) path-dependent methods, (2) residue-compensation methods and (3) quality-driven methods.

The path-dependent methods generally apply to the noiseless situations. The integral path are preliminary defined, such as linear scan, spiral scan and multiple scan direction. These methods have a very fast process speed. However, the presence of residues on the fixed path can easily corrupt the correct integration.

To overcome the problem, the residue-compensation methods is developed. It firstly generates a branch-cut by connecting the nearest opposite sign residues. Then the wrapping process is carried out by following a path which will not cross the branch-cut. They are also very efficient in calculation, but an inappropriately placed branch-cut may isolate some phase zones which will lead to phase discontinuity in the reconstruction.

In the quality-driven methods, the unwrapping order is guided by the pixel reliability. Thus, the lowest reliable data are limited in spreading errors. These methods usually contains two steps: First define a phase quality function based on various rules, such as correlation coefficients, phase derivative variance [64] or fringe modulation [65]. Then design the unwrapping path guided by the quality map: normally the highest quality pixels are unwrapped first and the lowest quality pixels last. In practice, the quality-driven algorithms have a good balance between robustness and computation efficiency.

Here we briefly introduce a quality-driven algorithm based on sorting by reliability following a non-continuous path (SRNCP), which is deployed frequently in our experiments. In this algorithm, the possibility of phase inconsistencies is detected by calculation the second differences D, which usually measures the degree of concavity/convexity of a function. For a pixel in the image, it is calculated as:

$$
D(m, n) = \left[H^2(m, n) + V^2(m, n) + {D_1}^2(m, n) + {D_2}^2(m, n)\right]^{1/2}, \tag{2.84}
$$

where $H(m, n)$, $V(m, n)$, $D_1(m, n)$ and $D_2(m, n)$ are the second differences of the horizontal, vertical and two diagonal directions respectively, as defined below:

$$\begin{aligned} H(m,n) &= \mathcal{U}\left[\phi(m-1,n)-\phi(m,n)\right]-\mathcal{U}\left[\phi(m,n)-\phi(m+1,n)\right], \\ V(m,n) &= \mathcal{U}\left[\phi(m,n-1)-\phi(m,n)\right]-\mathcal{U}\left[\phi(m,n)-\phi(m,n+1)\right], \\ D_1(m,n) &= \mathcal{U}\left[\phi(m-1,n-1)-\phi(m,n)\right]-\mathcal{U}\left[\phi(m,n)-\phi(m+1,n+1)\right], \\ D_2(m,n) &= \mathcal{U}\left[\phi(m-1,n+1)-\phi(m,n)\right]-\mathcal{U}\left[\phi(m,n)-\phi(m+1,n-1)\right]. \end{aligned} \tag{2.85}$$

Generally, the pixels are more reliable if their second differences are lower. Therefore, the reliability of a pixel can be defined as:

$$R = \frac{1}{D}. \tag{2.86}$$

Then, the reliability of an edge is defined as the sum of the reliablities of two connected pixels. Both the vertical and horizontal edges are calculated. The edges are then sorted by reliability which also determines the unwrapping priority. There is a grouping process along with the phase unwrapping. Initially, all the pixels are not in any group. The rules in table 2.1 are applied when an edge formed by two pixels ϕ_1 and ϕ_2 are unwrapped.

Condition	Process
ϕ_1 and ϕ_2 do not belong to any group.	Unwrap the pixel that belongs to the smallest group with respect to any pixel in the largest group, and join the two groups together.
ϕ_1 and ϕ_2 belong to different groups.	Unwrap both pixels with respect to each other and join them into a single group.
ϕ_1 belongs to a group and ϕ_2 does not belong to any group .	Unwrap ϕ_2 with respect to ϕ_1 and join ϕ_2 to this group. The operation will be inverted if ϕ_1 and ϕ_2 are swapped in the condition.

Table 2.1: The strategy of different cases in unwrapping an edge.

The process in the table 2.1 keeps running until all the pixels are stored into a single group. This algorithm works very robust and fast in most of our experimental data that includes holographic results and wavefront slopes.

Despite the many progresses of phase unwrapping algorithms that have been made, we have to note that no algorithm is perfect. Each of them may only be effective in solving one specific problem. Compromises are unavoidable in handling practical problem.

References

[1] K. A. Grebenyuk, *Classical sampling theorem in digital holography,* Journal of Physics: Conference Series **536**, 0 (2014).

[2] L. Onural, *Sampling of the diffraction field,* Applied Optics **39**, 5929 (2000).

[3] J. D. Schmidt, *Numerical simulation of optical wave propagation with examples in MATLAB,* (SPIE Bellingham, Washington, USA, 2010).

[4] B. C. Platt and R. Shack, *History and Principles of Shack-Hartmann Wavefront Sensing,* Journal of Refractive Surgery **17**, 573 (2001).

[5] J. Primot, *Theoretical description of Shack-Hartmann wave-front sensor,* Optics Communications **222**, 81 (2003).

[6] P. Bon, G. Maucort, B. Wattellier, and S. Monneret, *Quadriwave lateral shearing interferometry for quantitative phase microscopy of living cells.* Optics express **17**, 13080 (2009).

[7] J. J. L. Jaramillo, N. Vasset, and M. Ansorg, *Wavefront Sensing: From Historical Roots To the Stateoftheart,* EAS Publications Series **30**, 10 (2008).

[8] S.-H. Baik, S.-K. Park, C.-J. Kim, and B. Cha, *A center detection algorithm for Shack–Hartmann wavefront sensor,* Optics & Laser Technology **39**, 262 (2007).

[9] Y. Carmon and E. N. Ribak, *Phase retrieval by demodulation of a Hartmann-Shack sensor,* Optics Communications **215**, 285 (2003).

[10] C. Canovas and E. N. Ribak, *Comparison of Hartmann analysis methods,* Applied Optics **46**, 1830 (2007).

[11] G. Cao, *Accuracy analysis of a Hartmann-Shack wavefront sensor operated with a faint object,* Optical Engineering **33**, 2331 (1994).

[12] J. W. Hardy, *Adaptive optics for astronomical telescopes*, Vol. 16 (Oxford University Press, 1998).

[13] S. Thomas, *Optimized centroid computing in a Shack-Hartmann sensor,* Advancements in Adaptive Optics **5490**, 1238 (2004).

[14] C. Leroux and C. Dainty, *A simple and robust method to extend the dynamic range of an aberrometer,* Optics Express **17**, 19055 (2009).

[15] H. Shinto, Y. Saita, and T. Nomura, *Shack–Hartmann wavefront sensor with large dynamic range by adaptive spot search method,* Applied Optics **55**, 5413 (2016).

[16] L. A. Poyneer and B. Macintosh, *Spatially filtered wave-front sensor for high-order adaptive optics,* Journal of the Optical Society of America A **21**, 810 (2004).

[17] S. Thomas, T. Fusco, A. Tokovinin, M. Nicolle, V. Michau, and G. Rousset, *Comparison of centroid computation algorithms in a Shack-Hartmann sensor,* Monthly Notices of the Royal Astronomical Society **371**, 323 (2006).

[18] O. Lardière, R. Conan, R. Clare, C. Bradley, and N. Hubin, *Performance comparison of centroiding algorithms for laser guide star wavefront sensing with extremely large telescopes,* Applied Optics **49**, G78 (2010).

[19] A. Talmi and E. N. Ribak, *Direct demodulation of Hartmann-Shack patterns.* Journal of the Optical Society of America. A, Optics, image science, and vision **21**, 632 (2004).

[20] V. P. Lukin, N. N. Botygina, O. N. Emaleev, and P. A. Konyaev, *Wavefront sensors and algorithms for adaptive optical systems,* Adaptive Optics Systems II **7736**, 773659 (2010).

[21] W. Southwell, *Wave-front estimation from wave-front slope measurements,* Journal of the Optical Society of America **70**, 998 (1980).

[22] R. Cubalchini, *Modal wave-front estimation from phase derivative measurements,* Journal of the Optical Society of America **69**, 972 (1979).

[23] L. Seifert, H. J. Tiziani, and W. Osten, *Wavefront reconstruction with the adaptive Shack-Hartmann sensor,* Optics Communications **245**, 255 (2005).

[24] D. L. Fried, *Least-square fitting a wave-front distortion estimate to an array of phase-difference measurements,* Journal of the Optical Society of America **67**, 370 (1977).

[25] C. Correia, C. Kulcsar, J.-M. Conan, and H.-F. Raynaud, *Hartmann modelling in the discrete spatial-frequency domain: application to real-time reconstruction in adaptive optics,* Proceedings of SPIE **7015**, 701551 (2008).

[26] M. Verhaegen, G. Vdovin, and O. Soloviev, *Control for High Resolution Imaging* (TU Delft, Delft, 2015).

[27] P. R. Riera, *Efficient computation with special functions like the circle polynomials of Zernike,* Proceedings of SPIE **4769**, 130 (2002).

[28] K. Doyle, V. Genberg, and G. J. Michels, *Integrated Optomechanical Analysis,* Vol. 692 (2003) p. 2003.

[29] E. Kewei, C. Zhang, M. Li, Z. Xiong, and D. Li, *Wavefront reconstruction algorithm based on legendre polynomials for radial shearing interferometry over a square area and error analysis,* Optics Express **23**, 20267 (2015).

[30] R. J. Noll, *Zernike polynomials and atmospheric turbulence,* Journal of the Optical Society of America **66**, 207 (1976).

[31] V. N. Mahajan, *Zernike annular polynomials and optical aberrations of systems with annular pupils.* Applied optics **71**, 8125 (1981).

[32] O. T. A. Janssen, S. van Haver, A. Janssen, J. J. M. Braat, P. Urbach, and S. F. Pereira, *Extended Nijboer-Zernike (ENZ) based mask imaging: Efficient coupling of electromagnetic field solvers and the ENZ imaging algorithm,* Optical Microlithography Xxi, Pts 1-3 **6924**, 92410 (2008).

[33] J. Antonello, *Optimisation-based wavefront sensorless adaptive optics for microscopy,* (2014).

[34] K. R. Freischlad and C. L. Koliopoulos, *Modal estimation of a wave front from difference measurements using the discrete Fourier transform,* Journal of the Optical Society of America A **3**, 1852 (1986).

[35] G. M. Dai, *Wavefront optics for vision correction*, February (SPIE Press, 2008) p. 366.

[36] G. M. Dai, *Comparison of wavefront reconstructions with Zernike polynomials and Fourier transforms.* Journal of Refractive Surgery (2006), 10.3928/1081-597X-20061101-21.

[37] G. Yoon, S. Pantanelli, and S. MacRae, *Comparison of Zernike and Fourier wavefront reconstruction algorithms in representing corneal aberration of normal and abnormal eyes,* Journal of Refractive Surgery **24**, 582 (2008).

[38] G. M. Dai, *Modified Hartmann-Shack wavefront sensing and iterative wavefront reconstruction,* **2201**, 562 (1994).

[39] R. A. Gonsalves, *Phase retrieval and diversity in adaptive optics,* Optical Engineering **21**, 829 (1982).

[40] M. R. Teague, *Deterministic phase retrieval: a Green's function solution,* Journal of the Optical Society of America **73**, 1434 (1983).

[41] P. J. McMahon, E. D. Barone-Nugent, B. E. Allman, and K. A. Nugent, *Quantitative phase-amplitude microscopy II: Differential interference contrast imaging for biological TEM,* Journal of Microscopy **206**, 204 (2002).

[42] L. J. Allen and M. P. Oxley, *Phase retrieval from series of images obtained by defocus variation,* (2001).

[43] C. Zuo, Q. Chen, and A. Asundi, *Transport of intensity equation: a new approach to phase and light field,* Holography, Diffractive Optics, and Applications VI **9271**, 92710H (2014).

[44] D. Paganin, A. Barty, P. J. Mcmahon, and K. A. Nugent, *Quantitative phase-amplitude microscopy. III. The effects of noise,* Journal of Microscopy **214**, 51 (2004).

[45] A. Polo, H. P. Urbach, T. U. Delft, and D. U. o. T. Tu Delft, *Adaptive Optics for EUV Lithography: Phase Retrieval for Wavefront Metrology,* (2014).

[46] E. J. Candès, T. Strohmer, and V. Voroninski, *PhaseLift: Exact and Stable Signal Recovery from Magnitude Measurements via Convex Programming,* Communications on Pure and Applied Mathematics **66**, 1241 (2013).

[47] I. Waldspurger, A. D'Aspremont, and S. Mallat, *Phase recovery, MaxCut and complex semidefinite programming,* Mathematical Programming (2013), 10.1007/s10107-013-0738-9.

[48] E. J. Candès, Y. C. Eldar, T. Strohmer, and V. Voroninski, *Phase retrieval via matrix completion,* Electrical Engineering **abs/1109.0**, 1 (2011), arXiv:1109.0573 .

[49] R. W. Gerchberg and W. O. Saxton, *A practical algorithm for the determination of phase from image and diffraction plane pictures,* Optik **35**, 237 (1972).

[50] J. R. Fienup, *Phase retrieval algorithms: a comparison,* Applied Optics **21**, 2758 (1982).

[51] G. Z. Yang, B. Z. Dong, B. Y. Gu, J. Y. Zhuang, and O. K. Ersoy, *Gerchberg-Saxton and Yang-Gu algorithms for phase retrieval in a nonunitary transform system: a comparison.* Applied optics **33**, 209 (1994).

[52] F. Meng, D. Zhang, X. Wu, and H. Liu, *A comparison of iterative algorithms and a mixed approach for in-line X-ray phase retrieval,* Optics Communications **282**, 3392 (2009), arXiv:NIHMS150003 .

[53] C. Guo, C. Shen, J. Tan, X. Bao, S. Liu, and Z. Liu, *A robust multi-image phase retrieval,* Optics and Lasers in Engineering **101**, 16 (2018).

[54] J. R. Fienup, *Reconstruction of an object from the modulus of its Fourier transform,* Optics Letters **3**, 27 (1978).

[55] T. Bendory, R. Beinert, and Y. C. Eldar, *Fourier Phase Retrieval: Uniqueness and Algorithms,* , 1 (2017).

[56] K. Jaganathan, Y. C. Eldar, and B. Hassibi, *Phase Retrieval: An Overview of Recent Developments,* , 1 (2015), arXiv:1510.07713 .

[57] T. Strohmer, *Measure what should be measured: progress and challenges in compressive sensing,* (2012), arXiv:arXiv:1210.6730v1 .

[58] M. D. Pritt and J. S. Shipman, *Least-Squares Two-Dimensional Phase Unwrapping Using FFT's,* IEEE Transactions on Geoscience and Remote Sensing (1994), 10.1109/36.297989.

[59] D. Kerr, G. H. Kaufmann, and G. E. Galizzi, *Unwrapping of interferometric phase-fringe maps by the discrete cosine transform,* Applied Optics (1996), 10.1364/ao.35.000810.

[60] J. J. Gierloff, *Phase unwrapping by regions,* Society of Photo-Optical Instrumentation Engineers (SPIE) Conference Series **818**, 2 (1987).

[61] K. M. Hung, S. Precision, T. Yamada, S. Corporation, O. D. Division, and C. Peripherals, *Phase unwrapping by regions using least- squares approach,* , 2965 (2013).

[62] P. Stephenson, *Data validation techniques in a tiled phase unwrapping algorithm,* Optical Engineering **33**, 3703 (1994).

[63] A. Baldi, *Two-dimensional phase unwrapping by quad-tree decomposition,* **40** (2001).

[64] Y. Lu, X. Wang, and X. Zhang, *Weighted least-squares phase unwrapping algorithm based on derivative variance correlation map,* Optik **118**, 62 (2007).

[65] W. S. Li, *Phase unwrapping algorithm based on phase fitting reliability in structured light projection,* Optical Engineering **41**, 1365 (2002).

3

Sampling the optical field with a spatial amplitude modulator

We have experimentally demonstrated a lensless coherent microscope based on direct registration of the complex optical field by sampling the pupil with a sequence of two-point interferometers formed by the digital micro-mirror device. Complete registration of the complex amplitude in the pupil of imaging system, without any reference beam, provides a convenient link between the experimental and computational optics. Unlike other approaches to digital holography, our method does not require any external reference beam, resulting in a simple and robust registration setup. Computer analysis of the experimentally registered field allows for focusing the image in the whole range from zero to infinity, and for virtual correction of the aberrations present in the real optical system, by applying the adaptive wavefront corrections to its virtual model. An accelerated scheme by scanning binary masks with the principle of phase retrieval has been proposed and numerically verified.

Parts of this chapter have been published in Journal of Optics **17**(12), 122001, 2015 [1] and SPIE conference proceedings [2].

3.1. Introduction

Reconstruction of an object by methods of digital holography [3] requires the complex amplitude of the field to be known with high spatial resolution. A number of indirect techniques for registering the optical complex amplitude have been developed. Methods of digital holography, including phase-shift interferometry [4–6] require the reference beam to be present in the system. Such a reference beam can be internally generated by spatial filtering of a portion of the object beam [7, 8], or through the use of light from an empty area of the field of view [9].

Reconstruction of the phase from the intensity of the diffracted field [10–12] generally represents an ill-posed problem, and requires some additional information about the object to be made available. Reconstruction of the wavefront without a reference beam is possible with a Shack-Hartmann sensor [13].

A recent publication [14] describes a quadriwave lateral shearing interferometer for high-resolution field reconstruction. However, methods based on the phase reconstruction from wavefront tilts usually reconstruct only the potential component of the phase, neglecting phase vortices. Also, a relatively uniform intensity distributions needs to be present in the plane of reconstruction. These two factors significantly limit the applicability of these methods to digital holography.

Time multiplexing [15, 16] represents another useful approach to high-resolution reconstruction of the complex fields. In this approach, the complex amplitude is registered sequentially in different locations of the pupil. This is usually achieved through complex setups requiring a reference beam and a galvanometric or piezoelectric scanner.

In this chapter we propose an alternative and more straightforward time multiplexing technique for the sampling of the wavefront for registration of both the amplitude and the phase of the optical field. The technique operates without any reference beam and without any imaging lens or microscope objective, providing micrometer-scale resolution that is comparable to previously reported techniques [7–9, 14, 16]. The method can be divided into two branches. Main difference between them is the scanned pattern of spatial amplitude modulation. The first one scans two-pixel masks to form a series of Young's interferometers. The second projects randomized masks to retrieve speckle patterns. The reconstruction processes differ from each other as well. Here we first briefly introduce the spatial amplitude modulator we used, and then both of these two time multiplexing optical field sampling methods in the following sections.

3.2. Digital micro-mirror device as a spatial amplitude modulator

The digital micro-mirror device (DMD) initially developed by Texas Instrument for image projection, have been used as an image plane sampling device in spectrometry and laser beam characterization [17, 18]. The digital micro-mirror device (DMD) in Figure 3.1 can function as a programmable binary amplitude modulator. It contains an array of up to millions of independent tilt-able aluminium micro-mirrors. Each mirror having a size of micrometers is mounted on a hinge over a CMOS electronics as shown in Figure 3.1 (a). These mirrors, driven by the electro-static force created by the underlying electrodes, can rotate either a certain angle ($10 - 12°$) or the opposite to the normal of the DMD surface corresponding to an 'on' or 'off' state. The refreshing rate of all the micro-mirror states can be fast in the order of kHz. Thus, the DMD enables a fast and high precision control of the amplitude of light. The DMDs were initially commercialized by Texas Instruments for Digital Light Processing (DLP) projectors due to their high reflective efficiency, high contrast ratio and high resolution properties. Besides the success in the display market, the applications in non-display technologies are also emerging. In recent years, many wavefront sensing and imaging techniques have been carried out with the help of DMDs [17, 19–21].

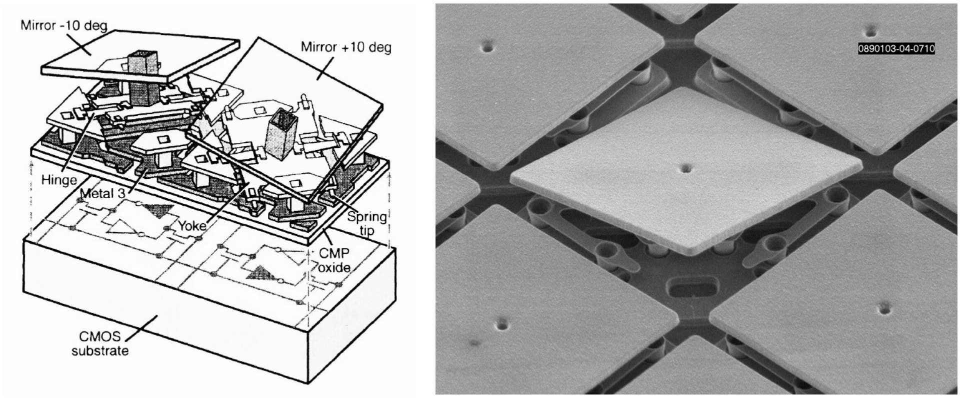

(a)

(b)

Figure 3.1: (a) The sketch of two DMD pixels [22]. (b) DMD is shown under an electron microscope [23].

3.3. Scanning two-point interferometers

In this section, we mainly describe the use of the DMD for sampling the optical field in the pupil plane by a series of Young's interferometers, dynamically formed by the micro-mirrors of a DMD.

Figure 3.2 explains the principle of registration of the complex amplitude for the case of transmissive object, however the same principle can be realized for reflective and scattering objects. The light beam emitted by the laser and scattered by the object, forms a speckle pattern on the surface of the DMD. The DMD device samples the field by turning on only two (reference and sample) micro-mirrors, to form a two-point interferometer. The fringe pattern is registered in the focal Fourier plane of the collective lens. The phase of the fringe pattern, with respect to the origin, is equal to the phase difference between the sample and reference micro-mirrors. The phase

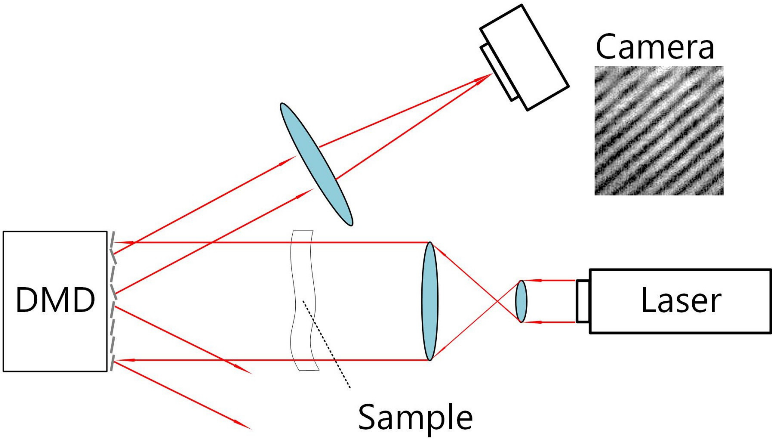

Figure 3.2: Coherent imaging setup based on field sampling with the use of DMD.

of the fringe pattern can be easily calculated by making the Fourier transform of the image, and then by calculating the phase in one of sidelobe maxima (refer to Section 2.2). The complete sequence, resulting in the registration of the complex amplitude of the field in all points corresponding to micro-mirrors with indices (i, j) and coordinates $x = i\delta, y = j\delta$, where δ is the pitch of the DMD, is given below:

- Choose the reference micro-mirror by scanning the intensity profile. To ensure high visibility of the interference pattern, the reference micro-mirror should be placed in an area with high intensity, for instance in a bright speckle. The reference micro-mirror stays in the 'on' position during the whole registration process for all pixels in the aperture.

- Turn on the sample micro-mirror with coordinates (x, y) and register the interference pattern in the focal plane of the collective lens. Example interferograms obtained with different micro-mirror pairs are shown in Figure 3.3.

- Process the fringe pattern, to find the phase $\varphi_r(x, y)$ corresponding to the fundamental harmonic in the registered fringe pattern. This can be done by Fourier transforming the image and calculating the phase in one of two sidelobes. Register the intensity in the sample point $I_r(x, y)$ by calculating the total intensity in the registered fringe pattern.

- Go to the next sample micro-mirror, and proceed until field intensity and phase are registered for all points of interest.

Since all micro-mirrors, except the two that are used for interferometry, are in the 'off' state, the reflected beam can be used for conventional imaging during the whole registration procedure.

The systematic phase errors are caused by the aberrations and misalignments in the path of the registration system, by the geometry of DMD, by the image noise and

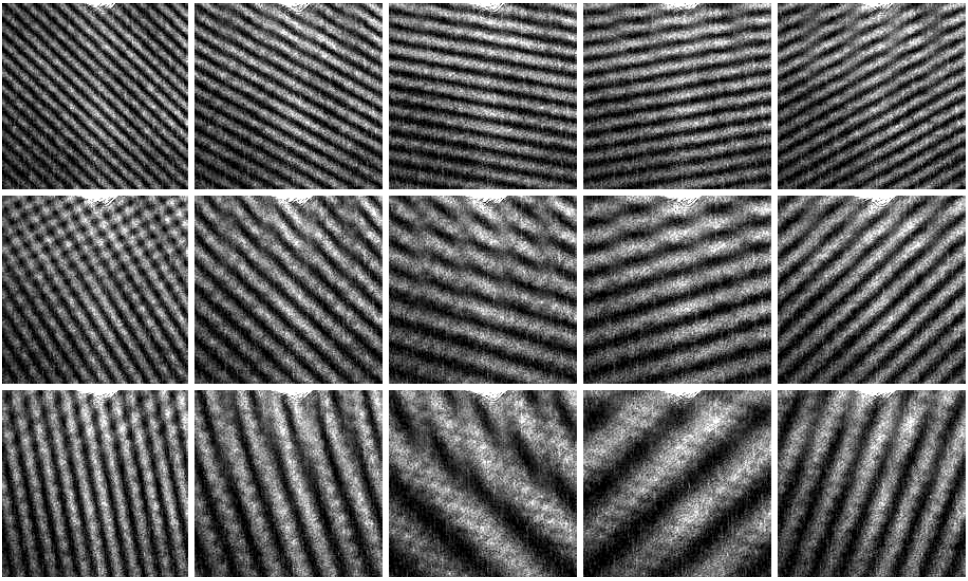

Figure 3.3: Interferograms obtained experimentally for different positions of the sampling micro-mirror.

the limited size of the imaged area in the Fourier plane. The major systematic error is caused by the grating-like geometry of the DMD. The 'on' pixels reflect incoming light at the angle of $\phi = 24^\circ$ in the sagittal (horizontal) plane, introducing path difference of $\Delta\varphi = x\sin(\phi) \approx 0.407x$ where x is the pixel coordinate in the sagittal plane. To enable a correct registration of the complex amplitude, the coherence length of the source L_c should satisfy the condition $L_c \gg 0.407A_x$, where A_x is the full size of the registered field in the sagittal plane.

To account for all systematic aberrations, we calibrated the system by measuring its response $\varphi_c(x, y)$ to a reference plane wave. The aligned stable system has to be calibrated only once. The intensity I_o and phase φ_o of the object field can be expressed through the measured values of integral intensity of the interferogram $I_r(x, y)$ and phase $\varphi_r(x, y)$, and the phase of the calibration beam $\varphi_c(x, y)$:

$$\begin{aligned} I_o(x, y) &= I_r(x, y) - \min_{x,y}[I_r(x, y)], \\ \varphi_o(x, y) &= \varphi_r(x, y) - \varphi_c(x, y). \end{aligned} \tag{3.1}$$

The lateral resolution $r = 0.61\lambda/NA$ of the system is defined by its numerical aperture, which can be defined as $NA = A/2Z$, where A is the size of the virtual aperture, and Z is the distance between the DMD and the object.

The numerical aperture of the virtual optical system cannot be larger than the angle of diffraction on a single micro-mirror λ/δ, where we assume the micro-mirror size is equal to the pitch δ. With the smallest reported pitch of the DMD of 5.4 μm, and the wavelength varying in the range of $0.4 \backsim 1.5$ μm, we obtain the NA range of 0.075 ∽ 0.27, with larger NA corresponding to a longer wavelength. Similarly, the pixel pitch δ of the DMD determines the smallest spatial frequency detectable: λ/δ. Evidently, the field of view is limited by λ/δ, as any two points separated by a larger angle would cause no interference.

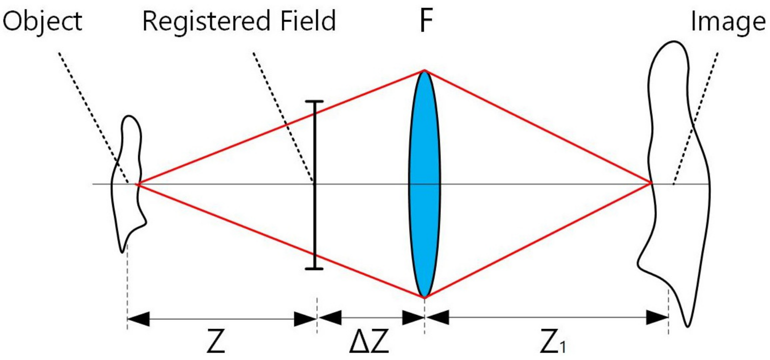

Figure 3.4: Virtual optical system for image reconstruction.

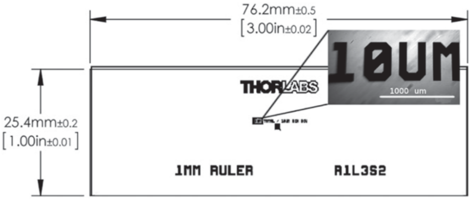

Figure 3.5: The object for imaging experiments: a stage micrometer (R1L3S2P) from Thorlabs.The central line (magnified in the inset) was used for the experiments.

After the complex amplitude $U(x, y) = \sqrt{I_o(x, y)}e^{\varphi_o(x,y)}$ is measured for all points in the pupil, the field distribution in the object plane can be reconstructed by direct back propagation from the plane of the DMD to the object plane, by using, for example, a spectral method:

$$U(x, y, Z) = \Phi^{-1}\left[\Phi[U(x, y, 0)] \cdot e^{-Z\sqrt{k^2-u_x^2-u_y^2}}\right], \tag{3.2}$$

$$U(x, y, 0) = \Phi^{-1}\left[\Phi[U(x, y, Z)] \cdot e^{Z\sqrt{k^2-u_x^2-u_y^2}}\right], \tag{3.3}$$

where Φ and Φ^{-1} are forward and inverse Fourier transforms, Z is the distance from the object to the DMD, u_x and u_y are the coordinated in the Fourier space, and $k = 2\pi/\lambda$, where λ is the wavelength. Direct application of expressions 3.2 reconstructs the field with a magnification of $M = 1$. The magnification can be altered by propagation of the coherent field through a virtual optical system formed by a lens with focal length

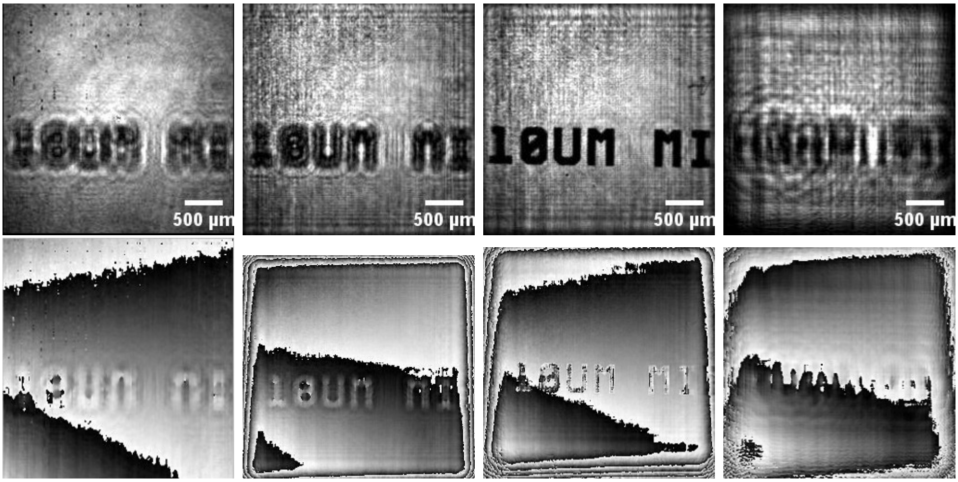

Figure 3.6: Field intensity (top) and phase (bottom) registered in different planes with magnification $M = 1$, and a total field of view of 3x3 mm. From left to right the image shows fields registered at the DMD plane, and back propagated to -2.5 cm, -5.0 cm and -20.0 cm from the DMD.

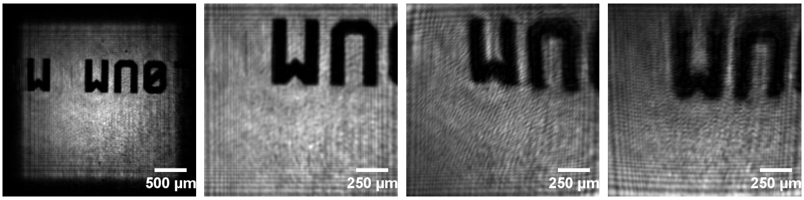

Figure 3.7: Image reconstructed in the best focus plane of a virtual optical system shown in Figure 3.4, with magnification $M = -1$, with magnification $M = -2$, with $M = -2$ and one wave of astigmatism, and with $M = -2$ and one wave of coma (left to right).

F, as shown in Figure 3.4, where

$$M = Z_1/(Z + \Delta Z), \tag{3.4}$$

$$F = \frac{Z_1(Z + \Delta Z)}{Z_1 + Z + \Delta Z}. \tag{3.5}$$

The lens can be modeled as a phase mask $\varphi_l(x, y) = k\frac{x^2+y^2}{F}$. In the simplest case of $M = 1$ and $\Delta Z = 0$, we obtain $Z_1 = Z$, and $F = Z/2$.

Our experimental system, as seen in Figure 3.8, is formed by a 15 *mW* He-Ne laser with a beam expander. The laser illuminates a low-cost DM365 LightCrafter DMD with a pixel pitch of $\delta = 10.8$ μm. The reflected light is collected to the Fourier plane by a 2-inch F/3 lens with a focal length of 15 cm. The interferograms are registered by a low-cost CMOS camera with pixel pitch of 5.5 μm in a region of interest of 512x512 pixels. The DMD is placed at the front focal plane of the lens. The camera is placed at the back focal plane of the lens.

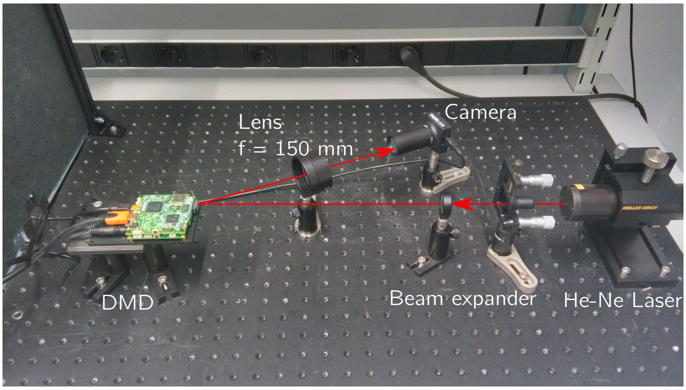

Figure 3.8: The experimental setup of the coherent imaging system.

After registration of the reference phase corresponding to undisturbed laser beam, an object represented by transparent glass slide (see Figure 3.5) with a high-resolution chrome mask was placed in the light path at a distance of $\sim 5\ cm$ from the DMD. The field was registered in a grid of 150x150 pixels, with pixel pitch of $2\delta = 21.6\ \mu m$, forming a virtual square aperture of about 3x3 mm. The numerical aperture of the virtual optical system is equal to $NA = A/2Z = 3/100 \sim 0.03$. The lateral resolution of the optical system is estimated as $r = 0.61\lambda/NA \sim 13\ \mu m$.

Figure 3.6 shows the field distribution registered in the plane of DMD, and reconstructed in three different planes, including the plane of best focus, by using back-propagation described by the pair of expressions (3.2). Figure 3.7 illustrates the result of propagation in a virtual optical system shown in Figure 3.4 with $Z = \Delta Z = 0.05$ m, and magnification of $M = -1$ and $M = -2$. The last two images in Figure 3.7 illustrate the possibility of virtual aberration correction by applying correcting phase terms to the experimentally registered complex field. Since the optical system is practically free from aberration, the addition of aberration terms reduces the image sharpness, but proves the point that virtual adaptive correction is possible in such a system. Such a correction could be necessary, for example, if the object image is registered through the cover glass, causing spherical aberration.

Reconstruction of a complex field with dimensions of NxN requires N^2 interferograms to be registered and processed. Our experimental setup based on inexpensive components achieved registration rates of up to 7 pixels per second, mostly limited by the video interface of the DMD and the camera frame rate. Application of a more advanced DMD and camera would allow to increase the registration rate up to at least 4000 pixels per second, resulting in a time requirement of 15s per frame for a pupil sampling of 256x256 pixels.

3.4. Scanning multiple binary masks

Further acceleration of the previous method can be achieved by increasing the number of active pixels in a frame from two to a larger number. In this section, we present a reference-less and time-multiplexing phase retrieval method by making use of the digital micro-mirror device (DMD). In this method, the DMD functions not only as a flexible binary mask which modulates the optical field, but also as a sampling mask for measuring corresponding phases, which makes the whole setup simple and robust. The DMD reflection forms a sparse intensity mask in the pupil which produces speckle pattern after propagation. With the recorded intensity on the camera and the binary pattern on the DMD, the phase in all the 'on' pixels can be reconstructed at once by solving inverse problems with iterative methods, for instance using Gerchberg-Saxton algorithm. Then the phase of the whole pupil can be reconstructed from a series of binary patterns and speckle patterns. Numerical experiments show the feasibility of this phase retrieval method and the importance of sparse binary masks in the improving of convergence speed.

The basic principle of phase retrieval is explained in Figure 3.9. The surface of DMD is illuminated by coherent laser light. The incident light is aberrated by a transmissive phase object. A DMD and a camera are positioned at the back focal plane and front focal plane of a converging lens respectively. The micro-mirrors of the DMD are randomly switched on to form n frames of binary masks M_i $(i = 1, 2, ..., n)$. With all these masks, the whole DMD plane will be sampled.

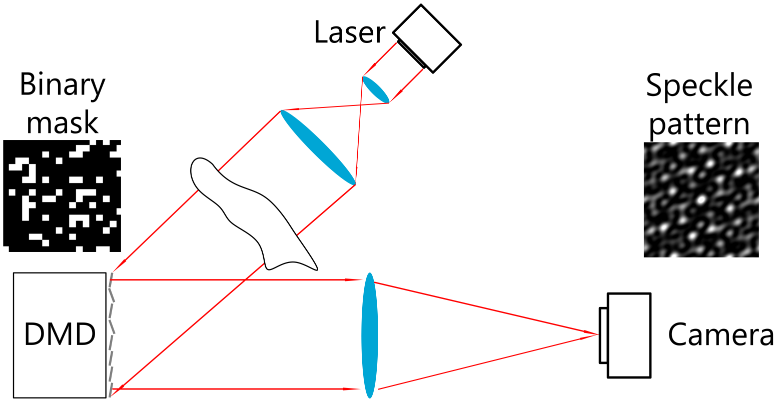

Figure 3.9: Optical set up for phase retrieval based on the DMD generated speckle patterns.

Assuming the optical field at the DMD plane is U_{back}, then we have can describe this relation as:

$$U_{back} = \sum_{i=1}^{n} M_i U_{back}. \tag{3.6}$$

In the wave optics, a converging lens performs two-dimensional Fourier transformations. The optical field in the DMD plane and the field in the camera plane U_{front}

are related by Fresnel propagation:

$$U_{front}(x,y) = \frac{1}{j\lambda F}\hat{U}_{back}(\frac{x}{\lambda F}, \frac{x}{\lambda F}), \tag{3.7}$$

where F is the focal length of the converging lens, λ is the wavelength, $\hat{U}_{back}$ denotes the Fourier transform of U_{back} . When a binary mask M_i is used to modulate intensity at the plane U_{back} , a speckle pattern I^i_{front} propagated from $I^i_{back} = |M_i U_{back}|^2$ can be registered by the camera. This speckle pattern contains the information of the complex field of the DMD plane which can be reconstructed by solving inverse problems.

Iteration methods, for instance the Gerchberg-Saxton (GS) algorithm as introduced in Section 2.6.3 , can be used to reconstruct the optical field. The GS algorithm is based on the iterative calculation of the forward propagation and back propagation. In this case, we modified the classical GS algorithm with the known binary mask and measure speckle patterns as the input information and assuming the initial intensity on the DMD surface is uniformed. The detail modified algorithms is described in Figure 3.10.

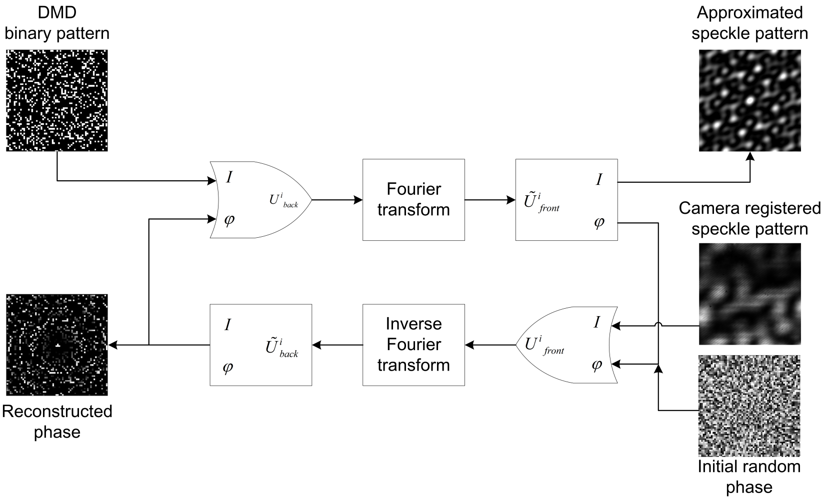

Figure 3.10: Phase retrieval with a modified Gerchberg-Saxton algorithm on a single frame.

We consider that the intensity of the DMD plane is known as the binary pattern M_i . In order to retrieve the phase at the DMD plane, the algorithm starts with the speckle distribution with a random phase at the camera plane. Then the inverse Fourier transform of the field at the front focal plane U^1_{front} is computed, obtaining the optical field at the back focal plane U^i_{back} , with an intensity distribution different from the binary pattern. The phase distribution is conserved, while the intensity distribution is substituted with the known binary pattern. This new field is Fourier transformed, obtaining a pattern $\left|\tilde{U}^i_{front}\right|^2$ at the front focal plane which is similar to the registered speckle pattern. The phase distribution of this pattern is kept, while the intensity is replace with the registered one. Then the inverse Fourier transform is computed again, starting a new iteration cycle. With multiple iterations, the algorithm converges to the exact distribution of the speckle pattern, which contains the right phase of the ‘on’ pixels of DMD.

All the pixels will be randomly switched ‘on’ only once during all the frames. The corresponding phases will be registered and combined together with the help of a shared reference, as shown in Figure 3.11. For instance, a single DMD pixel shared by all frames can be used as a reference to integrate all the phase layers. There is no need of extra setups to create a reference.

Multiple binary patterns are used, as randomness and sparsity in the intensity pattern leads to a quick convergence in the iterative method. Such effects will be investigated in the following numerical experiments.

Based on the setup in Figure 3.9, we built a numerical propagation model to validate the feasibility of this method. In order to investigate the effect of sparsity of given binary patterns, the convergence speed is compared in experiments in different frame numbers (1 frames, 5 frames, 20 frames and 40 frames), see Figure 3.12. The whole dimension of the field is 512x512. The size of DMD is set to be 64x64. A defocus aberration has been applied in the DMD plane.

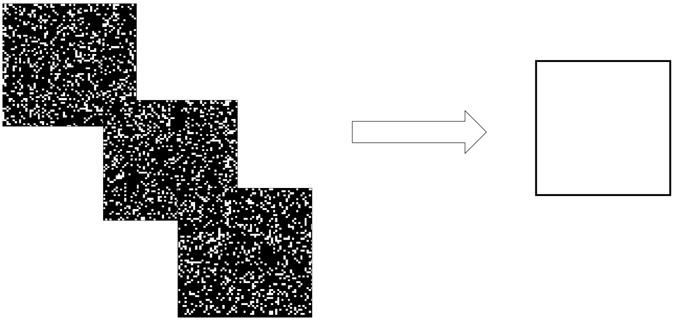

Binary patterns

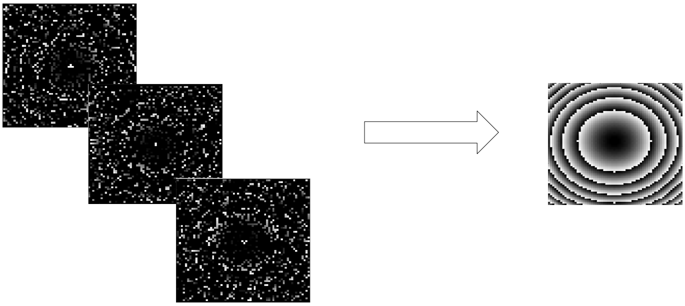

Reconstructed phase

Figure 3.11: The schematic of stacking multiple frames to retrieve the complete phase map.

For a given total number of frames n, there are $4096/n$ micro-mirrors in the ‘on’ state in each frame. We reconstructed the phase for each of the frames using the modified GS algorithm. The variances between the given aberration and the reconstructed phase in each cycle have been calculated for the first 200 iterations.

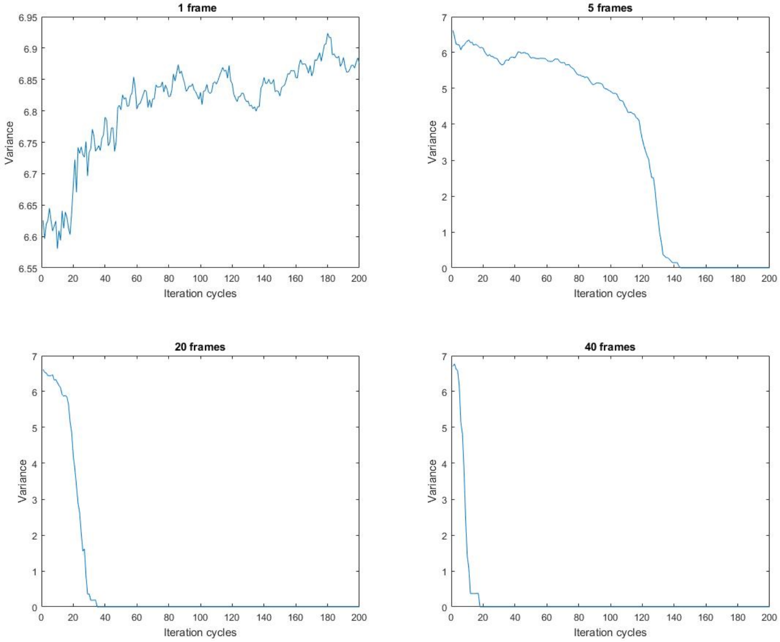

Figure 3.12: Comparison of the converging speed in different number of frames.

The effectiveness of the proposed method depends strongly on the total number of frames. When there is just one frame to reconstruct the whole pupil, which means all the DMD pixels are switched on at once, the GS algorithm cannot converge to a stable result. With a total of 5 frames, the first 200 iterations shown a trend of convergence. Yet the phase was still not close to the true value. The convergence speed increase dramatically with increase of the total number of frame. Less than 40 iteration cycles are needed to converge for $n = 20$, when 5 % of the pixels are turned on. The needed amount of iterations is reduced with the increase of n, and thus the increase of sparsity of the DMD patterns. Though the exact number of iterations is changing with different initial guess, this trend reveals that the condition of sparse sampled input intensity is very important to the success of phase retrieval.

Adapting the parameters in the numerical model to our own experimental setups, we demonstrated the full reconstruction of the phase in DMD pupil formed by 304×342 pixels from only 50 frames. Each of the frame was created with 2 % of the pixels randomly turned on. In the Fourier plane, every frame generated a single intensity pattern, limited to 255 scales of gray, to represent an 8 bit camera image. The center pixel was designated as a reference which was common between all the frames. The simulation yielded the phase reconstruction of an introduced low-order aberration with

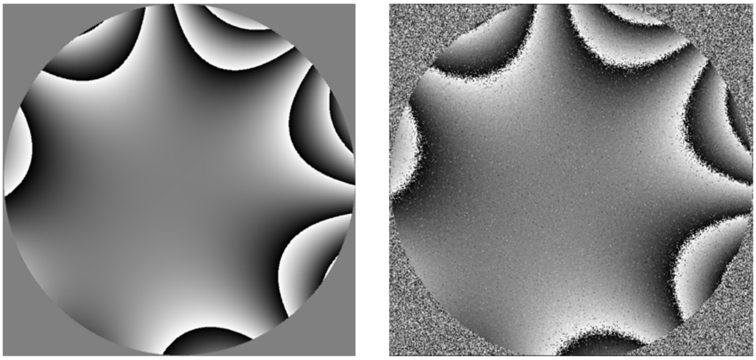

Figure 3.13: Original phase (left, generated by a sum of Zernike polynomial up to the third order) and phase reconstruction from 50 frames.

ten iterations used in the GS algorithm for each frame.

3.5. Conclusions

In the Section 3.3, we have experimentally demonstrated the registration of complex coherent optical field by aperture sampling using a digital micro-mirror device. Unlike other approaches to digital holography, our method does not require any external reference beam, resulting in a very simple and robust registration setup. Based on this approach, a lensless coherent microscope has been realized, in which the complex amplitude has been experimentally registered inside a 3 mm aperture in a grid with 150x150 sampling points. The experimentally registered field have been propagated in a virtual optical system to demonstrate virtual imaging, digital focusing, and adaptive correction.

In the Section 3.4, we demonstrated the feasibility of phase reconstruction by solving phase retrieval problem from multiple speckle patterns produced by binary masks generated with DMD. The quick convergence in iterative method is conditioned by the randomness and sparsity of the intensity carrier in the DMD pupil. Primitive experimental implementations of this method have also been carried out. Due to the noise in the practical conditions, more iterations were required for convergence. The propagation model in the iterative algorithm should consider the misalignment and aberrations of the system as well as the computation time in further work. In addition, the optimal choice of common reference pixels is also expected to make contribution to reduction of the noise.

References

[1] G. Vdovin, H. Gong, O. Soloviev, P. Pozzi, and M. Verhaegen, *Lensless coherent imaging by sampling of the optical field with digital micromirror device,* Journal of Optics **17**, 122001 (2015).

[2] H. Gong, O. Soloviev, D. Wilding, P. Pozzi, M. Verhaegen, and G. Vdovin, *Holographic imaging with a Shack-Hartmann wavefront sensor,* Optics Express **24**, 13729 (2016).

[3] M. K. Kim, *Digital Holographic Microscopy*, Vol. 2011 (2011) pp. 149–190.

[4] I. Yamaguchi, *Phase-Shifting Digital Holography,* Digital Holography and Three-Dimensional Display **22**, 145 (1997).

[5] T. Zhang and I. Yamaguchi, *Three-dimensional microscopy with phase-shifting digital holography,* Optics Letters (1998), 10.1364/ol.23.001221.

[6] N. G. Vlasov, S. G. Kalenkov, D. V. Krilov, and A. E. Shtanko, *Non-lens digital microscopy,* in *Current Research on Image Processing for 3D Information Displays*, Vol. 5821 (International Society for Optics and Photonics, 2005) pp. 158–162.

[7] G. Popescu, L. P. Deflores, J. C. Vaughan, K. Badizadegan, H. Iwai, R. R. Dasari, and M. S. Feld, *Fourier phase microscopy for investigation of biological structures and dynamics.* Optics letters **29**, 2503 (2004).

[8] G. Popescu, T. Ikeda, R. R. Dasari, and M. S. Feld, *Diffraction phase microscopy for quantifying cell structure and dynamics,* Optics Letters **31**, 775 (2006).

[9] B. B. Kemper, A. Vollmer, C. E. Rommel, J. J. Schnekenburger, G. von Bally, and G. von Bally, *Simplified approach for quantitative digital holographic phase contrast imaging of living cells,* Journal of Biomedical Optics **16**, 026014 (2011).

[10] R. W. Gerchberg and W. O. Saxton, *A practical algorithm for the determination of phase from image and diffraction plane pictures,* Optik **35**, 237 (1972).

[11] J. J. Miao, P. Charalambous, J. Kirz, and D. Sayre, *Extending the methodology of X-ray crystallography to allow imaging of micrometre-sized non-crystalline specimens,* Nature **400**, 342 (1999).

[12] S. Witte, V. T. Tenner, D. W. Noom, and K. S. Eikema, *Lensless diffractive imaging with ultra-broadband table-top sources: from infrared to extreme-ultraviolet wavelengths,* Light: Science & Applications **3**, e163 (2014).

[13] B. C. Platt and R. Shack, *History and Principles of Shack-Hartmann Wavefront Sensing,* Journal of Refractive Surgery **17**, 573 (2001).

[14] P. Bon, G. Maucort, B. Wattellier, and S. Monneret, *Quadriwave lateral shearing interferometry for quantitative phase microscopy of living cells.* Optics express **17**, 13080 (2009).

[15] G. Indebetouw, P. Klysubun, T. Kim, and T. C. Poon, *Imaging properties of scanning holographic microscopy.* Journal of the Optical Society of America. A, Optics, image science, and vision **17**, 380 (2000).

[16] E. Y. Lam, X. Zhang, H. Vo, T.-C. Poon, and G. Indebetouw, *Three-dimensional microscopy and sectional image reconstruction using optical scanning holography,* Applied Optics **48**, H113 (2009).

[17] D. Dudley, W. M. Duncan, and J. Slaughter, *Emerging digital micromirror device (DMD) applications,* , 14 (2003).

[18] M. Sheikh and N. A. Riza, *Demonstration of pinhole laser beam profiling using a digital micromirror device,* IEEE Photonics Technology Letters (2009), 10.1109/LPT.2009.2016113.

[19] Y. Gong and S. Zhang, *Ultrafast 3-D shape measurement with an off-the-shelf DLP projector,* Optics Express (2010), 10.1364/oe.18.019743.

[20] D. B. Conkey, A. M. Caravaca-Aguirre, E. Niv, and R. Piestun, *High-speed phase-control of wavefronts with binary amplitude DMD for light control through dynamic turbid media,* Proceedings of SPIE **8617**, 86170I (2013).

[21] R. Schmitt, I. Jakobs, and K. Vielhaber, *Wavefront Sensor Design based on a Micro-Mirror Array for a High Dynamic Range Measurement at a High Lateral Resolution,* in *Fringe 2009: 6th International Workshop on Advanced Optical Metrology*, edited by W. Osten and M. Kujawinska (Springer Berlin Heidelberg, Berlin, Heidelberg, 2009) pp. 1–6.

[22] L. J. Hornbeck, *Digital Light Processing update: status and future applications,* (1999) pp. 158–170.

[23] L. Hornbeck, *Chip Hall of Fame: Texas Instruments Digital Micromirror Device,* (2017).

4

Holographic imaging with a Shack-Hartmann wavefront sensor

A high-resolution Shack-Hartmann wavefront sensor has been used for coherent holographic imaging, by computer reconstruction and propagation of the complex field in a lensless imaging setup. The resolution of the images obtained with the experimental data is in a good agreement with the diffraction theory. Although a proper calibration with a reference beam improves the image quality, the method has a potential for reference-less holographic imaging with spatially coherent monochromatic and narrowband polychromatic sources in microscopy and imaging through turbulence.

Parts of this chapter have been published in Optics Express **24**(13), 13729, 2016 [1].

4.1. Introduction

Recording of the complex electromagnetic field with the method of holography allows to reconstruct both the phase and the amplitude at any propagation point [2, 3]. In general, optical holograms are created by recording the interference patterns created by the object and the reference waves. The object wave field is restored then by scattering the reference beam on the hologram [4].

Methods of digital holography register the wave field in the computer [5], to facilitate the object field reconstruction by computational wave propagation using physical optics models of diffraction and interference [6]. Digital holography has potential advantages of higher speed of the hologram acquisition, simple experimental setups, and most notably, the availability of the complete amplitude and phase information about the optical field. Once the complex amplitude is known, it is possible to manipulate the wavefront to correct aberrations retrospectively [7, 8], extending the methods of adaptive wavefront correction to virtual domain.

Since the phase information is not directly available, different methods of phase reconstruction from intensity measurements have been developed. Phase retrieval and diversity methods have been used to derive the computer description of the optical field [9–11]. These methods reconstruct the complex amplitude by solving an inverse source problem, using numerical methods, such as Gerchberg-Saxton algorithm [8, 12, 13]. In these cases, reconstruction of the complex field from recorded intensities alone represents an ill-posed problem [14].

The Shack-Hartmann (SH) sensor is a simple tool commonly used in adaptive optics to register the arrays of local wavefront tilts [15]. Each subaperture builds a spot-like point-spread function (PSF) image, where the deviation of the centroid of the light spot is proportional to the local wavefront derivative. The wavefront can be efficiently reconstructed from the array of the centroid deviations, in a single shot.

In this chapter we describe experimental realization of holographic image reconstruction from the phase and intensity obtained directly with a high-resolution SH sensor.

4.2. Method

The scheme of a holographic imaging setup based on a SH sensor is shown in Figure 4.1. A transparent object is illuminated by a spatially coherent light beam and the scattered field is registered by a high resolution SH sensor. Registered intensity contains sampled information about the phase gradients and the intensity field, which can be used to reconstruct the complex field in the sensor plane, and to obtain a coherent holographic image of the object by back-propagating the complex field to the object plane. Though the method is applied to a transparent object, a similar setup could be used for imaging of reflective and scattering objects.

For a SH sensor having full aperture of A and pitch p, the resolution of the sensor can be estimated from the analysis of interference produced by two coherent point sources S_1, S_2 belonging to the object plane. If the distance between these two sources

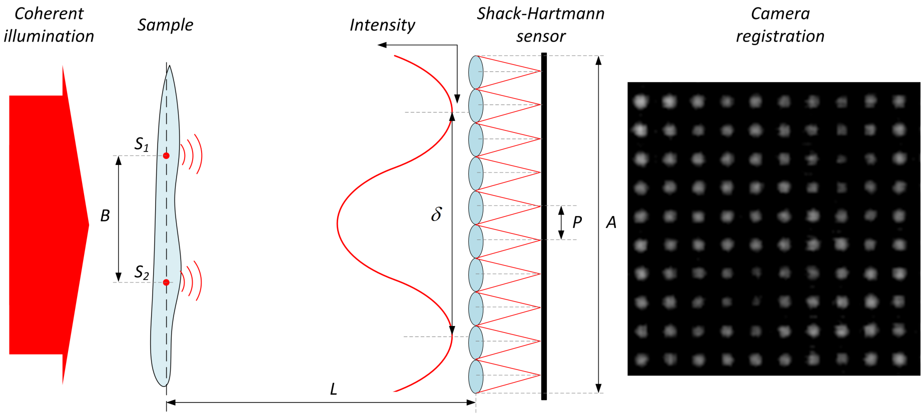

Figure 4.1: Imaging holographic setup based on the SH sensor.

is equal to B, then the interference fringe period δ in the sensor plane, at a distance L from the object, is given by:

$$\delta = \frac{\lambda L}{B}. \tag{4.1}$$

To avoid any information loss, the fringe period should be smaller than the sensor aperture: $\delta < A$. From this condition, we can derive the expression for minimum distance between two point sources that is still resolved by the sensor:

$$B_{min} = \frac{\lambda L}{A}, \tag{4.2}$$

where object features smaller than B_{min} will not be resolved by the sensor.

On the other hand, from the Nyquist criterion, the minimum fringe period in the sensor plane should cover at least 2 micro-lenses: $\delta = 2p$, from which we can derive the expression for the maximum field of view in the object plane:

$$B_{max} = \frac{\lambda L}{2p}. \tag{4.3}$$

Condition (4.3) has a simple physical meaning: the whole object should be small enough to remain unresolved by a single lenslet. This condition defines the difference between our method and the approaches described in [16, 17], where each subaperture resolves the object. If the object is larger than B_{max}, the reconstructed field will have parasitic low-frequency modulation, caused by aliasing. In some cases, when the low frequency modulation is not important, the field of view can be chosen larger than that defined by the condition (4.3).

The total number of resolved elements, in the ideal aliasing-free case, is given by:

$$\frac{B_{max}}{B_{min}} = A/2p. \tag{4.4}$$

The number of resolved elements is one half of the number of micro-lenses along the chosen coordinate, and the total number of pixels resolved in the object plane is one quarter of the number of micro-lenses in the sensor matrix.

Reconstruction of the complex optical field from a high-resolution SH pattern requires several steps. The phase is obtained by integrating the wavefront gradients [18]. Since the number of resolved elements in the hologram is proportional to the number of lenslets, large lenslet arrays should be used for high-resolution imaging. Special methods of phase reconstruction, suitable for processing of large arrays of spot images produced by a SH sensor have been developed in Refs. [19–21]. In these methods, the SH intensity pattern is represented as a composition of a series of interference fringes. The pattern is Fourier transformed, then the first side lobes along the frequency axes f_x and f_y in the Fourier domain are moved to the origin. Then, the phase derivatives ϕ_x and ϕ_y are obtained as the argument of the inverse Fourier transform of the shifted distribution of intensity. Then, the gradients W_x and W_y can be derived as:

$$W_x = p\phi_x/(2\pi F), \;\; W_y = p\phi_y/(2\pi F), \tag{4.5}$$

where F is the focal length of the micro-lens array.

Once the gradient information has been obtained, the wavefront can be reconstructed by a Fourier-based modal reconstruction [22–24].

$$\hat{W}(f_x, f_y) = -i\frac{(f_x\hat{W}_x + f_y\hat{W}_y)}{2\pi(f_x^2 + f_y^2)}. \tag{4.6}$$

Here the Fourier series is seen as a set of basis function of the wavefront. $\hat{W}$ is used to denote the angular spectrum of W. In the work of [25] it was shown that replacement of f by $2\sin(f/2)$ in equation (4.6) gives a better noise performance. We have tried both reconstructors, but found no noticeable difference.

Before the Fourier based wavefront reconstruction can take place, it is essential to pre-process the gradient fields. The ϕ_x, ϕ_y derived from the arguments of exponential functions range in $[0, 2\pi]$, possessing numerous discontinuities. Depending on the method, phase unwrapping [26] might be required to obtain a smooth phase function that can be used for building the physical optics model of propagation.

The intensity field can be obtained by smoothing the spot pattern with a suitable low-frequency filter. The final complex field in the sensor plane is obtained by combining the phase and intensity fields. Finally, the object amplitude and phase distributions are reconstructed by back propagation of the complex field to the object plane.

4.3. Simulation

For the numerical simulation we have adopted the parameters of the experimental setup, described in Section 4.4, shown in Figure 4.1: a collimated beam with the wavelength of $\lambda = 633$ nm is scattered by positive transparent resolution test chart, shown in Figure 4.2. To represent the complex field, we used a square array with sampling dimensions of $n \times n = 2048 \times 2048$ pixels with pixel pitch $\mu = 5.5$ μm. After passing through the sample, the wave is propagated to the SH sensor at a distance of $L = 0.5$ m. The SH array is formed by $N \times N = 140 \times 140$ micro-lenses in orthogonal geometry with a pitch of $p = 63\ \mu$m. The focal length of each micro-lens is 2 mm, and the total size of the array is $A = 8.82$ mm. According to equation (4.2) the resolution of our setup in the object plane is equal to:

$$B_{min} = \frac{\lambda L}{A} = 35\ \mu\text{m} \tag{4.7}$$

and the total field-of-view $B_{max} = B_{min} N/2 = 2.45$ mm.

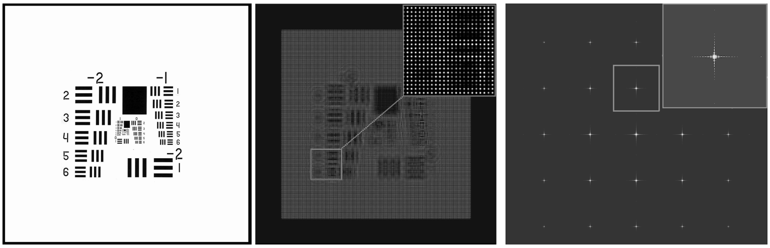

Figure 4.2: Numerical model: resolution test chart (left). Intensity pattern retrieved from the SH sensor at a distance of 0.5 m from the chart (middle). The central part of the Fourier transform of the intensity pattern with sidelobes (inset) used to reconstruct the x and y components of local WF tilts (right).

The simulation was initiated with filtering the coherent light wavefield through the intensity mask. Then the filtered wave was propagated to the SH sensor, filtered through the phase mask corresponding to the SH array, and propagated to the image plane, where the intensity distribution was registered by a simulated camera with linear intensity response with pixel pitch of $\mu = 5.5\ \mu$m. The simulated intensity pattern $I_0(x, y)$, registered by the SH sensor, is shown in the middle of Figure 4.2.

The right part of Figure 4.2 shows the result of discrete Fourier transform (DFT) of the registered SH sensor intensity pattern $I_0(x, y)$. The four symmetrical sidelobes at distance $d = \mu N/p \approx 179$ pixels from the center contain the phase information. The scale of the DFT image is defined by the zero padding of the input array. The sidelobes have been extracted in the window of 140×140 pixels, corresponding to the number of lenslets N, and translated to the origin. The wavefront gradients were obtained by applying inverse DFT to the centered sidelobe.

Figure 4.3 shows the wrapped distributions ϕ_x and ϕ_y. Two-dimensional Goldstein branch cut unwrapping algorithm [26, 27] was used to unwrap the gradient fields. The wavefront $W(x, y)$, reconstructed using equations (4.5, 4.6) is shown in the right part of Figure 4.3. As expected, the wavefront has low-amplitude high-frequency modulation, with some large phase jumps localized in the areas of low intensity, where the phase reconstruction is ill-defined.

The SH pattern $I_0(x, y, L)$ was smoothed by a Gaussian filter to obtain the intensity field $\tilde{I}_0(x, y, L)$, shown in Figure 4.4. The complex field registered in the SH sensor

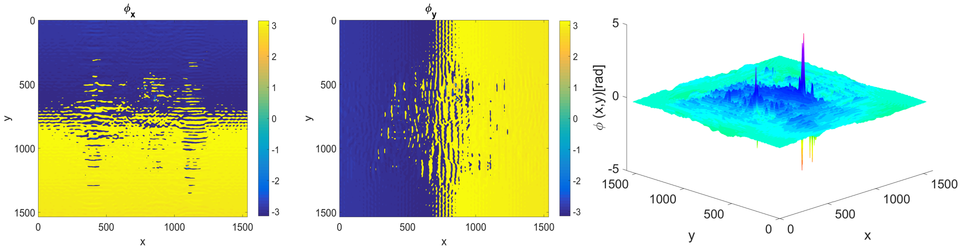

Figure 4.3: Gradients ϕ_x, ϕ_y, corresponding to the diffraction on USAF test chart, reconstructed from the inverse Fourier transform (left, middle), and the wavefront reconstruction (right).

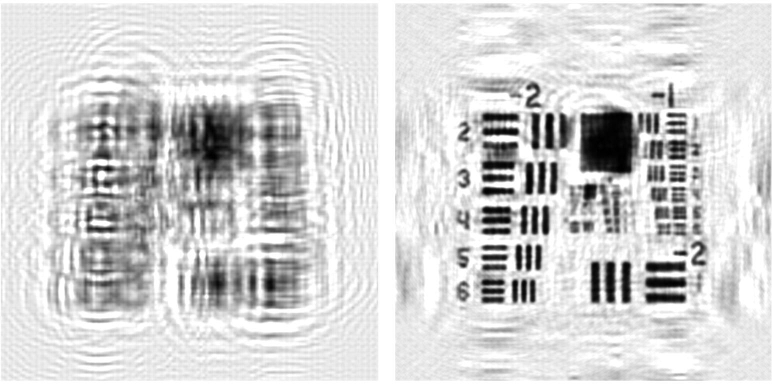

Figure 4.4: Sensor intensity obtained in simulation, by filtering the SH pattern (left), and the reconstruction of the resolution test chart by back propagation of the reconstructed complex field to the object plane (right).

plane was composed as $U(x,y,L) = \sqrt{\tilde{I}_0(x,y,L)}\exp(i\theta(x,y,L))$, where $\theta(x,y,L) = kW(x,y,L)$ and $k = 2\pi/\lambda$. The complex field in the resolution test chart plane $U(x,y,0)$ can be reconstructed by back propagation:

$$U(x,y,0) = \mathcal{F}^{-1}\{e^{-iL\sqrt{k^2-f_x^2-f_y^2}}\mathcal{F}(U(x,y,L))\}. \tag{4.8}$$

Figure 4.4 shows the filtered intensity in the sensor plane and the numerical reconstructed image of the resolution test chart in the object plane, at a distance of $L = -0.5$ m. The resolution of the image corresponds to the theoretical limit. The results of numerical experiment clearly demonstrate the validity of the method.

As with any other SH sensor, the reconstruction is expected to be not very sensitive to the degree of temporal coherence in the illumination. We have simulated the hologram reconstruction obtained with broadband sources composed of three monochromatic lines with the bandwidth $\Delta\lambda = 20$ nm, formed by three lines at $\lambda_1 = 623$, $\lambda_2 = 633$, $\lambda_3 = 643$ nm; $\Delta\lambda = 50$ nm, formed by three lines at $\lambda_1 = 598$, $\lambda_2 = 633$, $\lambda_3 = 658$ nm; and $\Delta\lambda = 200$ nm, formed by three lines at

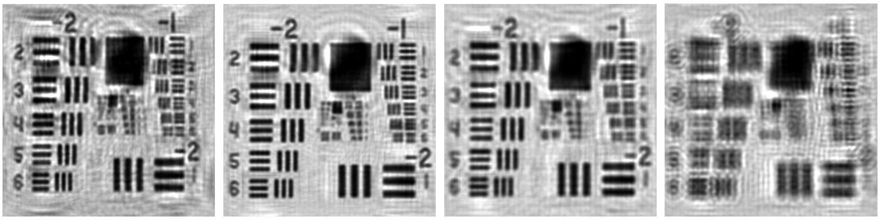

Figure 4.5: Simulated image reconstruction obtained with spatially coherent 633 nm monochromatic source (left) and polychromatic sources with bandwidth of 20, 50 and 200 nm, centred at 633 nm (images 2 to 4, counted from left to right).

$\lambda_1 = 533$, $\lambda_2 = 633$, $\lambda_3 = 733$ nm. For each polychromatic source, we simulated the SH spot pattern by incoherent summation of three intensity patterns obtained for three wavelengths $I_{\sum} = I_{\lambda_1} + I_{\lambda_2} + I_{\lambda_3}$. The resulting polychromatic spot pattern $I_{\sum}$ has been used to coherently reconstruct the wavefront and the object, using the central wavelength of $\lambda_2 = 633$ nm. The reconstruction results, shown in Figure 4.5, demonstrate robust reconstruction for source bandwidth of up to 50 nm (up to 200 nm with significant resolution loss), proving the method conditional usability with polychromatic spatially coherent sources.

4.4. Experiment

For experimental validation we have built a setup according to the scheme shown in Figure 4.1, with all parameters matching the simulation described in the previous section. Positive USAF 1951 test target (R1DS1P, Thorlabs, U.S), shown in Figure 4.6 was used as the test object. The object was placed at a $L = -0.5$ m distance in front of the SH mask. The SH array (OKO Tech, the Netherlands) is formed by $N \times N = 140 \times 140$ micro-lenses in orthogonal geometry with a pitch of $p = 63$ μm, focal length of $F = 2$ mm and the total size of the square array of $A = 8.82$ mm. High resolution camera UI-3370 (IDS corporation, Germany) has been used for image registration.

In order to eliminate the systematic aberrations, the reference wavefront has been registered without the object. In principle, this step can be excluded, but then some virtual adaptive optics needs to be used for the compensation of systematic system aberrations. Calibration with the reference beam is a simple step, which needs to be done only once, then the calibration data can be used as long as the illumination beam is stable.

After filtering and correction for the reference phase, we retrieved the intensity and phase distributions in the plane of SH sensor. Figure 4.6 illustrates the intensity corresponding to the object field, registered by the SH sensor. The image of the resolution test target, obtained by back propagation to the distance of $L = -0.5$ m, is shown in Figure 4.7.

Robust reconstruction of the wavefront is possible only when spots from all subapertures are present in the image registered by the SH sensor. Theoretically, the high

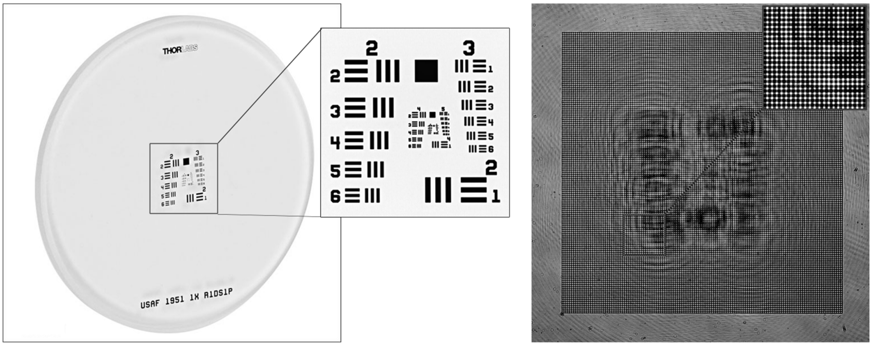

Figure 4.6: Positive 1951 USAF test target (R1DS1P, Thorlabs, U.S) (left), and the image registered by the SH sensor (right).

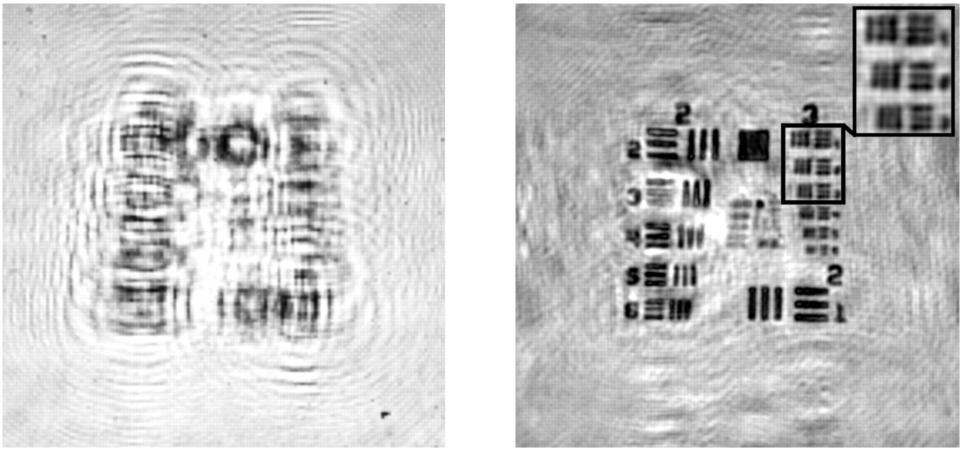

;

Figure 4.7: Filtered experimentally registered intensity (left), and object reconstruction, obtained by back propagation of the reconstructed wave to -0.5 m (right).

harmonics of the scattered light should enter all subapertures, even those in the geometrical shadow. However, registration of these harmonics requires a large dynamic range and high signal to noise ratio of the image sensor. In our experiment, with standard USAF 1951 resolution chart, we have resolved the second element in the third group. The resolution is defined by a standard formula $R = 2^{G+(E/6)} \approx 8.95$ lp/mm, where $G = 3$ and $E = 2$ are the group and element numbers. This corresponds to the resolved line pitch of 56 μm, which is close to the theoretical limit of 35 μm. We attribute the resolution loss to the measurement noise, limited dynamic range of the camera, and aliasing caused by the too large object size. Also, the resolution of the method can not be reported exactly, due to some ambiguity in the definition of coherent resolution, caused by the intrinsic nonlinearity of coherent imaging. See Ref. [28] for further discussion on the definition of coherent resolution.

4.5. Discussion and Conclusion

We have demonstrated holographic imaging with a SH sensor, experimentally realizing a transmissive lensless imaging setup with close to the diffraction limited resolution on a high-contrast object.

This technique holds promise for microscopy and general coherent imaging with extended depth of field in applications that require fast registration and fast processing of a large number of relatively low-resolution holograms, such as dynamic holographic interferometry, flow cytometry, dynamic microscopic imaging. In addition, direct reconstruction of the complex field allows to create a virtual adaptive optical system, computationally correcting for the aberrations in the imaging path. This approach can be used for coherent multi-aperture imaging of remote objects through atmospheric turbulence, in systems similar to suggested in [17, 29].

The experimental setup can be further optimized for speed and simplicity. In particular, the number of camera pixels used for hologram registration, can be optimized. In our setup we used more than 100 pixels to register the light spot under each single lenslet. Essentially, a quad cell with 4 pixels is sufficient for the registration of both the intensity and the centre of gravity of the light spot. This brings us to the minimum requirement to the number of pixels in the registration camera: 4 imaging sensor pixels are needed per micro-lens, and 4 micro-lenses are needed per reconstructed hologram pixel, resulting in the minimum requirement of 16 camera pixels per reconstructed pixel in the final image. This conclusion sets theoretical limit to the number of pixels, in the assumption of linear response of the quad cell to the spot coordinate. In practice, a system with large number of quad cells is expected to be non-linear and difficult to align, but nonetheless a quad-cell based Hartmann sensor proved possible in the previous work from the authors [30]. Coherent back propagation extends the information contents beyond the single intensity distribution, by using the phase to reconstruct the intensity in a number of different planes along the propagation path.

There is no principal requirement for a reference beam, though the quality of reconstruction is better when the reference beam is used to account for systematic aberrations. To achieve the theoretical resolution, the imaging setup requires the incoming light to have a high degree of spatial coherence over the whole lenslet array. However, simulation proves that the instrument is not very sensitive to the degree of temporal coherence in the illumination and can be used with spatially coherent polychromatic sources.

In this chapter, we have investigated the bare-bone proof of concept. It can be further developed for a higher resolution and higher numerical aperture by using denser and larger micro-lens arrays, and by introducing additional optics for proper optical coupling of the illumination beam to the object and the sensor, towards usable coherent imaging instrument.

References

[1] H. Gong, O. Soloviev, D. Wilding, P. Pozzi, M. Verhaegen, and G. Vdovin, *Holographic imaging with a Shack-Hartmann wavefront sensor,* Optics Express **24**, 13729 (2016).

[2] D. Gabor, *A New Microscopic Principle,* Nature **161**, 777 (1948).

[3] M. K. Kim, *Digital Holographic Microscopy,* Digital Holographic Microscopy Principles, Techniques, and Applications **2011**, 149 (2011).

[4] U. Schnars, C. Falldorf, J. Watson, and W. Jüptner, *Digital Holography and Wavefront Sensing: Principles, Techniques and Applications* (Springer, 2015) pp. 1–226.

[5] J. W. Goodman and R. W. Lawrence, *Digital image formation from electronically detected holograms,* Applied Physics Letters (1967), 10.1063/1.1755043.

[6] J. W. Goodman, *Introduction to Fourier Optics*, 2nd ed. (Roberts and Company Publishers, 2005) p. 491.

[7] P. Ferraro, S. De Nicola, A. Finizio, G. Coppola, S. Grilli, C. Magro, and G. Pierattini, *Compensation of the inherent wave front curvature in digital holographic coherent microscopy for quantitative phase-contrast imaging,* Applied Optics **42**, 1938 (2003).

[8] G. Vdovin, H. Gong, O. Soloviev, P. Pozzi, and M. Verhaegen, *Lensless coherent imaging by sampling of the optical field with digital micromirror device,* Journal of Optics **17**, 122001 (2015).

[9] J. R. Fienup, *Phase retrieval algorithms: a comparison,* Applied Optics **21**, 2758 (1982).

[10] R. A. Gonsalves, *Phase retrieval and diversity in adaptive optics,* Optical Engineering **21**, 829 (1982).

[11] Y. Shechtman, Y. C. Eldar, O. Cohen, H. N. Chapman, J. Miao, and M. Segev, *Phase Retrieval with Application to Optical Imaging,* Signal Processing Magazine , 1 (2014), arXiv:1402.7350 .

[12] R. W. Gerchberg and W. O. Saxton, *A practical algorithm for the determination of phase from image and diffraction plane pictures,* Optik **35**, 237 (1972).

[13] F. Meng, D. Zhang, X. Wu, and H. Liu, *A comparison of iterative algorithms and a mixed approach for in-line X-ray phase retrieval,* Optics Communications **282**, 3392 (2009), arXiv:NIHMS150003 .

[14] C. Guo, C. Wei, J. Tan, K. Chen, S. Liu, Q. Wu, and Z. Liu, *A review of iterative phase retrieval for measurement and encryption,* Optics and Lasers in Engineering , 1 (2016).

[15] B. C. Platt and R. Shack, *History and Principles of Shack-Hartmann Wavefront Sensing,* Journal of Refractive Surgery **17**, 573 (2001).

[16] S. A. Alexandrov, T. R. Hillman, T. Gutzler, and D. D. Sampson, *Synthetic aperture fourier holographic optical microscopy,* Physical Review Letters (2006), 10.1103/PhysRevLett.97.168102.

[17] J. Holloway, M. S. Asif, M. K. Sharma, N. Matsuda, R. Horstmeyer, O. Cossairt, and A. Veeraraghavan, *Toward long-distance subdiffraction imaging using coherent camera arrays,* IEEE Transactions on Computational Imaging (2016), 10.1109/tci.2016.2557067.

[18] W. Southwell, *Wave-front estimation from wave-front slope measurements,* Journal of the Optical Society of America **70**, 998 (1980).

[19] Y. Carmon and E. N. Ribak, *Phase retrieval by demodulation of a Hartmann-Shack sensor,* Optics Communications **215**, 285 (2003).

[20] A. Talmi and E. N. Ribak, *Direct demodulation of Hartmann-Shack patterns.* Journal of the Optical Society of America. A, Optics, image science, and vision **21**, 632 (2004).

[21] C. Canovas and E. N. Ribak, *Comparison of Hartmann analysis methods,* Applied Optics **46**, 1830 (2007).

[22] K. R. Freischlad and C. L. Koliopoulos, *Modal estimation of a wave front from difference measurements using the discrete Fourier transform,* Journal of the Optical Society of America A **3**, 1852 (1986).

[23] F. Roddier and C. Roddier, *Wavefront reconstruction using iterative Fourier transforms.* Applied optics **30**, 1325 (1991).

[24] G. M. Dai, *Wavefront optics for vision correction*, February (SPIE Press, 2008) p. 366.

[25] A. Talmi and E. N. Ribak, *Wavefront reconstruction from its gradients,* Journal of the Optical Society of America A **23**, 288 (2006).

[26] D. C. Ghiglia and M. D. Pritt, *J Investig Dermatol* (1998).

[27] R. M. Goldstein, H. A. Zebker, and C. L. Werner, *Satellite radar interferometry: Two-dimensional phase unwrapping,* Radio Science (1988), 10.1029/RS023i004p00713.

[28] R. Horstmeyer, R. Heintzmann, G. Popescu, L. Waller, and C. Yang, *Standardizing the resolution claims for coherent microscopy,* Nature Photonics **10**, 68 (2016).

[29] M. Loktev, O. Soloviev, S. Savenko, and G. Vdovin, *Speckle imaging through turbulent atmosphere based on adaptable pupil segmentation,* Optics letters **36**, 2656 (2011).

[30] D. W. De Lima Monteiro, G. Vdovin, and P. M. Sarro, *High-speed wavefront sensor compatible with standard CMOS technology,* Sensors and Actuators, A: Physical **109**, 220 (2004).

5

Optical path difference microscopy with a Shack-Hartmann wavefront sensor

In this chapter we show that a Shack-Hartmann wavefront sensor can be used for quantitative measurement of the specimen optical path difference in an ordinary incoherent optical microscope, if the spatial coherence of the illumination light in the plane of the specimen is larger than the microscope resolution. To satisfy this condition, the illumination numerical aperture should be smaller than the numerical aperture of the imaging lens. This principle has been successfully applied to build a high-resolution reference-free instrument for the characterization of the optical path difference of micro-optical components and microscopic biological samples in both transmissive and reflective configurations.

Parts of this chapter have been published in Optics Letters **42**(11), 2122, 2017 [1] and Proc. SPIE 10616, 2017 International Conference on Optical Instruments and Technology: Optical Systems and Modern Optoelectronic Instruments [2].

5.1. Introduction

Optical path difference (OPD) is an important modality in modern microscopy, as it provides additional information about the structure of microscopic samples, especially when the intensity modulation is weak due to low absorption in the specimen. In many cases, such as characterization of micro-optical components, it is important to measure the quantitative distribution of the sample OPD, with a precision comparable to ordinary optical shop testing.

Phase contrast microscopy visualizes the OPD of microscopy samples and different techniques can be used to achieve this phase contrast. Zernike phase contrast microscopy increases the image contrast by manipulating the phase difference between the scattered and unscattered light [3, 4]. However, this intensity information cannot be converted to OPD directly, moreover, images are affected by an inherent halo and shade-off artifacts. Differential interference contrast microscopy is a kind of shearing interferometry which generates the phase gradient contrast by slightly shifting two polarized light beams and then interfering them with each other [5]. This method is more popular than Zernike phase contrast for its good pseudo three-dimensional view and improvement on the transverse resolution, although it can not be employed to quantitative OPD measurements due to its non-linear response.

Interferometric methods, such as interference microscopy and digital holographic microscopy, provide quantitative phase measurements with high transverse resolution [6], but they require a highly coherent light source. On the other hand, White-light interferometry usually requires an accurate positioning stage to achieve quantitative measurements [7]. In addition, the practical applicability of these interferometric methods is limited by the requirements of a highly coherent reference beam [8, 9].

Phase diversity methods [10, 11] retrieve the phase by iteratively solving inverse problems using well-established diffraction theory. Mostly they suffer from slow convergence and non-uniqueness in the result due to the ill-posed nature of the problem. Redundant constraints, such as intensity measurements at different distances [12], with diverse phases [13] and with varying apertures [14, 15], can be used to improve phase retrieval performance. The additional apparatus required by these methods further complicates the imaging system.

Wavefront sensing technology is widely and maturely developed in the field of adaptive optics [16]. Quadriwave lateral shearing interferometry wavefront sensor has been employed for quantitative phase imaging and has achieved a sensitivity of a few nanometers [17]. Recently, a technique named partioned aperture wavefront sensing also realized quantitative phase measurement with incoherent illumination by using a quatrefoil lens [18].

Shack-Hartmann (SH) wavefront sensors are widely used to detect the smooth wavefronts of the light beam. Such a restriction to low-order reconstruction is sufficient for many applications, thus the transverse resolution of SH sensors was inferior to the interferometric and phase retrieval sensors [19]. However, the development of high-resolution SH sensors facilitates their direct application to imaging problems, for example a holographic imaging with a SH sensor has been recently demonstrated: [20].

In this chapter, we report a quantitative OPD microscope based on a high resolution SH wavefront sensors. By directly using wavefront reconstruction technique, the OPD due to the sample thickness and refractive index can be simply obtained by integration of the gradient field registered by the sensor. This non-interferometric technique is able to work under spatial incoherent illumination with high light efficiency. As a widely available optical component, the SH wavefront sensor can easily transform an ordinary microscope into an OPD imaging modality with the following described principles. Two configurations both in transmissive and reflective modes were implemented and tested.

5.2. Transmissive configuration

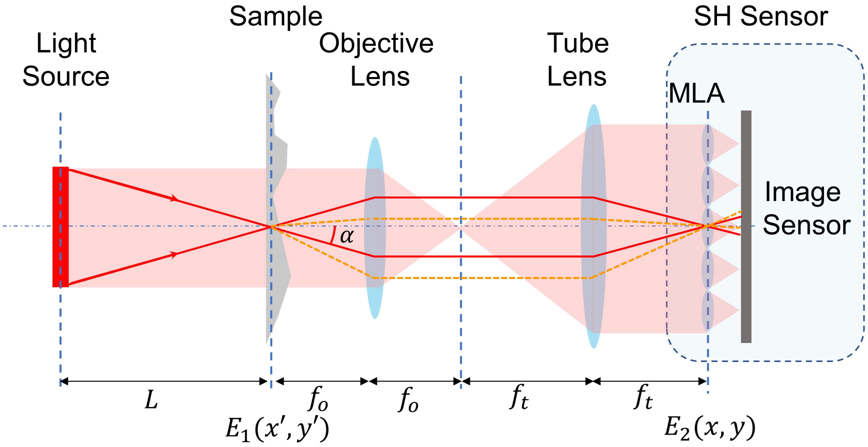

Figure 5.1: Diagram of the Shack-Hartmann quantitative OPD microscope.

The scheme of a transmissive SH-based OPD microscope is shown in Figure 5.1. To correctly understand its function, we need to consider two optical paths: (1) The imaging is performed by projecting the sample image on the microlens array (MLA), by the optical system formed by the objective lens and the tube lens with magnification $M = f_t/f_o$ where f_t and f_o are the focal lengths of the tube and objective lens respectively. In this optical path, each lenslet corresponds to a single pixel in the image of the sample intensity. (2) The wavefront sensing path is formed by the light source, a transparent sample with unknown OPD distribution, the objective lens, the tube lens, and the MLA. The first image of the light source is formed in the pupil of the objective lens if $L \gg f_o$, which is easy considering the short focal length of microscope objectives. The position of this image depends on the wavefront tilts introduced by the sample. The pupil plane, containing an image of the source, is conjugated to the image sensor by the system formed by the tube lens and one of the lenslets. Since each lenslet corresponds to a single resolution point in the sample plane, the lateral shift of the source image behind the lenslet will be dependent on the local wavefront tilt introduced in the corresponding point of the sample.

5.2.1. Principles

To obtain a correct SH pattern with localized light spots, the position of which is linearly dependent on the OPD gradients, two physical conditions should be satisfied:

(1) To guarantee that the scattered light has enough space to move in the pupil of objective, the half angular size of the light cone α scattered by the sample, should be smaller than the aperture angle of the objective:

$$\tan(\alpha) \ll A_o. \tag{5.1}$$

(2) To guarantee the correct centroiding, the image of light source behind the lenslet should be smaller than the MLA pitch:

$$\tan(\alpha/M) \ll A_M, \tag{5.2}$$

where A_M is the numerical aperture of the micro-lens array.

With the assumption that the sample has a minor effect on the scattered light cone, the angle α is mainly defined by the numerical aperture of the illumination A_s. According to Van Cittert-Zernike theorem, the coherence size provided by an extended source with numerical aperture of A_s in the plane of sample is proportional to $\sim \lambda/A_s$, while the resolution of the microscope is defined by the numerical aperture of imaging lens $\sim \lambda/A_o$. This brings us to the conclusion that, to secure correct operation of a SH sensor, the length of spatial coherence of the illumination light in the sample plane should be larger than the optical resolution of the microscope. In the plane of the MLA, full spatial resolution is obtained with lenslets that are smaller than the microscope point spread funtcion (PSF). This condition is equivalent to the requirement of complete spatial coherence over the extent of a single lenslet. If the lenslet size is larger than the PSF size, correct wavefront reconstruction is still possible, with some loss of spatial resolution, as long as condition 5.2 is satisfied.

Compared to the usual wavefront sensing requirement of complete coherence over the whole aperture of the sensor, these requirements are much softer. This difference is explained by the fact, that the OPD function is a deterministic function which is coherent by definition, therefore only local coherence of the probe light is needed to characterize it. In contrast, the wavefront characterization in the field of adaptive optics, the deterministic function describing the wavefront can be defined only if the light is coherent over the whole sensor aperture, including all lenslets.

In the MLA plane, the wavefront gradient decreases by a factor of M due to the microscope magnification, while the wavefront height remains the same. The registered SH pattern can be approximated as a regular foci grid modulated by the wavefront gradients $\frac{\partial W}{\partial x}$, $\frac{\partial W}{\partial y}$ under the assumption that the spots are circularly symmetric and equal. The wavefront gradients may be retrieved from the first harmonics as follows

[21, 22]:

$$I_{SH}(x,y) = E_2(x,y)E_2^*(x,y)\left\{2 + \cos\left[\frac{2\pi}{P}\left(x + F\frac{\partial W}{\partial x}\right)\right] + \cos\left[\frac{2\pi}{P}\left(y + F\frac{\partial W}{\partial y}\right)\right]\right\}, \tag{5.3}$$

where F is the focal length of a lenslet. P is the pitch of MLA. Therefore, the illumination source should also meet the same requirement as the assumption for SH spots. When considering the absorption of the sample, the movement of spots is not affected by small intensity variations. While if the absorption is severe, the SH pattern should be carefully exposed or enhanced with high dynamic range techniques.

In this chapter we retrieve the wavefront gradients by using the Fourier demodulation method [23]. A reference wavefront is registered in advance in the absence of sample, for sensor calibration. Then the OPD gradients brought by the sample $\frac{\partial O(x,y)}{\partial x}, \frac{\partial O(x,y)}{\partial y}$ can be obtained by calculating the deviation from the reference. Finally, we can reconstruct the OPD by two-dimensional gradient integration [24]:

$$O(x,y) = \mathcal{F}^{-1}\left\{-i\frac{f_x\mathcal{F}\left\{\frac{\partial O(x,y)}{\partial x}\right\} + f_y\mathcal{F}\left\{\frac{\partial O(x,y)}{\partial y}\right\}}{{f_x}^2 + {f_y}^2}\right\}. \tag{5.4}$$

Here $\mathcal{F}\{\cdot\}$ and $\mathcal{F}^{-1}\{\cdot\}$ denote the Fourier transform and inverse Fourier transform. f_x, f_y are the coordinates in the frequency domain. Note that phase unwrapping is needed when the obtained wavefront gradients contain phase jumps [25].

5.2.2. Experiments

To study the feasibility and accuracy of this method, the OPD profile of a micro-lens array (APO-Q-P300-R8.6, AMUS GmbH, Germany) was measured in the experiment with a customized microscope in the configuration of Figure 5.1. The light source is a collimated LED (M470L3-C1, Thorlabs, US) with the central wavelength of 460 nm, and a bandwidth of 25 nm. The numerical aperture of this collimated LED source is $A_s \approx 0.02$. A commercial SH sensor (FS3370-O-P63-F2, OKO Tech, the Netherlands) consisting of 140×140 lenslets with a pitch of $P = 63\ \mu m$, focal length of $F = 2\ mm$, with a 2048×2048 digital CMOS sensor employed for image registration. Our setup is built to satisfy the condition:

$$P \leqslant M\frac{\lambda}{A_o}, \tag{5.5}$$

which is equivalent to condition 5.2. According to condition 5.5, the microscope was then implemented with a 10× microscope objective ($A_o = 0.25$) and a tube lens with $f_t = 400\ mm$, providing $\sim 2.5\times$ extra magnification, resulting in a total magnification of 25×. With a 63 μm lenslet, here we have experienced some loss in the spatial resolution, but the OPD was correctly reconstructed since condition 5.2

was still satisfied.

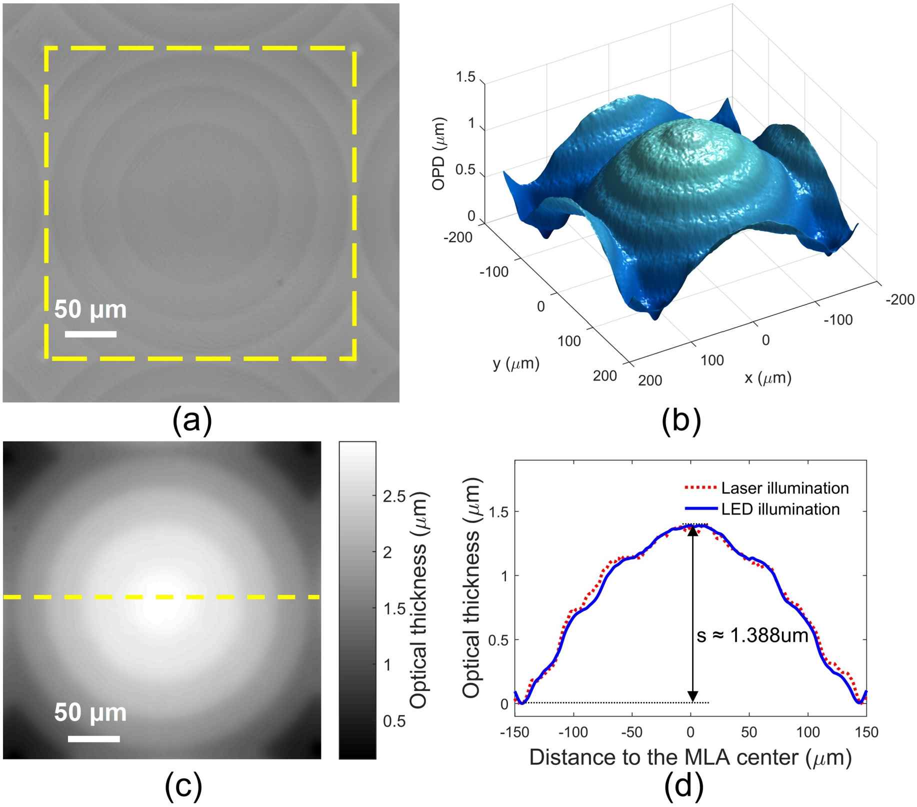

(a) (b) (c) (d)

Figure 5.2: Bright field microscope of a lenslet obtained with 10× microscope objective with $A_o = 0.25$ (a). 3D OPD map of the MLA reconstructed from a SH sensor with a LED illumination (b). Thickness map of the lenslet (c). Center cross-section of the micro-lens reconstructed with LED and laser illumination (d).

The experimental results are shown in Figure 5.2. According to the manufacturer specification sheet, the sample lenslets have plano-convex spherical shape with a pitch of 300 μm and a nominal focal length of 18.6 mm. The sagitta of micro-lens is $s = 1.31$ μm. The contrast of the bright field image in Figure 5.2 (a) is very poor even though some ring structures are visible. Figure 5.2 (b) shows the three-dimensional reconstruction of the OPD in the specimen. The layer structure due to lithographic fabrication process is clearly visible. The refractive index of the central wavelength in the fused silica is $n = 1.4647$. Then the OPD map of a single micro-lens is converted to the optical thickness in Figure 5.2 (c). The blue line in Figure 5.2 (d) is the center line cross-section of the micro-lens thickness map. The measured sagitta $s = 1.388$ μm is close to the given geometric parameter. The red dash line is the measurement of the same micro-lens in the same setup, but with the LED replaced by a collimated fiber laser (HLS635, Thorlabs, US). The wavelength of the laser is 635 nm and the refractive index is then $n = 1.4570$. We can see a very good agreement between these two measurements. The variance may be due to the speckle noise, as it tends to produce a more noisy measurements compared to partially coherent light. The spatial resolution in this particular case is limited to $r_s = P/M \approx 2.5\ \mu$m. In the assumption of noiseless registration, the OPD error per lenslet can be derived from the average wavefront curvature over the lenslet $\Delta_M \approx {r_s}^2 |\overline{\frac{d^2\psi}{dr^2}}|$, where ψ is the OPD function and r is the coordinate. For a spherical surface with radius R we have $|\overline{\frac{d^2\psi}{dr^2}}| = 1/R$. In this particular case with $R = 18.6\ mm$, $\Delta_M \approx 0.34$ nm. Further analysis of the OPD error due to reconstruction noise, speckle, sensor sensitivity and other factors, is out of scope of this work. The data of our reconstruction, including thickness and number of layers, and the amplitude of the surface waviness, is in perfect agreement with the manufacturer's data, obtained independently for this particular sample (V. Leleko, private communication).

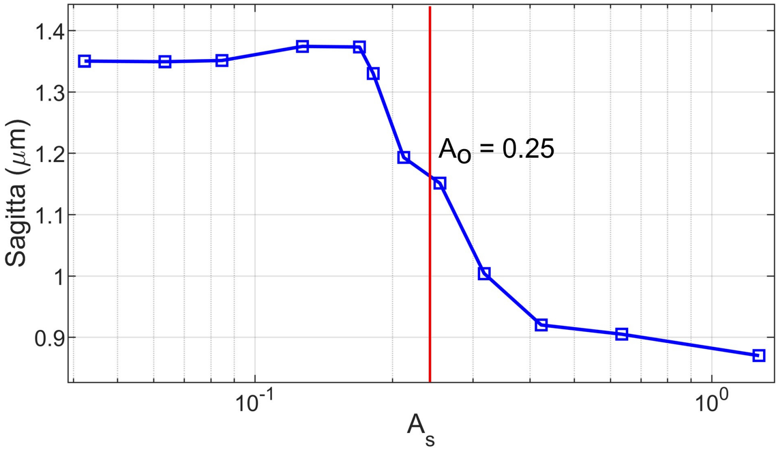

Figure 5.3: Measured thickness of micro-lens sagitta versus numerical aperture of illumination A_s.

In Figure 5.3, we investigated the influence of the illumination coherence on the accuracy of the OPD measurement. The incoherent LED illumination was scattered by a ground glass with a diameter of $D = 25.4\ mm$ at a distance L from the sample. We controlled the source angular size $A_s = D/2L$ by changing the distance L between the ground glass and the sample. The experiment produces correct reconstruction as long as the illumination size $A_s \leqslant 0.17$. Further increase of A_s causes the measurement error to rise quickly, when A_s is approaching A_o, in agreement with our analysis. The increase of the illumination NA results in larger bright source image inside the dark objective lens pupil. Wavefront tilts are sensed as movements of this bright image in the dark field. When the source image becomes too large, wavefront tilts result in vignetting of the shifted image by the edges of the pupil, producing erroneous measurements. Finally, when the image is larger than the pupil, the sensitivity to movements is reduced to zero. In this configuration, condition 5.2 is always satisfied, therefore, some strongly scattered ray movements were still sensed. Thus, we have shown experimentally, that a SH sensor can be used for precision measurements of OPD profiles with relatively low coherent illumination. Conventional microscopes could be easily converted for OPD imaging by properly adjusting the numerical aperture of the illumination system.

We have further applied this microscope to biological samples. An unstained dry red blood cell (RBC) smear was observed under a 40× objective (NA = 0.65). Figure 5.4 is the bright field image of red blood cells. In this image, only the outline of the red blood cells is visible. Details of the content of the red blood cells are however invisible due to the transparency of the red blood cells.

The OPD map, shown in Figure 5.4 (c) offers more topographic information of the red blood cells, e.g. the ring shape of blood cells. Thus, this method offers interesting potentials for blood related disease diagnostics. Particular interesting application could be clear imaging of the malaria parasite in an unstained infected blood sample.

Figure 5.5 shows both the bright field image and OPD map of a living human cheek cell. The sample was surrounded by physiological saline and was sandwiched between microscope slide and cover slip. The biological structure of the cheek cell including the nucleus, cytoplasm and membrane ruffles are visible in the OPD map while it is difficult to resolve from the bright field image without labeling. Benefiting from the high photon efficiency by using MLA to gather light, the SH image of the cell was acquired at an exposure time less than 5 ms with 1/6 of the LED maximum current (about 50 mW). The acquisition speed can easily achieve the full frame rate (75 fps) of the sensor, which enables real-time cell and sub-cell activity monitoring.

5.2.3. Conclusion

In summary, we have shown that for instrumental application of a SH sensor to characterize the OPD of transparent samples in an imaging microscope, the lateral coherent length of the illumination should be larger than the resolution of the imaging lens of the microscope. Additionally, the numerical aperture of the illumination source should be smaller than the numerical aperture of the imaging lens. This condition allows one to optimize the microscope both for high-resolution imaging and for correct OPD sensing. Based on these principles, we have developed a simple and robust quantitative OPD imaging microscope with which we have accurately characterized the OPD profile of microscopic samples, including micro-optical components, unstained blood cells and unstained cheek cells. This method can be easily applied to a conventional microscope, through proper alignment of the illumination setup, providing a low cost methodology for quantitative OPD analysis. Although only transmissive imaging cases has been verified in these experiments, this technique holds potential for reflective surface profile imaging, which is described in the following section.

5.3. Reflective configuration

In this section, we present a quantitative phase imaging microscope based on a SH sensor, that directly reconstructs the optical path difference (OPD) in a reflective mode.

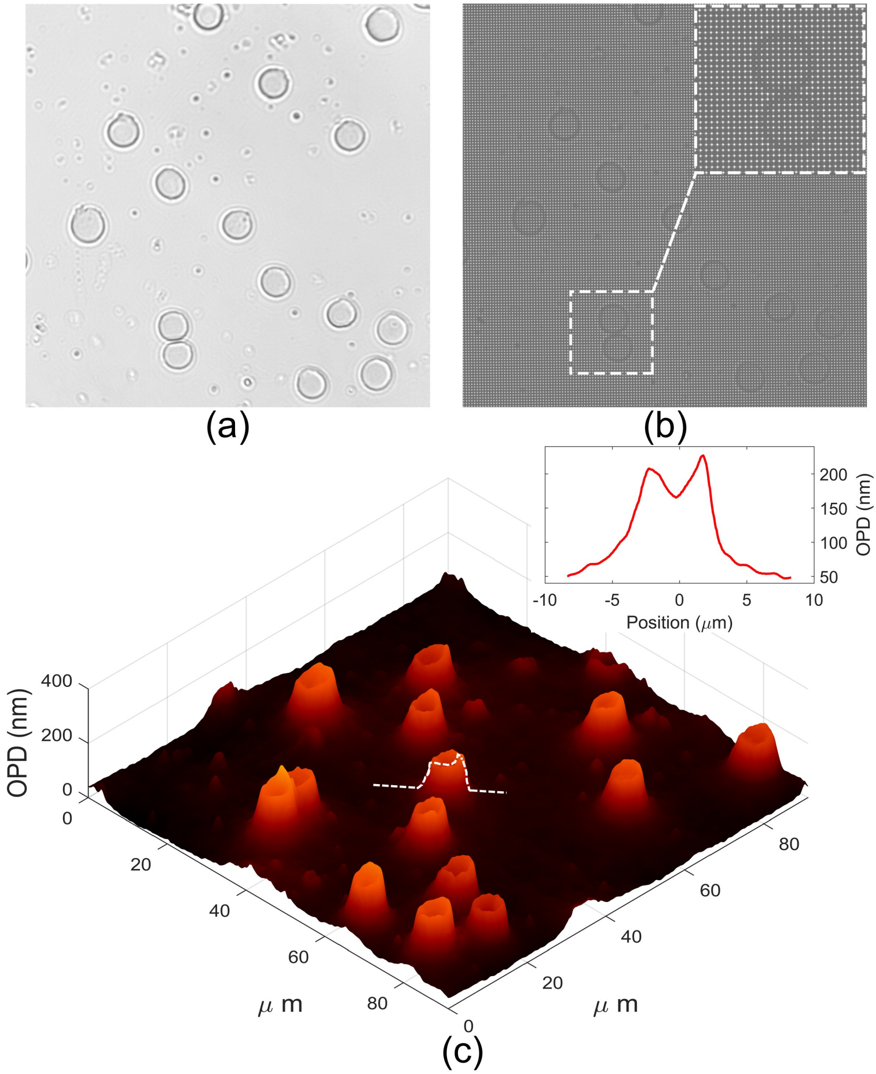

Figure 5.4: (a) Bright field image of red blood cells; (b) SH pattern; (c) the reconstructed OPD map. A cross-sessions of the OPD of individual blood cell is shown in the inset.

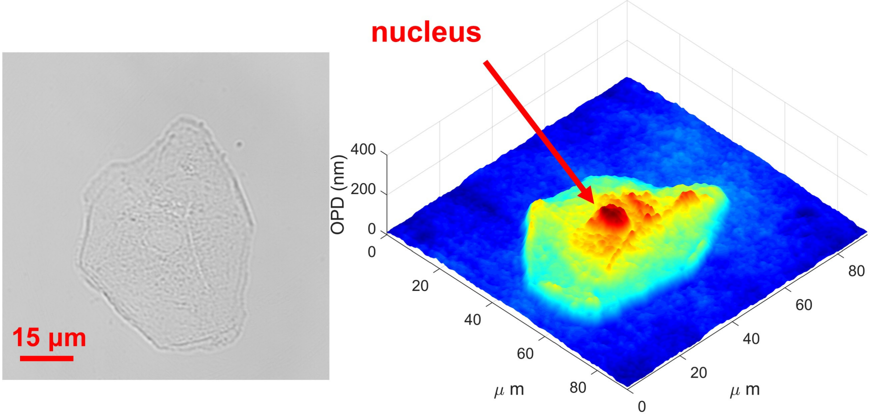

Figure 5.5: OPD measurement of a living cheek cell: (left) the bright field intensity image; (right) the OPD map.

Compared with the holographic or interferometric methods, the SH technique needs no reference beam in the setup, which simplifies the system greatly. With a pre-registered reference, the OPD image can also be reconstructed from a single shot. Also, the method has a rather relaxed requirement on the illumination coherence, thus a cheap light source such as a LED is feasible in the setup. In the previous section, we have successfully verified that a conventional transmissive microscope can be transformed into an optical path difference microscope by using a SH wavefront sensor under incoherent illumination. The key condition is that the numerical aperture of illumination should be smaller than the numerical aperture of imaging lens. This approach is also applicable to characterization of reflective and slightly scattering surfaces.

Characterization of the profile of a surface is required in various applications in both industrial and biomedical fields, including MEMS characterization, precision micro-optics, living cell monitoring [26–28]. The existing profiling methods can be put into two categories: contact and non-contact. Generally, the contact methods use a stylus to scan the surface to achieve resolution in nanometer or sub-nanometer scale. The mechanical system is bulky and the scanning process is relatively slow, especially for a 2D areas. Because of the invasive tip, certain materials, such as biological samples, are difficult to measure.

Therefore, the non-contact optical methods are gaining popularity in profilometry. Currently, the interferometric methods, such as the scanning interferometry and digital holography, are dominant. In general, they exploit the interference between the reference and sample beams. The phase difference between the two beams is extracted from the recorded interferogram or hologram. These methods can measure the surface topography with lateral resolution down to the diffraction limit. The axial resolution can achieve a sub-nanometer range. However, aberrations are difficult to avoid through all the optical components in the setup. Building a highly sensitive interferometric system needs a very good alignment which takes a lot of effort to achieve in practice. Most interferometric methods rely on highly coherent light source, which will suffer from speckle noise not only the measured sample but also the scattering of optical components [9, 29]. Both the requirements on system alignment and light source add the cost to a commercial instrument. Applying the wavefront sensing technique to the profilometry is also a trend. Methods like the partitioned aperture wavefront sensing [30], and the quadriwave lateral shearing interferometry [17] obtain good results.

In this work, we investigate further the reflective profilometry with the Shack-Hartmann wavefront sensor. We consider the requirements to illumination coherence and image sampling. Then the Fourier demodulation wavefront reconstruction technique is described. An experimental setup has been built to validate the feasibility of the method. A hexagonal microlens array mold is characterized using the method. The experimental results indicate that it is promising to instrumentalize this technique due to its simple and robust feature.

5.3.1. Illumination conditions

If the sample image is obtained on the surface of the microlens array, the spot size in the subaperture of a SH sensor is defined by the spatial coherence of the illumination beam and the scattering in the sample. Similar to the requirement in the transmissive configuration 5.2.1, the spot should fit into the field of view, also have some freedom to move, to facilitate precise measurements of local tilts. Here we can summarize the rule for reflective configuration into the expression:

$$\frac{\lambda}{C} + S + 2T \ll A, \tag{5.6}$$

where C is the characteristic size of the spatial coherence of illumination in the plane of the sample, S is the scattering angle on the sample, T is the maximum expected tip/tilt of the sample surface, and A is the numerical aperture of the imaging lens. Condition (5.6) allows for engineering compromise between the spatial coherence C of the illumination, sample scattering S, and the measurement range T, especially if A is not large enough.

5.3.2. Experiments

Figure 4.1 depicts an implementation of the SHWFS based microscope in a reflection configuration which is suitable for micro surface profiling. This implementation can be easily modified from a standard reflective microscope. A converging lens is used before the objective lens to collimate the light incident on the sample. The SHWFS locates at the imaging plane after the tube lens which is conjugated with the focal plane of objective lens with a system magnification. The objective lens, tube lens and the types of SHWFS can be tuned to satisfy the illumination condition in Section 5.3.1 with respect to the desired applications.

The difference from the transmission configuration is that the retrieved gradients are twice the OPD gradients. It is because of the reflected angle is doubled the local

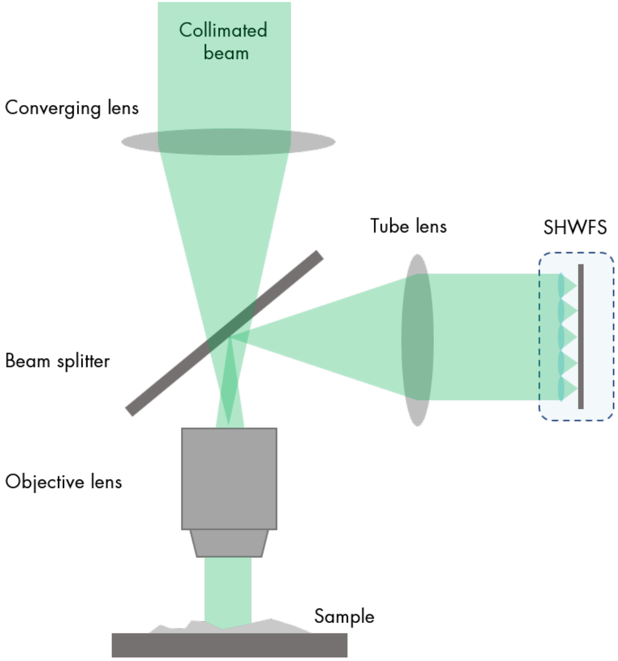

Figure 5.6: Setup of a SHWFS based reflective micro-profilometer.

tilt with respect to the normal of surface. This factor should be eliminated before the OPD reconstruction.

An off-spec silicon mold, provided by Flexible Optical BV, see Figure 5.7, is characterized to verify the feasibility of the approach. The mold has been fabricated by anisotropic etching of silicon [31, 32]. This hexagonal array has 127 micro-mirrors with a pitch of $p = 300$ μm, radius of curvature $r \approx 9.52$ mm and sag $s \approx 1.18$ μm.

The schematic of our experiment is shown in Figure 5.6. A collimated green LED (central wavelength 530nm, M530L3, Thorlabs, US) is used as the light source. A positive lens with focal length of 200 mm, in combination with a 10× objective (NA = 0.25) is used to form collimated sample illumination. The imaging/sensing arm is formed by the objective and a $f = 400$ mm tube lens, providing total magnification of 25×). The mold images are projected onto the microlens array of the SH sensor, to form a sharp image. The SHWFS (FS3370-O-P63-F2, Flexible Optical BV, Netherlands) has 140×140 lenslets in orthogonal arrangement. The pitch of the lenslet array is 63 μm. The focal length of each lenslet is about 2 mm. The sampling interval in the measurement plane is equal to $63/25 \approx 2.5\mu$m.

A reference is obtained with a flat mirror in the sample plane. This calibration step only has to be carried out just once. Then, the mold was put at the focal plane with a SH pattern being recorded. The reconstructed OPD is shown in Figure 5.8 (a). We can clearly identify the hexagon structure and the surface shape from the reconstruction.

A profile of the center is shown in Figure 5.8 (b) after a tilt correction. We flip this measurement upside down to compare with the ideal surfaces of the expected microlens in Figure 5.8 (c). The mirror figure defect, due to non-uniform etching rate, is clearly visible in the measurement result.

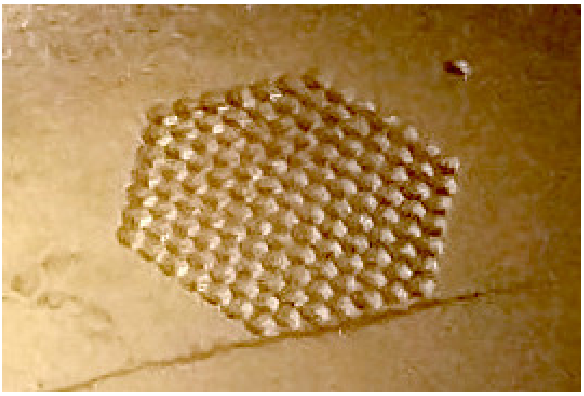

Figure 5.7: Silicon mold of a hexagonal microlens array, with pitch of 300μm.

5.3.3. Discussion and Conclusion

We have experimentally shown that the SH sensor can be used for micro-profilometry in a very simple setup, with relaxed requirements to the coherence of illumination and the sample scattering. The throughout investigation of the accuracy, range, and the sensitivity of the method, will be carried out in the future. In this particular experiment, we used this micro-profilometer to characterize the quality of a microfabricated silicon mold and have demonstrated a quite promising performance.

Moreover, there are some considerations when applying this approach as a micro-profilometer:

- The system can tolerate a certain amount of scattering on the sample, however significant roughness and scattering of the surface make contributions to the left part of condition (5.6), resulting in bad signal-to-noise performance and the failure of measurements.
- Instead of measuring the height directly, it is the OPD gradients being measured. The optical system works as a low pass filter for the gradients, so any reflected ray at an angle which is larger than the system NA (*i.e.* the high frequency components in angular spectrum) will be ignored, causing black spot in the image. Steep surfaces are difficult to detect with this method. A high numerical aperture system or multiple angle detection is needed to improve the performance.
- For samples with non-uniform reflection/absorption the high dynamic range (HDR) technique can be considered to extend the intensity dynamic range. Be-

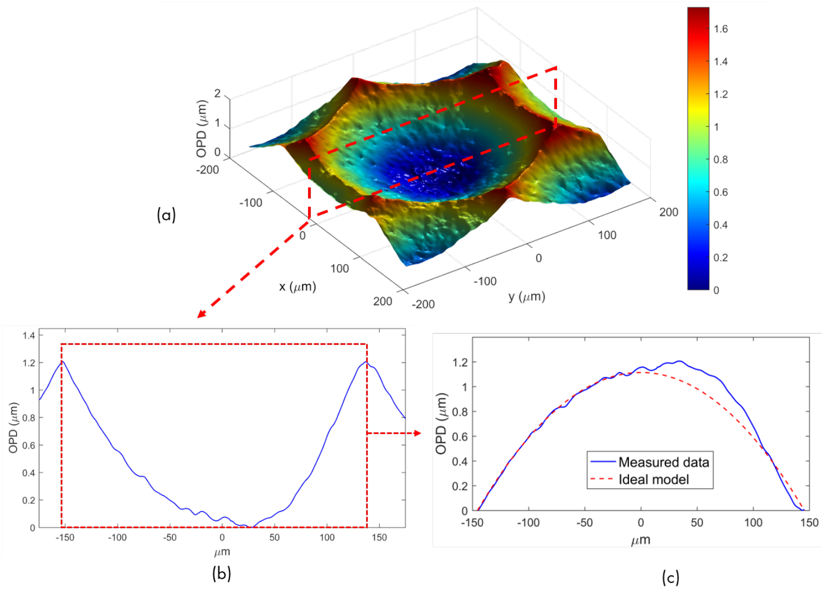

Figure 5.8: Reconstruction of the profile of a single 300 μm micro-mirror: the reconstructed OPD map (a), the cross-section profile of the micro-mirror (b), and the comparison between the measured and prescription profile data (c).

side that, the non-uniform intensity also affects the wavefront reconstruction [33] and needs to be investigated further.

We have successfully demonstrated a micro-profilometer based on reflective Shack-Hartmann wavefront sensing technique. The technique can be implemented by simply modifying a standard reflection microscope. It can work with a low cost light source under relaxed requirements to the spatial and temporal coherence, making it an inexpensive alternative to the existing techniques.

References

[1] H. Gong, T. E. Agbana, P. Pozzi, O. Soloviev, M. Verhaegen, and G. Vdovin, *Optical path difference microscopy with a Shack–Hartmann wavefront sensor,* Optics Letters **42**, 2122 (2017).

[2] H. Gong, O. Soloviev, G. Vdovin, and M. Verhaegen, *Shack-Hartmann reflective micro profilometer,* 2017 International Conference on Optical Instruments and Technology: Optical Systems and Modern Optoelectronic Instruments , 68 (2018).

[3] F. Zernike, *Phase contrast, a new method for the microscopic observation of transparent objects part II,* Physica **9**, 974 (1942).

[4] D. Murphy, *Fundamentals of light microscopy and Electronic Imaging* (2001).

[5] H. Gundlach, *Phase contrast and differential interference contrast instrumentation and applications in cell, developmental, and marine biology,* Opt. Eng. **32**, 3223 (1993).

[6] M. K. Kim, *Digital Holographic Microscopy,* Digital Holographic Microscopy Principles, Techniques, and Applications **2011**, 149 (2011).

[7] J. C. Wyant, *White light interferometry,* Proceedings of the SPIE - The International Society for Optical Engineering **4737**, 98 (2002).

[8] P. Ferraro, S. De Nicola, A. Finizio, G. Coppola, S. Grilli, C. Magro, and G. Pierattini, *Compensation of the inherent wave front curvature in digital holographic coherent microscopy for quantitative phase-contrast imaging,* Applied Optics **42**, 1938 (2003).

[9] B. Kemper and G. von Bally, *Digital holographic microscopy for live cell applications and technical inspection,* Applied Optics **47**, A52 (2008).

[10] R. A. Gonsalves, *Phase retrieval and diversity in adaptive optics,* Optical Engineering **21**, 829 (1982).

[11] Y. Shechtman, Y. C. Eldar, O. Cohen, H. N. Chapman, J. Miao, and M. Segev, *Phase Retrieval with Application to Optical Imaging: A contemporary overview,* IEEE Signal Processing Magazine **32**, 87 (2015), arXiv:1402.7350 .

[12] C. Guo, C. Wei, J. Tan, K. Chen, S. Liu, Q. Wu, and Z. Liu, *A review of iterative phase retrieval for measurement and encryption,* Optics and Lasers in Engineering , 1 (2016).

[13] P. Gao, G. Pedrini, C. Zuo, and W. Osten, *Phase retrieval using spatially modulated illumination.* Optics letters **39**, 3615 (2014).

[14] H. Gong, P. Pozzi, O. Soloviev, M. Verhaegen, and G. Vdovin, *Phase retrieval from multiple binary masks generated speckle patterns,* (SPIE Press, 2016) p. 98992N.

[15] H. Lu, J. Chung, X. Ou, and C. Yang, *Quantitative phase imaging and complex field reconstruction by pupil modulation differential phase contrast,* Optics Express **24**, 25345 (2016).

[16] R. K. Tyson, *Principles of Adaptive Optics*, Vol. 18 (2015) p. 360.

[17] P. Bon, G. Maucort, B. Wattellier, and S. Monneret, *Quadriwave lateral shearing interferometry for quantitative phase microscopy of living cells.* Optics express **17**, 13080 (2009).

[18] A. B. Parthasarathy, K. K. Chu, T. N. Ford, and J. Mertz, *Quantitative phase imaging using a partitioned detection aperture,* Optics Letters **37**, 4062 (2012).

[19] J.-C. Chanteloup, *Multiple-wave lateral shearing interferometry for wave-front sensing.* Applied optics **44**, 1559 (2005).

[20] H. Gong, O. Soloviev, D. Wilding, P. Pozzi, M. Verhaegen, and G. Vdovin, *Holographic imaging with a Shack-Hartmann wavefront sensor,* Optics Express **24**, 13729 (2016).

[21] Y. Carmon and E. N. Ribak, *Phase retrieval by demodulation of a Hartmann-Shack sensor,* Optics Communications **215**, 285 (2003).

[22] C. Canovas and E. N. Ribak, *Comparison of Hartmann analysis methods,* Applied Optics **46**, 1830 (2007).

[23] A. Talmi and E. N. Ribak, *Direct demodulation of Hartmann-Shack patterns.* Journal of the Optical Society of America. A, Optics, image science, and vision **21**, 632 (2004).

[24] A. Talmi and E. N. Ribak, *Wavefront reconstruction from its gradients,* Journal of the Optical Society of America A **23**, 288 (2006).

[25] M. A. Herráez, D. R. Burton, M. J. Lalor, and M. A. Gdeisat, *Fast two-dimensional phase-unwrapping algorithm based on sorting by reliability following a noncontinuous path,* Applied Optics **41**, 7437 (2002).

[26] G. Berkovic and E. Shafir, *Optical methods for distance and displacement measurements,* Advances in Optics and Photonics **4**, 441 (2012).

[27] R. Leach, *Optical Measurement of Surface Topography*, Vol. 53 (Springer, 2011) p. 320.

[28] A. Weckenmann, *Manufacturing and measurement of freeform optics,* CIRP Annals - Manufacturing Technology **62**, 823 (2013).

[29] C. D. Depeursinge, A. M. Marian, F. Montfort, T. Colomb, F. Charrière, J. Kühn, E. Cuche, Y. Emery, and P. Marquet, *Digital Holographic Microscopy (DHM) applied to Optical Metrology: A resolution enhanced imaging technology applied to inspection of microscopic devices with subwavelength resolution,* Fringe 2005 , 308.

[30] R. Barankov and J. Mertz, *Single-exposure surface profilometry using partitioned aperture wavefront imaging.* Optics letters **38**, 3961 (2013).

[31] D. W. de Lima Monteiro, O. Akhzar-Mehr, P. M. Sarro, and G. Vdovin, *Single-mask microfabrication of aspherical optics using KOH anisotropic etching of Si.* Optics express **11**, 2244 (2003).

[32] G. V. Vdovin, O. Akhzar-Mehr, P. M. Sarro, D. W. DeLimaMonteiro, and M. Lokteva, *Arrays of spherical micromirrors and molded microlenses fabricated with bulk {Si} micromachining,* Proc. of SPIE **4945**, 11 (2003).

[33] X.-j. Chen, L.-z. Dong, S. Wang, P. Yang, and B. Xu, *Algorithms to eliminate the influence of non-uniform intensity distributions on wavefront reconstruction by quadri-wave lateral shearing interferometers,* Optics Communications **402**, 276 (2017).

6

Light-sheet fluorescence microscope with waveguide illumination

> *Ideas do not always come in a flash*
> *but by diligent trial-and-error experiments*
> *that take time and thought.*
>
> **Charles Kuen Kao**

Although a large body of research has been done on light-sheet formation through a multimode fibre, we found out that simple adaptive control does not secure a stable light-sheet with a standard multimode waveguide. Any small deformation of the waveguide distorts the mode combination, destroying the target intensity distribution. In our opinion, the approach is implementable, but not practical. Therefore, in this chapter we have concentrated on the methods to obtain the full functionality of a light-sheet formation via the multimode waveguide, that allows for high stability and simple implementation. In this respect, we have investigated two approaches: 1. Slab multimode waveguide with light-sheet translation and control using the Talbot effect; 2. Multimode waveguide formed by a plurality of GRIN lenses.

6.1. Introduction of light-sheet fluorescence microscope

During the last decades, fluorescence microscopy has become a powerful biological and medical imaging tool for the biologists. The fluorophores, which are able to conjugate with many biological molecules in the specimen, can be excited by a specific wavelength, and emit light with a longer wavelength. This emission captured by the fluorescence microscope allows high resolution and high contrast imaging of the fluorophore distribution, hereby indicating the structure of the specimen. Many fluorescence microscopy techniques have been developed according to different applications [1, 2]. The epi-fluorescence microscope, as shown in Figure 6.1 (a), is one of the most popular implementations. Its illumination part and detection part are arranged on the same side of the sample stage. Both the illumination and emission light travel through the same objective lens in this configuration. It is able to capture a wide field of view of the sample at a time. Thus, it is suitable for fast acquisition of dynamic processes while suffering a relatively low axial resolution and the signal will be affected by the background fluorescence from the out-of-focus layers [3].

Confocal fluorescence microscope, as shown in Figure 6.1 (b), filters out the out-of-focus light by placing a spatial pinhole or a pinhole array at the confocal plane with the sample before the detector. It increases the signal-to-noise ratio and contrast. As a consequence, the lateral resolution is improved compared to wide-field fluorescent microscopy [4]. Combining with the techniques of illumination engineering, such as stimulated emission depletion microscopy (STED) [5], structured illumination microscopy(SIM) [6], and localization algorithms, such as photoactivated localization microscopy(PAM) , and stochastic optical reconstruction microscopy (STORM) [7]), it enables the super-resolution microscopy which was awarded the Nobel prize in 2014 [8]. However, due to the sequential point scanning scheme, the sampling process of the confocal arrangement is much slower. Additionally, the whole sample will be irradiated by the excitation light at a high intensity which may cause photobleaching and phototoxicity effects to the biological sample.

Recently, the light-sheet fluorescence microscopy (LSFM), also named selective plane illumination microscopy, is gaining popularity as a new form of fluorescence microscopy. As shown in Figure 6.1 (c), the key feature of a light-sheet microscope is its illumination path being perpendicular to the imaging path. A thin light-sheet is projected into the sample from the side to illuminate the entire focal plane of the imaging objective at the same time. There is no emission light from the out-of-focus part, thus only the illuminated plane can be recorded. Comparing with the conventional epi-fluorescent microscopy, the light-sheet microscopy has the same lateral resolution but can achieve a better signal-to-noise ratio by this optical sectioning procedure. The field of view with a good axial resolution is limited by the Rayleigh length of the illumination light-sheet. A three-dimensional fluorescent image of the sample can be generated by stacking the recordings from a number of sections which is much faster than the confocal scanning microscopy. Meanwhile, with planar optical sectioning, the light-sheeted scan through the whole sample can be avoided so that the sample absorbs much less radiation from the illumination. Therefore, with all these properties of 3D imaging, speed and low phototoxicity, the light-sheet microscope is considered a promising tool for *in vivo* biological imaging applications.

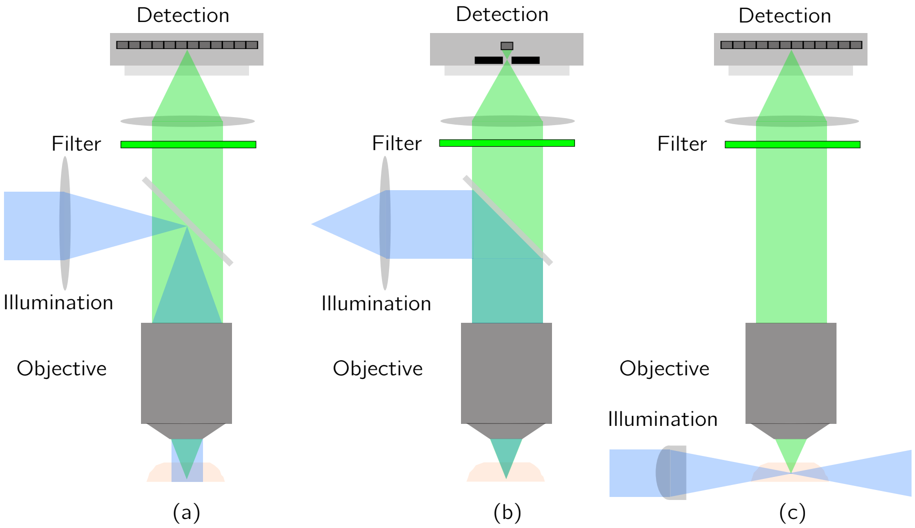

Figure 6.1: Configurations of fluorescence microscopes: (a) is classical epi-fluorescence microscopy. (b) is confocal microscopy. (c) is light-sheet microscopy.

6.2. Variants of LSFM for high-resolution imaging and compatibility

The typical configuration of LSFM is formed by the orthogonal arrangement of two objective lenses or one cylindrical lens with one objective lens. However, such a configuration is usually too bulky to be compatible with many existing microscopy systems. Furthermore, when it comes to the high resolution imaging case, high numerical aperture lenses which have a short working distance are needed. For example, a common objective with a NA of 0.65 has a working distance of 0.65 *mm*. It will easily lead to a spatial constraint issue in the implementations. These incompatibilities obstruct the widespread use of LSFM in the many applications.

Thus there are many variations of LSFM to meet the challenges of high resolution imaging and compatibility problems. In the work of J. Gerhardt et al. (2013), they developed a reflected light-sheet microscopy (RLSM) to achieve single-molecule imaging [9]. In the RLSM geometry as shown in Figure 6.2 (a), the illumination objective and detection objective are parallelly arranged. A small disposable mirror modified from AFM cantilever holder is placed close to the sample reflects the sectioning laser beam by 90°. Both illumination and detection objectives can be chosen with high numerical aperture in this geometry.

Instead of using two objectives, Elisa Zagato et al. implemented a single objective single plane illumination microscopy (SoSPIM) in 2017 [10]. It is an on-chip light-sheet microscope with an integrated micro-mirror in the sample holder as illustrated in

Figure 6.2 (b). The excitation laser beam is shaped and passes through the objective lens. The fluorescent emission is collected by the same lens. This method needs a dedicated sample holder and a relatively complex optics for controlling the light-sheet. Also, only one layer of the sample can be sectioned in the original design.

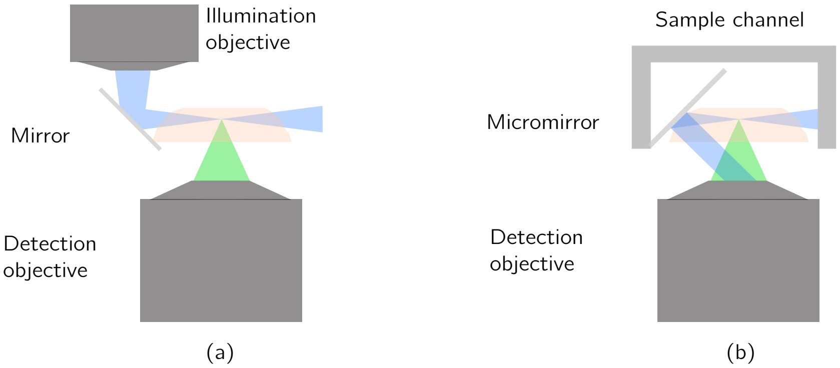

Figure 6.2: (a) A typical reflected light-sheet microscope (RLSM). (b) A variant of RLSM by using a single-objective lens (SoSPIM).

Apart from the reflected schemes, other methods based on the waveguide are developed. In the work of H. Deschout et al., a microfluidic chip was developed as a sample holder with light-sheet illumination integrated [11]. It is used for fluorescence single particle tracking and membrane vesicles characterization. Figure 6.3 (a) shows the scheme of this method. The excitation laser light is coupled into a slab waveguide through a single mode fibre. This waveguide is also designed to support mono-modal propagation. A core layer of $\sim 5\ \mu m$ thickness is sandwiched by two $\sim 25\ \mu m$ cladding layers. Their refractive indexes are $n_{core} = 1.595$ and $n_{cladding} = 1.594$ respectively. The light spreads out horizontally to illuminate the whole microchannel, while in the vertical direction, the spread is confined within the core. The light will diverge slowly right after the waveguide so that the thickness of the light-sheet in the field of view is usable for the specific measurement. An average light-sheet thickness of $\sim 9\ \mu m$ is achieved in experiments.

M. Plöschner et al. introduced an approach to deliver the light-sheet via an extremely narrow multimode fibre [12]. The small footprint of fibre tip (in the scale of 10s of μm) have the potential to allow the light-sheet to penetrate deeper into living samples. As illustrated in Figure 6.3 (b), coherent laser is firstly shaped by a spatial light modulator and then coupled into the multimode fibre. Due to multiple modes can be supported by the fibre, the light can be engineered to scan and focus after the end facet. Both Bessel beam and structured Bessel beam, which are considered to be superior to Gaussian beam in terms of resolution and field of view, can be delivered with the holographic manipulation of input optical fields. The correct generation of light-sheet requires the full transformation matrix of the illumination optics . However, the fibre is not a robust optic element, its transformation matrix will be affected easily due to the bending from any mechanical movement or even thermal effect. Then the realtime measurement of the transformation matrix is needed to guarantee the light-sheet quality which demands an extra complex setup.

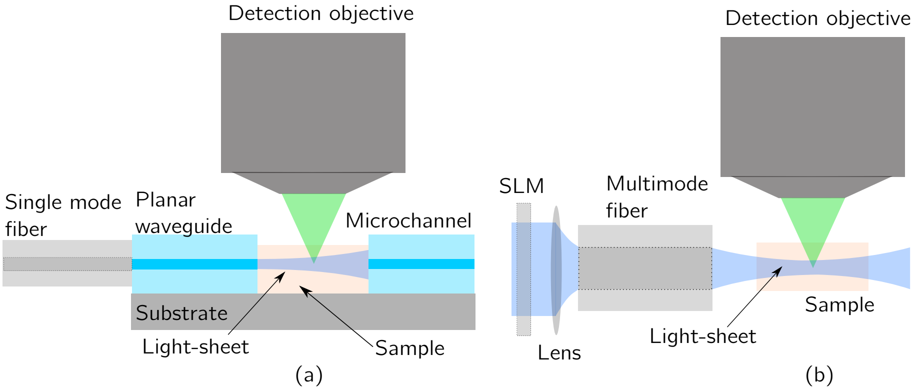

Figure 6.3: LSFM configuration with a planar waveguide (a), and with multimode fibre (b).

In the goal of miniaturizing LSFM, C.J Engelbrecht et al. provided a solution named mini SPIM by combining the fibre optics with gradient-index lens (GRIN) assemblies [13]. As described in Figure 6.4, the excitation light was delivered through a single-mode fibre and then shaped to a light-sheet by passing through an optics assembly consists of a collimation lens, a cylindrical GRIN lens, a glass spacer and a micro-prism deflector. Another assembly consisting of two GRIN lenses with different NAs collected the fluorescence emission and coupled it into a coherent fibre bundle for imaging. A light-sheet of a 4.6 μm FWHM in the centre has been achieved in the mini SPIM implementation.

Although there are several solutions that have been listed above, they are mostly targeted on very specific applications. A tool that can easily convert any imaging microscope into a LSFM with a low cost in money, time and effort is yet not broadly available to the biology and medical community. Inspired by all these previous work, in these chapter, we investigate two miniaturized light-sheet illumination schemes based on self-imaging slab waveguide and customized GRIN lens assembly respectively. These solutions are able to provide both simplicity and good stability in practice.

6.3. Light-sheet illumination with a self-imaging slab waveguide

Considering the work of M. Plöschner et al., the multimode fibre has the ability to focus the light after the distal end and control the output light-sheet with high degree of freedom. But the disadvantage of the multimode fibre is its flexibility brings uncertainty to the transformation matrix of the optical path. Thus, the system needs active control with spatial light modulator. Here we propose a solution by transporting the light-sheet, generated from the classical cylindrical optics, to the sample with a solid slab waveguide. This waveguide is based on the Talbot self-imaging effect which has a stable performance in terms of the light transforming.

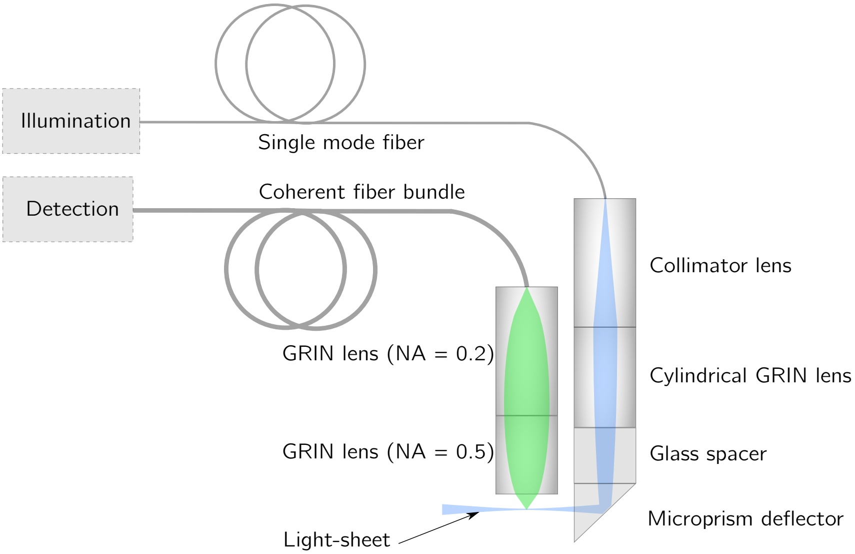

Figure 6.4: Miniaturizing light-sheet configuration with GRIN lenses.

6.3.1. Talbot effect in slab waveguide

Talbot effect, also referred to self-imaging, is a phenomenon that when a periodic object is illuminated by coherent light, the structure will appear repetitively at certain distances due to the free-space propagation. In other words, a complex amplitude field has a period of p in the lateral direction, $U(x+p,z) = U(x,z)$, is also periodic along the propagation direction: $U(x, z + z_T) = U(x,z)$. The period in the axial direction $z_T$is called Talbot distance which is decided by the light's wavelength and the lateral period: $z_T = 2p^2/\lambda$. This effect was first observed by Henry Fox Talbot in 1836 [14] and then received a wide studies on its fundamental features and applications, like imaging processing and optical metrology, in the fields from classical optics to non-linear optics and quantum optics [15].

R. Ulrich et al. and E. E. Grigor'eva et al. have studied the self-imaging phenomenon in waveguide [16, 17]. For a simple explanation, the light transmission in multimode waveguides virtually forms a periodic structure due to the self-reflection. Essentially, the self-imaging phenomenon is a superposition of a proper set of modes with phase coincidence [18]. Thus, it will occur regardless of whether it is in free space or an in-homogeneous medium [19]. For the purpose of generality, we analysis the fundamental points in terms of wave propagation and modes superposition as follows.

Given a planar waveguide in Figure 6.5. A layer of dielectric material with a thickness of W and refractive index of n_0 is sandwiched by claddings with a refractive index of n_1. $n_0 > n_1$ and the refractive index contrast is high so that internal reflection will happen.

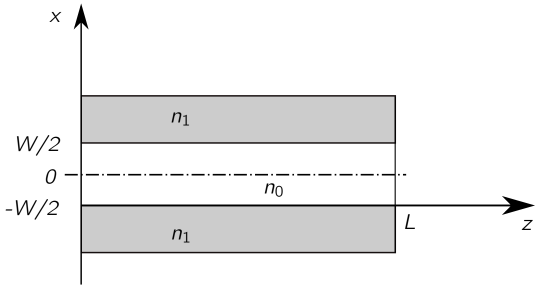

Figure 6.5: Scheme of a planar waveguide.

Assuming the optical field at the input facet ($z = 0$) of the planar waveguide is $E(x, z_0)$. This distribution can be represented as the superposition of an infinite number of waveguide wave functions $F_m(x, z_0)$ with the amplitude coefficients a_m:

$$E(x, z_0) = \sum_{m=1}^{\infty} a_m F_m(x, z_0), \tag{6.1}$$

The light will propagate in the waveguide with different propagation constants β_m for each mode. The guided modes number M to a distance $z \gg \lambda$ in the waveguide is finite. Thus after a distance z, the optical field is:

$$E(x, z) = \exp(i\beta_1 z) \sum_{m=1}^{M} a_m F_m(x, z_0) \exp[iz(\beta_m - \beta_1)]. \tag{6.2}$$

The field $E(x, z)$ will be the image of input $E(x, z_0)$ when the phase changes of various propagating modes differ by integer multiples of π or 2π, in other terms, it is:

$$\exp[iz(\beta_m - \beta_1)] = 1 \; or \; (-1)^m, \; (m = 1, ..., M). \tag{6.3}$$

The possibility of image formation by a guide is decided by the existence of a solution to the above equation. For a planar multimode waveguide, the propagation constant β_m is:

$$\beta_m = \frac{2\pi}{\lambda} n_0 \sqrt{1 - \left(\frac{\lambda}{n_0 \lambda_m}\right)^2}, \tag{6.4}$$

where the cutoff wavelength is $\lambda_m = 2W/m$ for the rectangular waveguide.

The phase difference between the wave of two modes with indices m and 0 after propagating over a length of z is:

$$\varphi_{m,0} = \frac{2\pi n_0 z}{\lambda} \left[\sqrt{1 - \left(\frac{\lambda}{n_0 \lambda_m}\right)^2} - \sqrt{1 - \left(\frac{\lambda}{n_0 \lambda_1}\right)^2} \right]. \tag{6.5}$$

The binomial series expansion of the function $f(x) = (1+x)^\alpha$ is

$$\begin{aligned}(1+x)^\alpha &= \sum_{k=0}^{\infty} \frac{\alpha(\alpha-1)(\alpha-2)\cdots(\alpha-k+1)}{k!} x^k \\ &= 1 + \alpha x + \frac{\alpha(\alpha-1)}{2!} x^2 + \cdots ,\end{aligned} \tag{6.6}$$

where $\alpha \in \mathbb{C}$ is an arbitrary complex number.

Given $x = -\left(\frac{\lambda}{n_0\lambda_m}\right)^2$ and $\alpha = \frac{1}{2}$. We also check the condition for convergence, $|x| < 1$, which means $\frac{\lambda}{n_0\lambda_m} < 1$. The first two terms of the expansion 6.6 is:

$$1 - \frac{1}{2}\left(\frac{\lambda}{n_0\lambda_m}\right)^2 . \tag{6.7}$$

Then equation 6.5 can be approximated by:

$$\begin{aligned}\varphi_{m,0} &\approx \frac{2\pi n_0 z}{\lambda}\left[\frac{1}{2}\left(\frac{\lambda}{n_0\lambda_1}\right)^2 - \frac{1}{2}\left(\frac{\lambda}{n_0\lambda_m}\right)^2\right] \\ &= \frac{\pi z\lambda}{n_0}\left(\frac{1}{{\lambda_1}^2} - \frac{1}{{\lambda_m}^2}\right) \\ &= -\frac{2\pi z\lambda}{8n_0W^2}\left(m^2-1\right) .\end{aligned} \tag{6.8}$$

The term m^2-1 is always integer. When it is odd, to have an image of the input, all the inter-mode phase differences should be a multiple of 2π. The condition can be satisfied with the following equality that:

$$z_T = \frac{8n_0W^2}{\lambda} N, \tag{6.9}$$

where $N = (0, 1, 2, ...)$.

At this point, the paraxial mode superposition will create an image of the input field.

When m^2-1 is even, an image of the input source inverted with respect to the axial plane of the waveguide is formed in the cross sections which is also called intermediate images:

$${z_T}' = \frac{4n_0W^2}{\lambda}\left(2N+1\right) . \tag{6.10}$$

Due to the field penetration into the confining walls between the core and claddings of dielectric waveguide, the real waveguide width W must be replaced by an effective width. It can be calculated as below:

$$W_{eff} = W + (\lambda/\pi)\left(n_1/n_0\right)^{2\rho}\left(n_0^2 - n_1^2\right)^{-1/2}, \tag{6.11}$$

where $\rho = 0$ for TE modes and $\rho = 1$ for TM modes.

Thus conditions in equations 6.9 and 6.11 can be used to design the waveguide that can reproduce the input. Then the LSFM system can be designed as Figure 6.6. The light-sheet is generated at the front end of the waveguide. In theory, it will be transported to the back end. The light can be focused at a distance from the end facet. Also, for the dielectric waveguide, the maximum numerical aperture is decided by:

$$NA = \sqrt{(n_1^2 - n_2^2)}. \tag{6.12}$$

Therefore, the material of the core and claddings can be chosen to support a relatively high numerical aperture out put to satisfy the high resolution requirements.

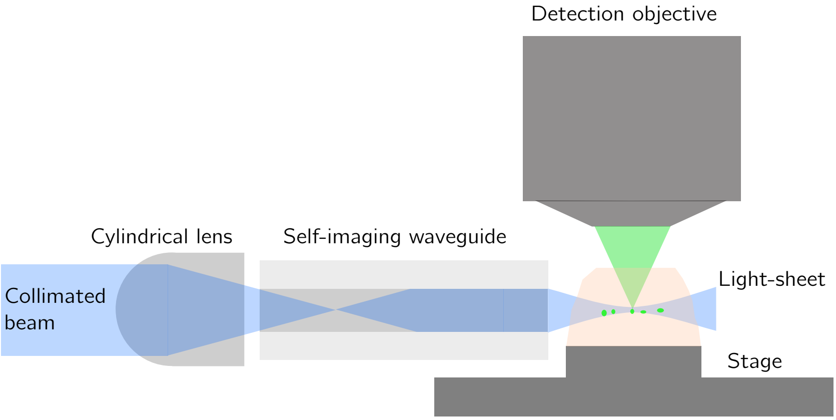

Figure 6.6: Scheme of a light-sheet microscope with a self-imaging waveguide illumination.

6.3.2. Beam propagation simulation in self imaging waveguide

Before we implementing the self-imaging waveguide system in experiment, we first investigated its performance of light-sheet transportation in simulations. The design and optimization of a waveguide structure is usually first simulated by numerical wave propagation techniques first.

There are many beam propagation algorithms that have been developed. The beam propagation method (BPM) is one of the most popular techniques to investigate the optical fields in waveguides, integrated photonic devices and free space. To solve the Maxwell's equations, it is assumed that the light has a predominate propagation direction and the power so that it meets the paraxial approximation. The dielectric constant (or refractive index) distribution $n(x, y, z)$ is assumed to vary slowly along the propagation direction z: $\partial n / \partial z \approx 0$. Under this assumption, the light propagation can be applied with the slowly varying envelope approximation that $\partial^2 A(x, y) / \partial y^2 \approx 0$, where $A(x, y)$ is the envelope of the optical field amplitude. The speed of the calculation can be accelerated by using fewer steps without of much accuracy. Thus, the BPM is very efficient for simulating the non-uniform structure with the scale much larger than wavelength.

Here we choose the Beamlab (https://www.codeseeder.com, Czech Republic) to evaluate the performance of the waveguide we designed. It implements the finite differences BPM (FD-BPM) technique in Matlab environment accelerated by parallel computing. FD-BPM is able to treat full vectorial propagation in large refractive index contrast optical waveguides and has a relatively high computational efficiency. Thus, it is very powerful tool and has been widely used for optical waveguide guide design.

Simulation of Talbot effect in slab waveguide

To begin with, we simulate the Talbot effect in a three layered slab waveguide as the same structure of Figure 6.5. To minimize the cost of the design, we choose the waveguide materials from the most commonly used glass categories. In the simulation, the waveguide core is glass BK7 with refractive index $n_0 = 1.522$ and the width $W = 50\ \mu m$. The surrounding claddings are fussed silica with refractive index $n_1 = 1.463$. The total thickness of the waveguide is $T = 150\ \mu m$ and the wavelength is $\lambda = 488\ nm$. According to equations 6.10 and 6.11, the effective core width is $W_{eff} \approx 50.37\ \mu m$ and the Talbot distance is $z_T \approx 63.3\ mm$.

A Gaussian beam with a waist $w_0 = 0.2W = 10\ \mu m$ is incident from the edge centre of the waveguide. Figure 6.7 shows the intensity of the beam propagation within the waveguide. The simulation result shows that the approximated Talbot distance is $z_T \approx 63.6\ mm$ which matches the analytical calculation. While the result also shows that the input is reproduced at positions of multiples of $z_T/8$.

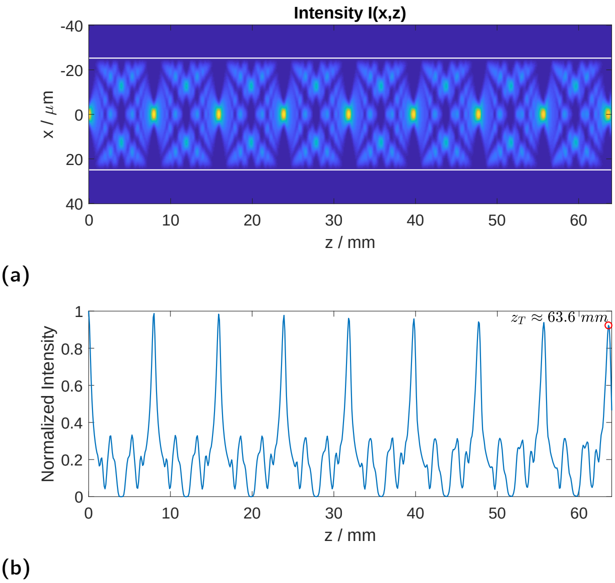

Figure 6.7: Simulation of Talbot effect in a slab waveguide. (a) Propagation of a Gaussian beam input ($\lambda = 488\ nm$) in the waveguide. (b) The intensity section along the propagation direction at $x = 0$.

Figure 6.8 shows the simulation with the input beam shifted by 5 μm. With an offset to the centre, only at the positions of multiples of $z_T/2$ the input is reproduced. At the position $z = z_T/2$, the intermediate image of the input appears. It is exactly shifted opposite with the offset of the input. Figure 6.9 simulated the situation that the input beam has a tilted angle of $\theta = 1°$. It is very interesting to find that the highest intensity does not appear at the input plane but at the position $z = z_T/4$. The image is shifted about 1.5 μm. At this length, the waveguide converts tilts to offsets and vice versa. This length has the potential to realize a self-image and may be used as a light-sheet scanner. However, due to the unavoidable input misalignment that occur in practice, this case with its very strict operating conditions is a relatively poor choice for stable self-imaging. The positions like $z = Nz_T/2$ *and* Nz_T are less sensitive to the alignment which can be chosen as the designed waveguide length.

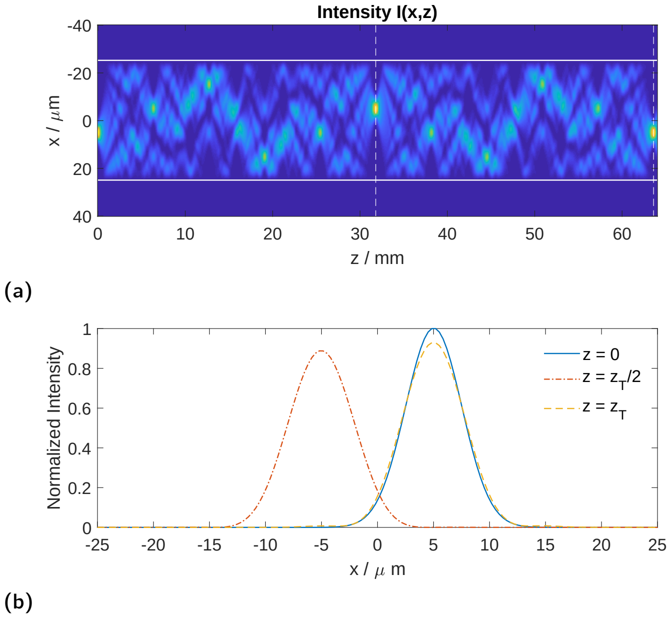

Figure 6.8: (a) Simulation of light propagation in the waveguide with a shifted Gaussian beam input. The offset is 5 μm. (b) The intensity profiles at plane $z = 0, z_T/2, z_T$.

Effect of waveguide length

The transporting performance of different waveguide lengths has been investigated in Figure 6.10. The laser beam quality is characterized by means of beam width and the beam propagation factor M^2. In this context, the beam width is defined by the full width at half of the maximum intensity (FWHM). And M^2 is a parameter which describes how much the real beam is different from the input Gaussian beam. It is defined as a ratio:

$$M^2 = \frac{w_R \theta_R}{w_0 \theta}, \tag{6.13}$$

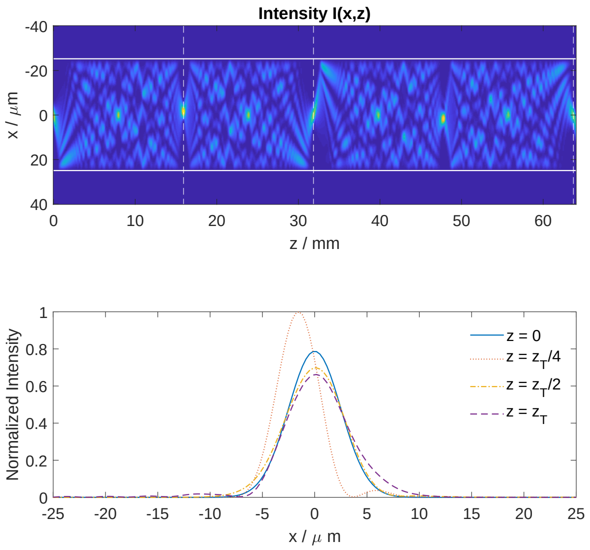

(a)

(b)

Figure 6.9: (a) Simulation of light propagation in the waveguide with a tilted Gaussian beam input. The tilted angle of incident light is $\theta = 1^\circ$. (b) The intensity profiles at plane $z = 0, z_T/4, z_T/2, z_T$.

where w_0, w_R and θ, θ_R are the beam waist radii (the width at $1/e^2$ intensity points) and divergence angles of the input beam and real beam respectively.

From the results in Table 6.1, we can see that the beam width of the focal spot is ambiguous to character the beam quality. But the M^2 shows the reproduced beam slightly decay from the input Gaussian beam with the self-imaging distance increases. Thus, in the design, if there is no practical need based on the optical configuration, we prefer to choose the shortest but stable waveguide length for self-imaging. In the following design, the waveguide is chosen with a length of $z_T/2$.

Position	FWHM (μm)	M^2
$z = 0$	5.69	1
$z = z_T/2$	6.36	1.09
$z = z_T$	6.36	1.09
$z = 2z_T$	7.03	1.11
$z = 3z_T$	6.36	1.22

Table 6.1: Beam qualities at different positions along the propagation direction in Figure 6.10.

Effect of waveguide roughness

It is also important to check how stable the self-imaging waveguide with reference to the input beam quality with various optical fabrication imperfections. We always prefer to achieve an acceptable output performance with a relatively low cost. Thus, it is

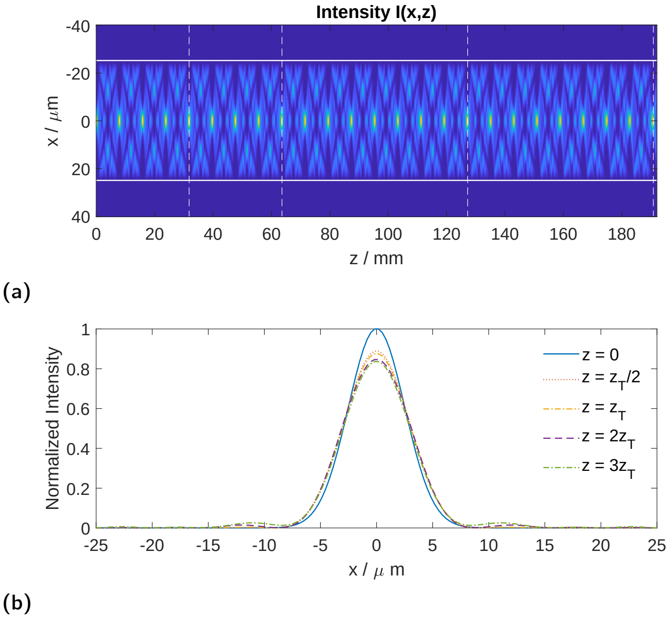

Figure 6.10: (a) Simulation of light propagation in the waveguide with a length of $L = 3z_T$. (b) (b) The intensity profiles at plane $z = 0, z_T/2, z_T, 2z_T, 3z_T$.

useful to guide the selection of the raw glass wafers. If we propagate the light-sheet through a rather rough waveguide as the extreme case simulated in Figure 6.11. The light is found to be dispersed randomly at the self-imaging distance.

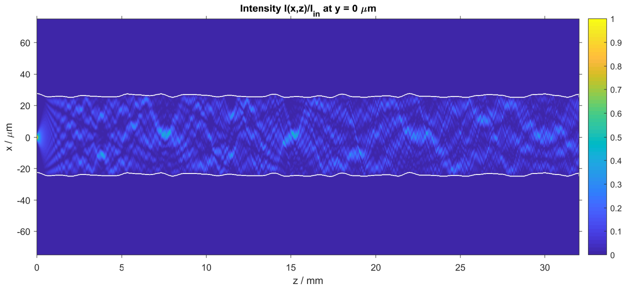

Figure 6.11: Light-sheet propagates through a waveguide with coarse dielectric walls. The offset of the thickness is 10λ.

We simulated a Gaussian beam (FWHM = 3.18 μm) propagating through a 50 μm layer of fused silica (n = 1.46) with water (n = 1.33) as the cladding medium. In this case, the waveguide is set to a self-imaging distance as half of the Talbot distance: $z_T/2 \approx 30.3\ mm$. The waveguide is discretized into 100 sections. Each section is shifted a certain range from the center leading to a rough surface of the core layer with different peak-to-valley (PV) heights. The FWHM and intensity of the reproduced focus are recorded with varying PVs. The results are shown in Figure 6.12. From a PV value from 0 to λ/5, the FWHM and intensity remain in the same level. The measured M^2 ratios are usually below 3. During λ/2 to 2λ, the re-focused beam slightly expanded from the base level 3.18 μm, and the transported intensity drops gradually. But the M^2 becomes hard to measure due to the focused beam no longer maintaining the Gaussian shape. With the PV increasing to more than 2λ , the light disperses quickly and is not able to reproduce the input beam properly. The results suggest that a core layer should have a roughness characterized by PV be at a sub-wavelength level.

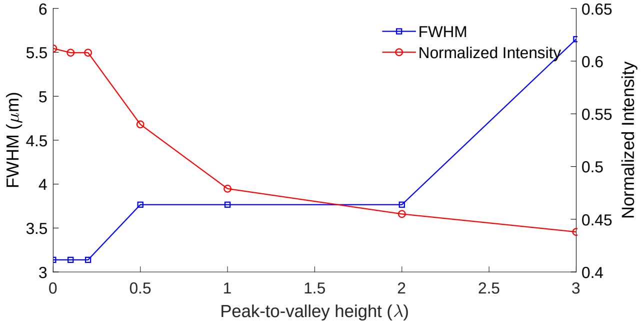

Figure 6.12: The delivered light-sheet performance (FWHM and normalized intensity) versus the roughness of the dielectric wall (indicated by peak-to-valley height).

Two configurations

Arranging the cylindrical lens and the self-imaging waveguide so that the light-sheet be reproduced after the distal end could have two configurations: (a) The light-sheet is formed after the front end of the self-imaging waveguide. (b) The light-sheet is formed on the front end and then is transported by a waveguide slightly shorter than the self-imaging length.

These two configurations have been simulated in Figure 6.13. The incident source is a uniform beam has the width of the waveguide core width 50 μm. It is focused by a thin lens, represented by the yellow bar in the figures, with a focal length of $F = 0.5\ mm$. Thus, the NA of the input beam is 0.05. The waveguide is simply formed by immersing a fused silica wafer in water.

The configuration (a) used a full self-imaging length waveguide, $L = z_T/2$. The input optical field is straightforwardly reproduced after the lens, thus the light keeps converging as the input beam. The configuration (b) used a shorter version of waveguide, its length is $L = z_T/2 - F$. In these cases, the supported propagation modes are not as many as the previous one. But in the sense of reconstructing the beam with certain NA, these two are equivalent. It can be seen from the section of the light-sheet waist position in Figure 6.14 (a). These two intensity profiles are almost coincident in the simulation. But when the length becomes shorter than $L = z_T/2 - F$, as recorded in Figure 6.14 (b), the FWHM of the light-sheet waist increases, and the intensity drops. As a result, the waveguide is not able to reproduce the beam with the same input NA any more.

The shorter self-imaging waveguide enables a flexibility in arranging the illumination system. For example, the light-sheet is able to scan vertically with a fixed waveguide and a scanning input. But to keep the same performance, we have to choose the length according to the NA of the input beam. If a high NA should be supported, then usually this difference of waveguide length is negligible.

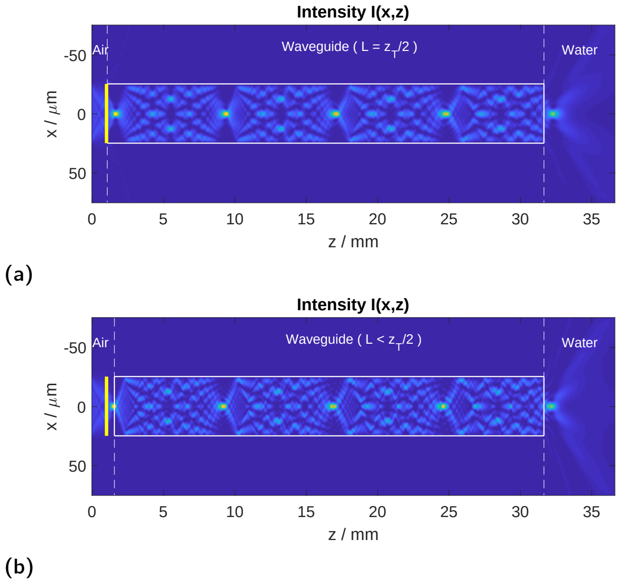

Figure 6.13: Two configurations of arranging the cylindrical lens and the self-imaging waveguide: (a) With a waveguide ($L = Z_T/2$), the light-sheet is formed after the front end of the self-imaging waveguide. (b) With a waveguide ($L < Z_T/2$), the light-sheet is formed on the front end.

6.3.3. Experimental realization

We designed the simplest form of the self-imaging waveguide to have a quick validation of the feasibility for light-sheet propagation in experiment. The scheme of this experiment is shown in Figure 6.15.

Fused silica ($n = 1.463$ in $\lambda = 488\ nm$) has been used as core medium. Due to its high refractive index, it can form a waveguide with air ($n = 1.00$ in $\lambda = 488\ nm$) as the "cladding" layer. In theory, it can support a very large numerical aperture up to 1.06 due to this high refractive index contrast. Later, it can also be protected with optical adhesives or other substrates with a suitable lower refractive index in any large scale fabrication.

According to equations 6.9 and 6.11 , we know the half Talbot distance is 30.2 mm. To make a room for the working distance, we diced a rectangular slice of dimensions

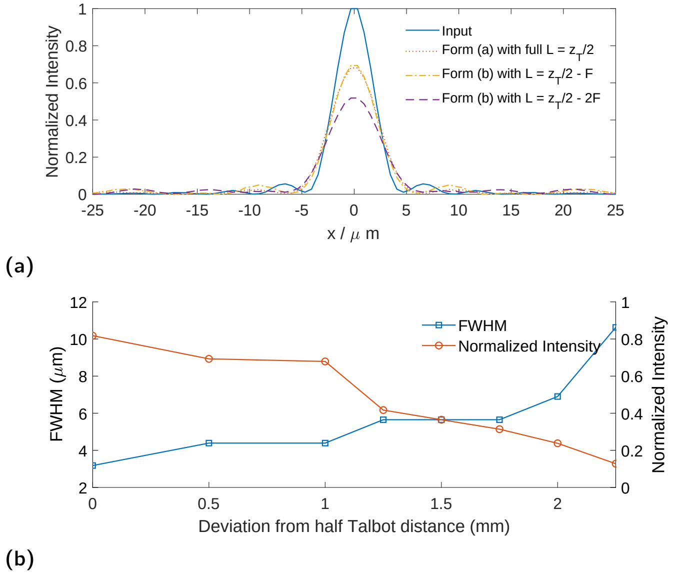

Figure 6.14: (a) The profiles of the input light-sheet and the output light-sheet with different waveguide lengths. (b) The FWHM and normalized intensity of the output light-sheet versus the length deviation from the self-imaging distance $L = z_T/2$.

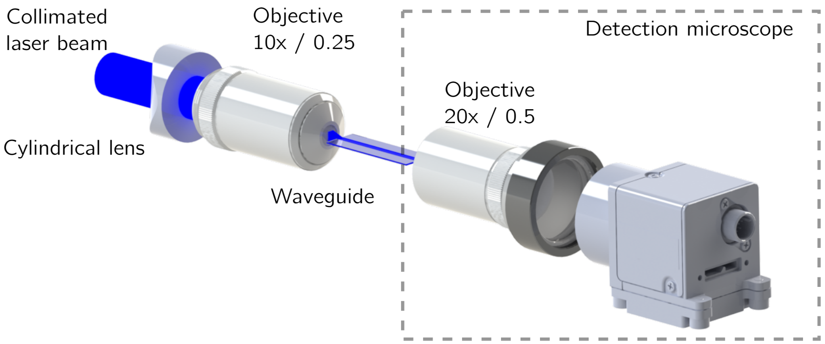

Figure 6.15: The scheme of the self-imaging waveguide experimental setup.

10 $mm \times 29.2\ mm$ from a 76.2 mm diameter double side polished wafer. The surface roughness is less than 100 ångström. After dicing the two sides that light passes through are polished with fibre polishing sheets. The waveguide is glued on a three-dimensional adjustable stage and is arranged as seen in the photo Figure 6.16:

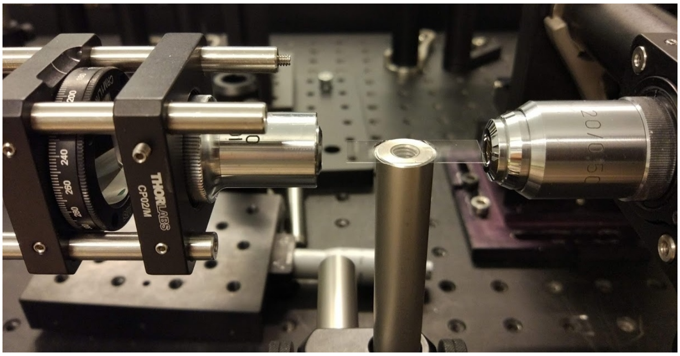

Figure 6.16: A waveguide is glued on a pole which is mounted on a XYZ stage. The light-sheet is generated on the left side and is detected by the microscope on the right side after the propagation in the waveguide.

A fibre coupled laser source ($\lambda = 488\ nm$, MCLS1, Thorlabs, US) is expanded to a collimated beam by a telescope to match the size of the full aperture of the microscope objective (10×, NA = 0.25, Olympus, Japan). A cylindrical lens ($F = 25\ mm$) is used before the objective to cancel the focusing power in the horizontal direction. Thus, a light-sheet is formed in the objective's focal plane. A microscope is built to characterize the light-sheet. It consists of an objective lens (20×, NA = 0.50, Olympus, Japan), a tube lens ($f = 200.0mm$,AC254-200-A, Thorlabs, US) and a CMOS camera (pixel size 5.9 μm,UI-3060 CP-M-GL,IDS, Germany). After calibration, the total magnification of the microscope is 25×.

To start, the input light-sheet is characterized by the microscope. A $500 \times 500px$ region-of-interest (ROI) of the original $1936 \times 1216px$ image from the microscope camera is shown in Figure 6.17. The input light-sheet has a FWHM of 1.65 μm which is slightly degraded from the theoretical diffraction limit 1.19 μm.

After a fine tuning of the XYZ stage, we coupled the light-sheet into the waveguide from the left side. The output from the waveguide is monitored by the detection camera. Again a fixed $500 \times 500\ px$ ROI window is selected. In Figure 6.18 (a), we focus the microscope on the right edge. The intensity distribution indicates the thickness of the core layer. Also, multiple interference fringes are visible at this plane. When focusing a distance (about 500 μm) after the end facet, the scatter image of the edge has been blurred. However, a light-sheet is clearly visible in Figure 6.18 (b). We plot the averaged intensity profile of this plane in Figure 6.18 (c). The FWHM of this light-sheet is measured to be 4.72 μm which is 2.86 times of the input light-sheet thickness.

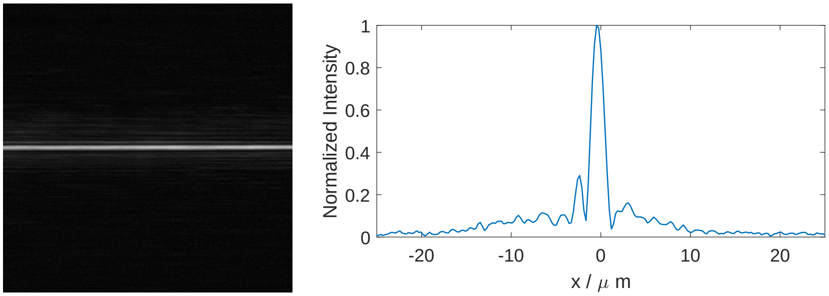

(a) (b)

Figure 6.17: (a) Focus of the input light-sheet generated from the cylindrical lens and microscope objective. (b) Averaged intensity profile of the light-sheet in (a).

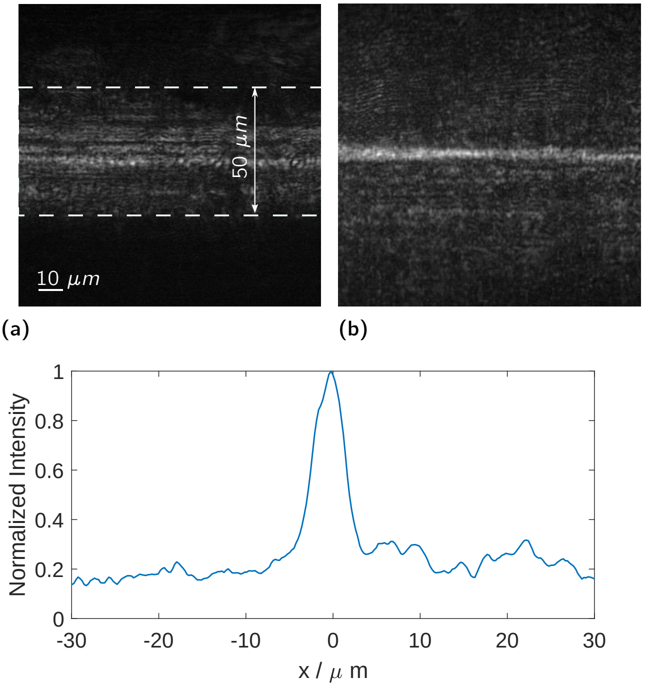

(a) (b)

(c)

Figure 6.18: (a) The intensity distribution on the plane of the waveguide edge. (b) The intensity distribution on the plane of the light-sheet waist. (c) Averaged intensity profile of the light-sheet in (b).

6.3.4. Discussion

From the experiment results, we can see that a light-sheet has been successfully reproduced by a specifically designed self-imaging waveguide. However, we also note that passing through the waveguide brought a certain extent of degradation to the initial light-sheet input. From the above simulation results, we can also analyse the causes behind this.

Firstly, there is an expansion of the light-sheet thickness in the experiment. Besides misalignment, it could also be caused by low aberrations introduced by the non-uniformity of the waveguide thickness and the material refractive index. In the experiment, we can try to compensate this aberration with the help of phase plate or spatial light modulator (SLM), though it will increase the cost of the system. Another factor involved could be the manufactured waveguide length being shorter than the actual half Talbot distance. It can be investigated in the following experiment by rotating the waveguide or varying the refractive index of cladding medium to achieve a different equivalent waveguide length.

Secondly, due to the background noise, the intensity contrast of the light-sheet drops from the initial 0.990 to 0.757 in the core area. The background speckle noise is mainly caused by the poorly polished input and output facets. The technique of polishing such a thin waveguide needs to be improved. The mounting simply with a glue leads to a rough dielectric walls which may also bring high frequency noises.

Although there are much room for the improvement in the experiment, the preliminary results validate the feasibility of transporting the light-sheet to the sample with a low cost self-imaging waveguide. The end footprint of the waveguide can be down to the scale of tens of micrometers which will not interfere with most of the high-numerical aperture imaging objectives. With a relay of the waveguide, the bulky and complex components of the illumination system can be arranged away from the working area which gives much freedom for the design of imaging part and sample holder. Thus, it provides a promising solution for minimizing the LSFM illumination system.

6.4. Miniaturize the light-sheet microscope with GRIN lens assembly

The self-imaging multimode waveguide is able to cover the footprint in a range from tens of micrometers to hundreds of micrometers. However, the form of this self-imaging waveguide is not limited to the three-layer slab waveguide. The graded-index (GRIN) medium in which the refractive index varies gradually is also popular in waveguide construction. As shown in Figure 6.19, in contrast with the step-index multimode waveguide that utilizes the total internal reflection effect, the change of refractive index between the core and claddings is smooth and continuous. Thus, the light ray is refracted rather than being reflected. It could, therefore, realize the self-imaging effect the same as the previous approach.

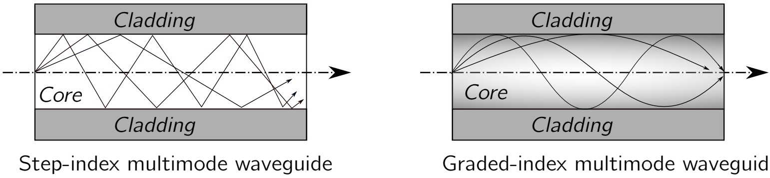

Figure 6.19: The scheme of step-index multimode waveguides (left) and graded-index multimode waveguides (right).

6.4.1. Introduction of GRIN lens

The GRIN lens is a specific form of GRIN waveguides and while it is usually much thicker ($200\ \mu m - 2\ mm$) compared to a multimode fibre. It is a standard off-the-shelf inexpensive component, which is widely used in optical communication and fibre imaging systems. In general, it is a short cylindrical glass tube with a gradient profile distribution of refractive index in its radial direction perpendicular to the optical axis, in the following mathematical form:

$$n(r) = n_0 \left[1 - (k/2)\, r^2\right], \tag{6.14}$$

where n_0 is the refractive index at the lens centre, k is the gradient constant, and r is the radius.

The numerical aperture of a GRIN lens is also related to the index change of the gradient profile,

$$NA_{GRIN} = n_0 \sqrt{1 - \operatorname{sech}^2 (kR)}, \tag{6.15}$$

where R is the semi-diameter of lens.

When a light ray is incident on the front facet of a GRIN lens, it follows a sinusoidal path along the optical axis. The length of the full sinusoidal period is called the pitch P of the GRIN lens. It is defined as:

$$P = 2\pi/\sqrt{k}. \tag{6.16}$$

Instead of varying the shape of surfaces for the conventional optics, the GRIN lenses can be cut to various lengths to perform different functionalities, such as imaging, focusing and collimation, which is shown in Figure 6.20. Similar to the Talbot distance waveguide, the full-pitch GRIN lens can reproduce an image at the front facet identically to the end facet. Meanwhile, a half-pitch lens invert the image at the exit facet. However, they are not mass-produced due to their limited applications. The most commercially available GRIN lens types are quarter-pitch and fractional-pitch (such as 0.23 and 0.29). The 0.25 pitch GRIN lens can image a point on the front facet to infinity which is usually employed as a collimator. And the 0.23 pitch lens and 0.29 pitch lens function as converging lens and diverging lens respectively. Along with their small size, they are widely used for fibre coupling, diode collimation and endoscopic imaging systems.

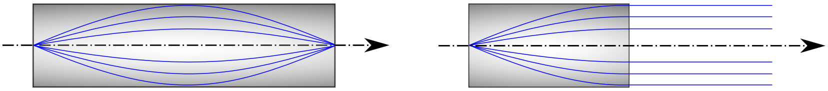

Half-pitch lens for imaging

0.25 pitch lens for collimating

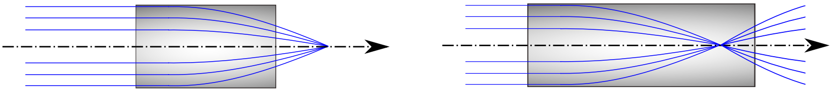

0.23 pitch lens (converging lens)

0.29 pitch lens (diverging lens)

Figure 6.20: Different functionalities of GRIN lenses with various lengths.

More complicated functionalities can be achieved with customized combinations of these GRIN lenses. In our case, we prefer to use a GRIN lens assembly. Most GRIN lenses are available in a length of a few millimeters (i.e. $2-7\ mm$) that will still hinder our arrangement of the light-sheet formation part of the optical system. Cascading the fractional-pitch GRIN lenses as a waveguide can gain us more relay space. One of the simplest configuration that consists of two converging GRIN lenses and a cylindrical lens is presented in Figure 6.21. Besides is, there are many variants according to specific situations.

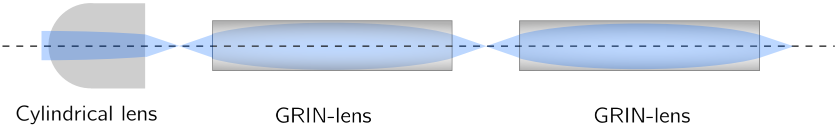

Figure 6.21: The configuration of light-sheet forming by cylindrical lens and two GRIN lenses.

6.4.2. Experimental realization

Here we shall introduce a practical implementation of the GRIN lens based waveguide to generate light-sheet. All the components are intentionally chosen to be available from the shelf.

Optical design

The arrangement of the components needs to be specifically designed. The convex GRIN lens (mostly in the 0.23 pitch) on the market are usually bulk produced for fibre communication applications, which has an angled facet to minimize back reflection or compensate the angled fibre ferrules with surface contacting. It causes difficulties in our case with the optical alignment. Thus, we choose the 0.29 pitch GRIN lens to construct the system since it has a planar facet. Also, the GRIN lenses are designed for the typical communication wavelengths. The optical parameters are different with the fluorescence excitation wavelengths. However, with the aid of the optical system design software, Zemax, and the optical models provided by the manufacturers, we can achieve a working arrangement.

Inheriting the basic scheme from the previous slab waveguide system, the GRIN lens illumination system includes a cylindrical lens (Edmund 48-357, $F = 25$ *mm*, US), an objective lens (10×, NA = 0.25), and two 0.29 pitch GRIN lenses (GRIN2906, Thorlabs, US). This type of GRIN lens has a diameter of 1.8 *mm* and the effective focal length at 630 nm is 1.90 mm, the working distance is 1.411 mm. The distances between the components are adjusted and optimized in the Zemax. All the Zemax models are supplied by the producers. The configuration is shown in Figure 6.22 (a). The objective lens is put 29.50 *mm* after the cylindrical lens. The distance between the objective lens and GRIN lens is 5.59 *mm*. The distance between the two GRIN lenses is 2.35 *mm*. The light-sheet waist is located at 0.25 *mm* after the GRIN lens pair. The theoretical Airy disk radius is 0.52 μm according to the spot diagram in Figure 6.22 (b). Note that, this configuration is yet not the optimal that can be achieved and there is more room for improving the design.

Experimental results

The scheme to test the generated light-sheet in the experiment is arranged as shown in Figure 6.4. The illumination part is arranged as in the previous configuration. According to the simulation results, we 3D printed a GRIN lens holder to ensure the distances, and glued the GRIN lenses in a glass sleeve. The light-sheet is then imaged by a microscope with a 20× microscope objective (NA = 0.5).

Figure 6.24 shows the light-sheet performance from the GRIN lens assembly. The light-sheet is recorded by a CMOS camera. The ROI is 700×700 *px* which is about 165.2×165.2 μm in the field of view. From the measurement of the averaged intensity profile in Figure 6.24 (b), the FHMW of the light-sheet waist is 1.42 μm, which is close to the diffraction limit of the used objective lens. The achieved width of the light-sheet with the smallest beam waist, as indicated in Figure 6.24 (c), is around 100 μm. This is rather a small range compared to the diameter of the GRIN lens. It may be due to the inhomogeneity of the lens medium, which it is the key to form the lens' power. However, this width is already able to cover most of the field of view of the objectives with high numerical aperture used for light-sheet microscopy.

6.4.3. Discussion

A GRIN lens based waveguide light-sheet illumination system has been validated. It successfully reduces the tip end of a light-sheet illumination system to the size of 1.8 mm. A smaller tip end is possible with different types of GRIN lenses without too much effort in re-optimizing the arrangement. According to the preliminary results in the experiment, this scheme can achieve a rather good performance in generating a light-sheet. The realized light-sheet thickness is comparable to the light-sheet generated by the conventional optics components, as shown in Figure 6.17. The illumination with higher NA can also be implemented in theory. It is suitable for the situations where the space requirement is less strict than the previous slab waveguide proposal. However, it has a much more robust mechanical structure. Also, all the components are relatively cheap and available on the market, which is conducive to the community

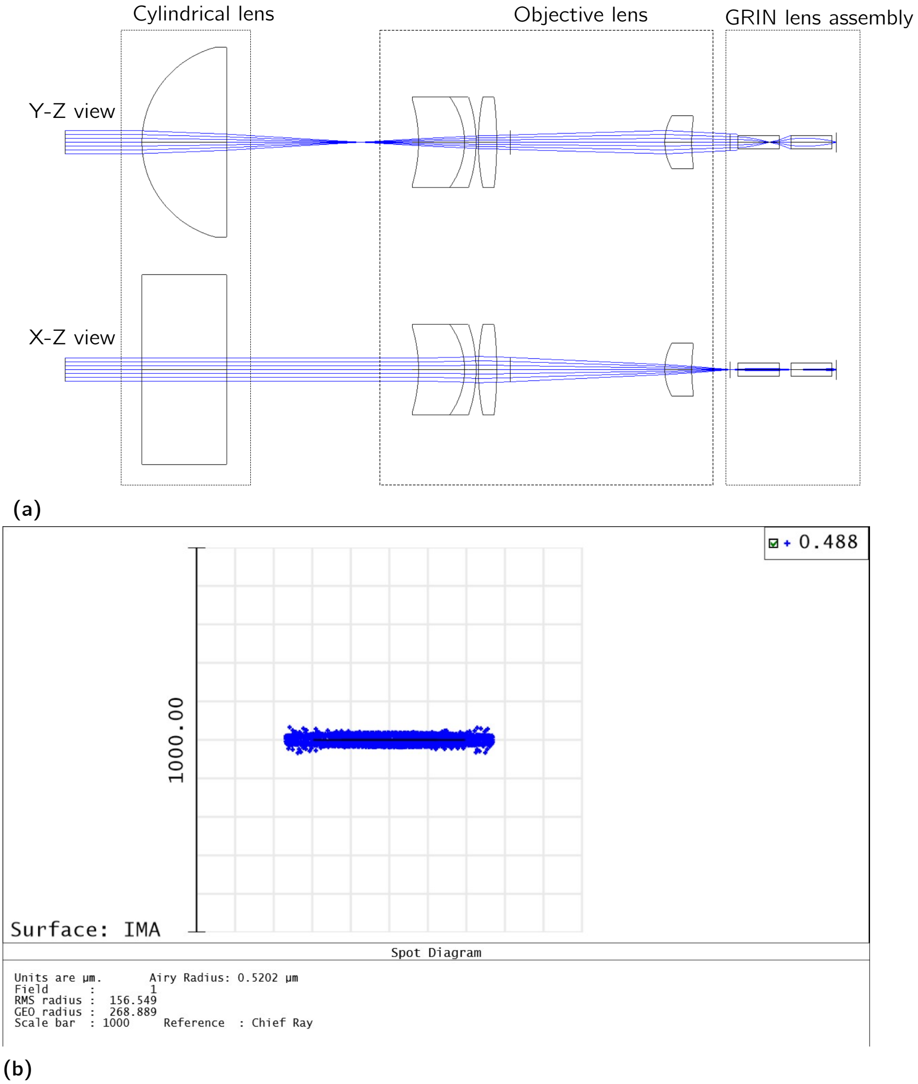

```
Units are µm.        Airy Radius: 0.5202 µm
Field      :           1
RMS radius :   156.549
GEO radius :   268.889
Scale bar  : 1000      Reference   : Chief Ray
```

Figure 6.22: (a)The Zemax model of the GRIN lens waveguide light-sheet illumination system.(b)The spot diagram of the previous Zemax configuration.

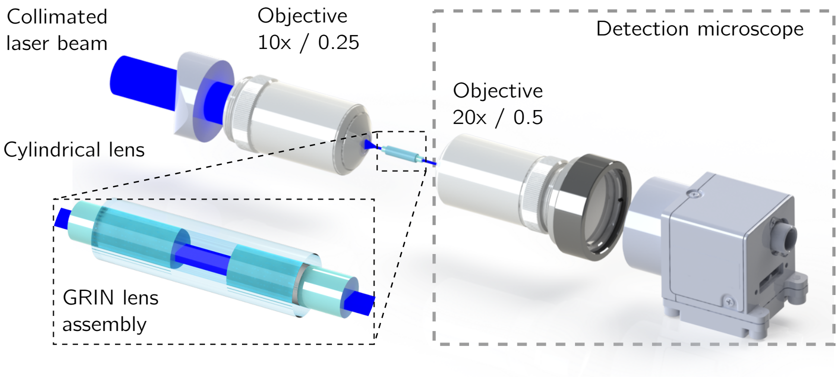

Figure 6.23: The scheme of the GRIN lens assembly waveguide experimental setup.

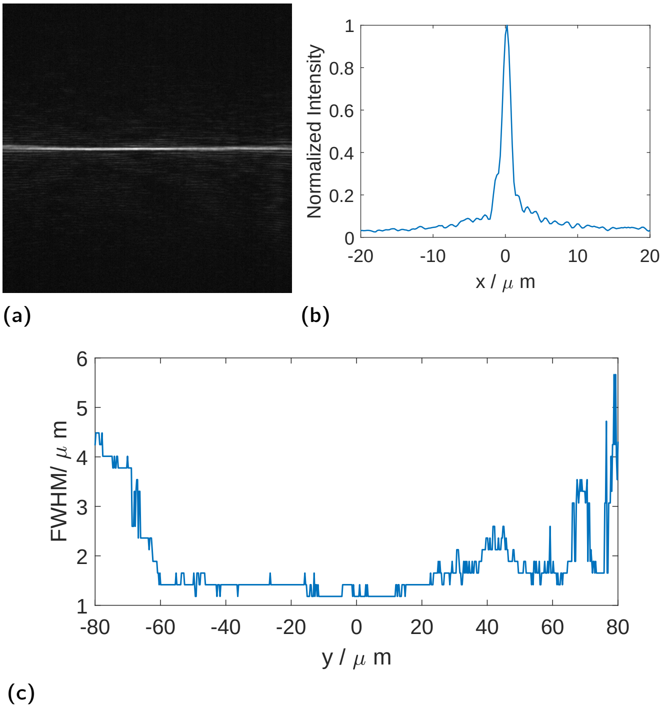

Figure 6.24: (a) Output light-sheet transported by the GRIN lens assembly. The field of view is 165.2 × 165.2 μm. (b) Averaged intensity profile of the light-sheet in (a). The FWHM of the averaged light-sheet is 1.42 μm. (c) FWHM characterization of the full light-sheet waist.

in implementing it without too much customization. The light-sheet quality, such as thickness and width, is naturally limited by the aberrations and imperfections in miniature optics. To a certain extent, it has already met the requirement of many biological imaging applications even at the cellular scale. For a higher performance, not only do the configuration of components need to be optimized, but an additional phase plate or adaptive wavefront corrector could also be added to compensate for those imperfections.

6.5. Conclusion

In this chapter, we have developed approaches to miniaturize the light-sheet generation system based on the idea of multimode waveguide. Two techniques has been demonstrated with the use of a slab waveguide and a GRIN-lens respectively. The slab waveguide is designed based on the self-imaging Talbot effect. A prototype has been fabricated and tested in the experiments. A light-sheet with thickness of a 4.72 μm FMHW was formed after the slab waveguide. This technique allows minimizing the tip end of the illumination arm to the scale of tens of microns. The GRIN lens system is a form of cascaded GRIN lenses. It is able to achieve a tip end cover the range between hundreds of microns and several millimeters. An experimental configuration has been implemented with the off-the-shelf components. It has successfully conducted a light-sheet with a waist of 1.42 μm thickness and $\sim$ 100 μm width, with respect to a 1.8 mm diameter tip end.

These experiment results verify the feasibility of miniaturizing the light-sheet illumination with different forms of waveguide. Although the preliminary results show some degradation in the light-sheet generation, this can be improved by optimizing the optical design and careful fabrication. The application of these illumination techniques need to be combined with specifically designed sample holder and imaging system configuration. The approach for adaptive control of the light-sheet through this waveguide is going to be investigated in the future.

References

[1] J. W. Lichtman and J.-A. Conchello, *Fluorescence microscopy,* Nature Methods **2**, 910 (2005).

[2] N. Ji, H. Shroff, H. Zhong, and E. Betzig, *Advances in the speed and resolution of light microscopy,* Current Opinion in Neurobiology **18**, 605 (2008).

[3] D. J. Webb and C. M. Brown, *Cell Imaging Techniques*, 2nd ed., edited by J. M. Walker, Vol. 931 (Humana Press, 2013) pp. 29–57.

[4] J. B. Pawley, *Handbook of biological confocal microscopy* (Springer Science & Business Media, 2006).

[5] S. W. Hell and J. Wichmann, *Breaking the diffraction resolution limit by stim-*

ulated emission: stimulated-emission-depletion fluorescence microscopy, Optics Letters **19**, 780 (2008).

[6] M. G. Gustafsson, L. Shao, P. M. Carlton, C. J. Wang, I. N. Golubovskaya, W. Z. Cande, D. A. Agard, and J. W. Sedat, *Three-dimensional resolution doubling in wide-field fluorescence microscopy by structured illumination,* Biophysical Journal **94**, 4957 (2008), arXiv:NIHMS150003 .

[7] B. Huang, W. Wang, M. Bates, and X. Zhuang, *Three-Dimensional Super-Resolution Reconstruction Microscopy,* Health (San Francisco) , 810 (2008).

[8] B. Huang, M. Bates, and X. Zhuang, *Super-resolution fluorescence microscopy,* Annual review of biochemistry **78**, 993 (2009).

[9] J. C. M. Gebhardt, D. M. Suter, R. Roy, Z. W. Zhao, A. R. Chapman, S. Basu, T. Maniatis, and X. S. Xie, *Single-molecule imaging of transcription factor binding to DNA in live mammalian cells,* Nature Methods **10**, 421 (2013).

[10] E. Zagato, T. Brans, S. Verstuyft, D. van Thourhout, J. Missinne, G. van Steenberge, J. Demeester, S. De Smedt, K. Remaut, K. Neyts, and K. Braeckmans, *Microfabricated devices for single objective single plane illumination microscopy (SoSPIM),* Optics Express **25**, 1732 (2017).

[11] H. Deschout, K. Raemdonck, S. Stremersch, P. Maoddi, G. Mernier, P. Renaud, S. Jiguet, A. Hendrix, M. Bracke, R. Van den Broecke, M. Röding, M. Rudemo, J. Demeester, S. C. De Smedt, F. Strubbe, K. Neyts, and K. Braeckmans, *On-chip light sheet illumination enables diagnostic size and concentration measurements of membrane vesicles in biofluids,* Nanoscale **6**, 1741 (2014).

[12] M. Plöschner, V. Kollárová, Z. Dostál, J. Nylk, T. Barton-Owen, D. E. K. Ferrier, R. Chmelík, K. Dholakia, and T. Čižmár, *Multimode fibre: Light-sheet microscopy at the tip of a needle,* Scientific Reports **5**, 18050 (2015).

[13] C. J. Engelbrecht, F. Voigt, and F. Helmchen, *Miniaturized selective plane illumination microscopy for high-contrast in vivo fluorescence imaging.* Optics letters **35**, 1413 (2010).

[14] H. Talbot, *LXXVI. Facts relating to optical science. No. IV* , The London, Edinburgh, and Dublin Philosophical Magazine and Journal of Science (1836), 10.1080/14786443608649032.

[15] J. Wen, Y. Zhang, and M. Xiao, *The Talbot effect: recent advances in classical optics, nolinear optics, and quantum optics,* Advances in Optics and Photonics **6**, 293 (2013).

[16] U. R. Ankele G., *Self imaging in homogeneous planar optical waveguides,* Applied Physics Letters **27**, 337 (1975).

[17] E. E. Grigor 'eva and A. T. Semenov, *Waveguide image transmission in coherent light (review),* Soviet Journal of Quantum Electronics) **5**, 1877 (1978).

[18] R. Ulrich, *Image formation by phase coincidences in optical waveguides,* Optics Commun. **13**, 259 (1975).

[19] C. Gomez-Reino, M. V. Perez, and C. Bao, *Gradient-index optics: fundamentals and applications* (Springer Science & Business Media, 2012).

7

Conclusions and Future work

This dissertation has mainly aimed at developing novel techniques, methodologies for measuring the optical field, specifically both the amplitude and phase distribution. Furthermore, we have attempted to extend their applications in the scope of optical imaging, including lensless/holographic imaging, quantitative phase imaging and the calibration for light-sheet microscopes.

Due to the fast oscillatory nature of light waves, the direct registration of its wave properties, such as its phase, are currently impossible with the present intensity-only detectors. Thus, abundant information contained in the optical field is lost. For example, the spatial information contained in phase is valuable for many scientific and engineering applications. Many methods have been proposed to retrieve the complete optical field. Each one of them lays particular emphasis on either accuracy, speed or spatial resolution, etc. When it comes to many specific scenarios, novel techniques need to be developed whilst confronting many of these trade-offs. These technologies are not fixed and separated. They can be improved, varied or integrated in many different ways. One sensor will not stick to only one specific use. Under certain conditions, they are able to perform well even in unconventional applications. Therefore, exploring new types of optical field sensors and breaking through the boundaries of the existing sensors uses are very interesting and current research topics.

The contributions of this dissertation addressing the above research topics can be mainly summarized into three parts. First, we have developed the techniques that register the optical field by utilizing a spatial amplitude modulator (Chapter 3). Secondly, the feasibility of applying a Shack-Hartman wavefront sensor to holographic imaging and quantitative phase imaging has been thoroughly investigated (Chapter 4 & 5). Finally, approaches based on multimode waveguides that miniaturize the illumination of light-sheet microscopy has been explored (Chapter 6). Hereafter is the summary of accomplishments in these topics and suggestions for their further research.

Optical field sampling with spatial amplitude modulating

This part of the work aimed at achieving a reference-free optical field sensing scheme that with features both high resolution performance and less computational effort.

As introduced in Chapter 1, the general holographic methods require a well-defined reference beam to record the optical field. This external reference largely hinders the simplification and stability of the optical setup. To address to this problem, we have developed a method for recording the coherent optical field that keeps the interferometric scheme while introduces the reference internally from one selected part of the light beam. It is realized by interfering the selected reference with the remaining field point by point through forming a series of Young's interferometers. Then, from each interferogram recorded in the far field, we could calculate the intensity sum and the phase difference of the reference and the corresponding points. Eventually, the whole optical field could be registered by combining all the measurements. We have experimentally verified this method via a binary amplitude spatial light modulator, digital micro-mirror device. The programmable micro-mirrors were used to form the scanning two-point interferometer. In the experiments, a lensless coherent microscope was built, and an optical field measurement with 150×150 points and an interval of 21.6 μm which is sufficient for computational imaging has been demonstrated.

We have proposed another technique, based on computational methods, that makes use of algorithms for iterative phase retrieval whist speeding up the convergence through introducing randomness and sparsity by an amplitude spatial light modulator. Multiple binary masks with a shared 'on' region as a reference, sample the optical field, forming speckle patterns in the far field. For each frame, the phase and amplitude of 'on' pixels are retrieved by alternating projection algorithms. Different from the previous methods, the whole optical field then can be reconstructed from much fewer frames instead of the point-wise scheme. Numerical simulations have shown a quicker convergence than the standard Gerchberg-Saxton algorithm. Also, a defocused optical field has been successfully reconstructed in experiment.

Both of these two schemes can remove the need for an external reference beam. The two-dimensional amplitude and phase of the aperture can be registered with a resolution the same as the size of the deployed SLM pixels which generally ranges from several microns to tens of microns. In principle, this approach does not need any lenses which is suitable for the situations where the use of such imaging optics is problematic.

Suggestions for future work The research in this type of optical field sensing approach is still very primitive. The future development of it should focus on improving the efficiency and robustness, which may come from looking at the following aspects:

- **Acquisition speed** So far, the time-consuming nature of the method has been the least considered. The acquisition process mainly includes the projection of the DMD pattern and the camera recording. Currently, the DMD runs in the HDMI video mode which is limited to 60 Hz. A low-cost CMOS camera with a frame rate of 25 fps records the interferogram. The phase extraction process is also integrated in the loop. Thus, it leads to a registration speed of 14 Hz. For the phase retrieval scheme in which only tens of frames are needed, the speed is acceptable. However, in the point-scanning scheme, registering the whole aperture with the highest resolution requires millions of samples leading to hours of measurement. The DMD had a maximum speed of 3 kHz in the pattern sequence display mode, although it has limited patterns can be stored due to the limited memory size of the device. Now, the bottleneck would be the camera, which we may consider replacing with a fast speed camera or line camera.

- **Smarter pattern planning** In the present experiments, we just used one pixel as reference and the reference was set to the centroid of intensity distribution within the measured aperture. This will be sufficient if the light is rather uniformly distributed. However, if the reference pixel happens to reflect no light, then this method will fail due to no interference fringes and subsequent random solutions. Thus, a more robust reference selection procedure is needed to guarantee there is enough light on the pixel to achieve interference. In addition, the dark area of the aperture needs no measurement. If we can determine this light distribution from priori information, we are able to reduce the total number of measurements, which speeds up the acquisition in the software.

- **Calibration** One critical problem in the phase retrieval scheme is the calibration. In the proof-of-principle stage, we simply used the wave propagation model by assuming there is no error in the arrangement of optical components. As a result, we have observed severe instability of the phase reconstruction in the experiments. The errors may come from the translation and rotation introduced by the misalignment of the camera or DMD. It should be reduced by more accurate physical adjustment or algorithmic self-calibration.

- **Phase retrieval algorithms** Currently, the phase retrieval procedure in the method is performed by a simply-modified Gerchberg-Saxton algorithm. Although for a single frame, the required number of iterations for convergence reduced dramatically. However, multiplying it with the required number of frames still leads to a great amount of computational effort. Many modern phase retrieval algorithms may improve the performance in terms of the accuracy, convergence and robustness.

Extending the application of conventional wavefront sensor

The purpose of this part of the work is to extend the potential applications of the Shack-Hartmann wavefront sensor, especially for holographic imaging and quantitative phase imaging.

We have validated the feasibility of the coherent holographic imaging with a high density SHWFS. The coherent diffraction field can be directly registered by the SHWFS and back propagated to different planes to extend the information. There is no need of reference beam in the optical setup. A reference can be pre-registered or virtually appointed. In the experiment, we have successfully reconstructed the image of a resolution target with a 140 × 140 SHWFS close to the diffraction limit. The image contrast is also higher than the conventional in-line holography scheme. Thus, it is a promising alternative for digital holography in many applications, especially when the illumination has a low temporal coherence or a simple optical setup is required.

By placing the SHWFS in the imaging plane in a microscope, we have achieved an approach to measure the optical path difference map or the quantitative phase map with the refractive index of known samples. As a non-interferometric technique, it requires a much less spatial coherence of the illumination to guarantee the correct OPD measurement. In the experiments, we have implemented the OPD microscope in both transmissive and reflective configurations. Both biological samples in the cellular level and micro optics component were successfully examined. A conventional optical microscope can be easily transformed into an OPD microscope, with the help of a SHWFS and an adjustment of the illumination, to retrieve the quantitative 3D information of the sample.

Suggestions for future work The future direction of this part of the work may focus on improving the performance of the developed techniques in terms of the following aspects:

- **Resolution** Due to the extra indispensable optics components, currently, a WFS can not achieve the same sampling resolution as digital holography in general. Some modified SHWFS sensors, such as using a quad-cell array to replace the camera sensor, may increase the resolution at the hardware level. Also, there are various pixel super-resolution techniques that can achieve a sub-pixel resolution by utilizing sub-pixel displacements in the imaging system. The possibility to enhance the SHWFS resolution with these techniques can be explored.

- **Removing artifacts** From the preliminary experimental results in Chapter 4, we can observe some artifacts in the reconstruction. These may be caused by incorrect phase unwrapping, or the primitive back propagation algorithms, which needs to be compensated in any further work. The dark areas due to the strong scattering or sample absorption will lead to a wrong reconstruction of the wavefront gradients. Although, they are insignificant for the propagation with the low amplitude, they can still effect the correct wavefront integration. Thus, the algorithms to eliminate such effects should be investigated.

- **Field of view and dynamic range** In the SHWFS based OPD microscope, we sacrifice the field of view to match the resolution of the imaging system, which limits the throughput of this approach. To achieve a larger FOV, a scanning manner of the sensor or sample can be considered. Also, for the sample with a steep surface or extreme varied refractive index medium, the wavefront gradients may go beyond the dynamic range of a SHWFS. For this case, the techniques that integrate multiple angled illuminations or sensors may be helpful. However, for this a usable implementation and algorithms need to be further researched.

Light-sheet microscopy illumination with waveguide

The final part of the work focused on developing a technique that can miniaturize the footprint of light-sheet illumination while support the introduction of adaptive control. Two approaches based on different forms of waveguide have been investigated.

Firstly, a slab waveguide has been designed to transmit the light-sheet by utilizing the Talbot effect. It is a multimode fibre in essence while being much more robust. The performance was simulated by the beam propagation method. In the experiments, a light-sheet with a FWHM of around 5 μm has been reproduced. Thus, with the help of this waveguide, the optics tip at the sample end can be reduced to the order of tens of microns.

As a successor, another form of waveguide based on the GRIN lenses has been developed. Although the tip at the sample end goes up from hundreds microns to millimetres, its on-shelf availability makes it much easier to implement than the slab waveguide. We have optimized the arrangement of commercial GRIN lenses assembly to accomplish this. In the experiments, a high quality light-sheet, with the beam waist closes to the diffraction limit of the setup has been realized.

Suggestions for future work This part of the work was proof-of-concept research and a start point of the Adaptive Imaging Microscopy (AIM) project. Thus, various prospects should be explored in the future. A few of them are listed below:

- **Structure optimization and fabrication** The current design of the waveguide has plenty of room for improvement. Such as the choices of the core and cladding medium of the slab waveguide, especially when it is immersed in water; the arrangement of the GRIN lens assembly to support a higher numerical aperture. Moreover, the usability and robustness should be improved by designing proper packaging for the components. As for the fabrication process, currently all the waveguides are handmade with rough quality control. For example, we have observed a low SNR in the slab waveguide experiments. This noise may be brought by the scattering from the poorly polished waveguide facets. Thus, we need to enhance the performance with better and more modern fabricating techniques.

- **Integrating with the imaging part** In the experiments, the imaging arm is only used to detect the light-sheet quality produced by the waveguides. When it comes to the real biological samples and high numerical aperture situations, we need to specifically design the sample holder and the arrangement of both the illumination arm and imaging arm, so that there is no interference between them. To achieve a fully functional LSFM, a convenient scanning scheme to selected plane should also be determined.

- **Adaptive control** The waveguide is designed to support multimode propagation, which allows the beam shaping with adaptive optics components such as deformable mirrors and SLMs. It can be used to compensate the imperfection of the optical component and the aberrations brought by the samples. To achieve full control of the light-sheet, the effect of the transportation of these unconventional waveguides still needs to be studied.

Curriculum Vitæ

Hai GONG

28-08-1989	Born in Hunan, China.

Summary

I am currently researching the topics of phase imaging, wavefront sensing & shaping and light-sheet microscopy. Experienced in building optical setups, designing optomechatronics systems and applying computational imaging methods. Multiple systems for microscopy, metrology and robotics has been successfully built. Interests lie in developing innovative optical imaging techniques as well as their biomedical and industrial applications.

Education

2014–2019 **Doctor of Philosophy**
Delft University of Technology, the Netherlands
Dissertation: Optical field sampling for imaging and optical testing
Promotors: Prof. G. Vdovin, Prof. M. Verhaegen

2011–2014 **Master in Mechanical Manufacturing and Automation**
Xi'an Jiaotong University, China
Thesis: Mode-hop suppression of tunable external cavity diode laser
Supervisor: Prof. dr. Z. Liu

2007–2011 **Bachelor in Mechanical Design, Manufacturing and Automation**
Harbin Institute of Technology, China

Awards & Scholarships

2017	Silver winner of Edmund Optics Educational Award
2014	Scholarship of CSC (China Scholarship Council)
2013	Philip K.H. Wong Scholarship, Hong Kong
2011	National Encouragement scholarship, China
2010	First prize of National Mechanical Innovation Design Competition, China
2010	Meritorious Winner of Interdisciplinary Contest in Modeling, United States
2009	First prize of National Undergraduate Mathematical Contest in Modeling, China

List of Publications

Journal Publications

1. T. E. Agbana, **H. Gong**, A. S. Amoah, V. Bezzubik, M. Verhaegen, and G. Vdovin, Aliasing, coherence, and resolution in a lensless holographic microscope, Opt. Lett. 42(12), 2271 (2017).
2. **H. Gong**, O. Soloviev, D. Wilding, P. Pozzi, M. Verhaegen, and G. Vdovin, Holographic imaging with a Shack-Hartmann wavefront sensor, Opt. Express 24(13), 13729 (2016).
3. **H. Gong**, T. E. Agbana, P. Pozzi, O. Soloviev, M. Verhaegen, and G. Vdovin, Optical path difference microscopy with a Shack–Hartmann wavefront sensor, Opt. Lett. 42(11), 2122 (2017).
4. G. Vdovin, **H. Gong**, O. Soloviev, P. Pozzi, and M. Verhaegen, Lensless coherent imaging by sampling of the optical field with digital micromirror device, J. Opt. 17(12), 122001 (2015).

Conference Publications

1. **H. Gong**, O. Soloviev, G. Vdovin, and M. Verhaegen, Shack-Hartmann reflective micro profilometer, 2017 Int. Conf. Opt. Instruments Technol. Opt. Syst. Mod. Optoelectron. Instruments (January), 68 (2018).
2. **H. Gong**, P. Pozzi, O. Soloviev, M. Verhaegen, and G. Vdovin, Phase retrieval from multiple binary masks generated speckle patterns, Proc. of SPIE 9899, p. 98992N (2016).
3. **H. Gong**, P. Pozzi, O. Soloviev, M. Verhaegen, and G. Vdovin. Optical field reconstruction with digital micromirror interferometry, X International Workshop of Adaptive Optics for Industry and Medicine (2015).